ELECTRONIC AND MAGNETIZATION DYNAMICS OF COBALT SUBSTITUTED IRON OXIDE NANOCRYSTALS

A Dissertation

by

TAI-YEN CHEN

Submitted to the Office of Graduate Studies of
Texas A&M University
in partial fulfillment of the requirements for the degree of

DOCTOR OF PHILOSOPHY

December 2010

Major Subject: Chemistry

Electronic and Magnetization Dynamics of

Cobalt Substituted Iron Oxide Nanocrystals

ELECTRONIC AND MAGNETIZATION DYNAMICS OF COBALT SUBSTITUTED IRON OXIDE NANOCRYSTALS

A Dissertation

by

TAI-YEN CHEN

Submitted to the Office of Graduate Studies of
Texas A&M University
in partial fulfillment of the requirements for the degree of

DOCTOR OF PHILOSOPHY

Approved by:

Chair of Committee,	Dong Hee Son
Committee Members,	Paul S. Cremer
	Simon W. North
	Hans A. Schuessler
Head of Department,	David H. Russell

December 2010

Major Subject: Chemistry

ABSTRACT

Electronic and Magnetization Dynamics of

Cobalt Substituted Iron Oxide Nanocrystals. (December 2010)

Tai-Yen Chen, B.S.; M.S., National Tsing Hua University, Taiwan

Chair of Advisory Committee: Dr. Dong Hee Son

Knowledge of energy dissipation and relaxation in electron, spin, and lattice degrees of freedom is of fundamental importance from both a technological and scientific point of view. In this dissertation, the electronic and magnetization dynamics of photoexcited colloidal cobalt substituted iron oxide nanocrystals, $Co_xFe_{3-x}O_4$, were investigated through transient absorption and pump-probe Faraday rotation measurements.

In this dissertation, linearly polarized femtosecond optical pulses at 780 nm were used to excite the weak absorption originating from the intervalence charge transfer transition (IVCT) between Fe^{2+} and Fe^{3+} ions of Fe_3O_4 nanocrystals. The timescale and corresponding relaxation processes of electronic relaxation dynamics of the excited IVCT state were first discussed. Size effect on electronic relaxation dynamics in Fe_3O_4 nanocrystals is not distinct on the basis of result from this study. One interesting feature of electronic dynamics data of photoexcited Fe_3O_4 nanocrystals is the creation of coherent acoustic phonons. Information on lattice temperature was obtained by measuring the period of coherent acoustic phonon as a function of excitation fluence and fit into a simple model based on Lamb's theory. Since optical control of the

magnetization can be either through optical or heating mechanisms, quantitative estimation of degree of demagnetization caused by lattice temperature is made by using Langevin function. The result from such estimation indicates the effect of lattice temperature rise on magnetization is too small to significantly affect the magnetization of Fe_3O_4 nanocrystals.

Magnetization dynamics were studied via pump-probe Faraday rotation measurements. Optical excitation with near-infrared pulse resulted in an ultrafast demagnetization in 100fs. The energy of the excited state then relaxed through spin-lattice relaxation (SLR). Effects of surface spin and chemical tuning on the SLR were investigated by comparing the magnetization recovery timescales of nanocrystal with different particle sizes and cobalt concentration respectively. The experimental result is explained by a simple model where interior and surface spins contributed to the spin-lattice relaxation process differently. The observations suggest that spin-orbit coupling of the surface is stronger and less sensitive to stoichiometric variation than the interior spins of the nanocrystals.

for my parents and family

ACKNOWLEDGEMENTS

My graduate student life finally came to an end after all these years of studying at Texas A&M University. Getting a Ph.D. degree overseas is quite an interesting experience, not because I need to speak English all the time, but to have the chance to learn and discuss new science with people from different countries. I am deeply grateful for such a life experience and want to thank the important people in my Ph.D. journey.

I have been fortunate to be among the first graduate students to work with my dissertation advisor, Dong Hee Son. From building up instruments, designing experiments, discussing experimental results and writing scientific papers, my education and scientific philosophy from Dong Hee are all that I could have hoped for. For his valuable time, patience and concern I am thankful.

I would also like to thank my dissertation committee members: Dr. North, Dr. Cremer, Dr. Gao, Dr. Hilty and Dr. Schuessler, for their help and advice for my research and dissertation.

As for my wonderful colleagues, Chih-Hao, Stacey, Hsiang-Yun, Shengguo, Erick, and Yeork: working with you makes my life in the lab very interesting. I am grateful for the extensive help that I received for the sample preparation from Chih-Hao and Hsiang-Yun, and the excellent advice on my seminar and preliminary and final exams from our presentation master, Stacey.

Finally, I would like to thank my parents and family for their love and encouragement which give me the energy to move on.

TABLE OF CONTENTS

CHAPTER Page

LIST OF FIGURES

FIGURE Page

FIGURE Page

FIGURE Page

FIGURE Page

LIST OF TABLES

CHAPTER I

INTRODUCTION

The magnetization of ferromagnetic material can be altered with different disturbances such as changes in temperature, magnetic field, or light on various time scales. The excitation energy can be stored by a ferromagnetic material in three different ways: deposit the energy to electrons, the excitation of phonons and change of magnetic ordering. Investigation of the time scales of energy dissipation processes of excited magnetic material between different degrees of freedoms (electron, spin, and lattice, see Figure 1.1) and their relationship to the sizes, chemical compositions of magnetic materials have been an important field of research since the electron spin is actively exploited as a new information carrier in addition to the electron charge. Due to the successful progress in femtosecond laser technology, optical excitation of ferromagnetic materials opened a new door to manipulate the magnetization on the time scale much faster than the typical spin-lattice relaxation time. This ultrafast modification of magnetization attracted a lot of attention and therefore during the past two decades, a significant effort was made to understand the mechanisms of photo- induced ultrafast demagnetization, magnetization and spin-switch of magnetic thin film structures.

This dissertation follows the style of *Journal of the American Chemical Society*.

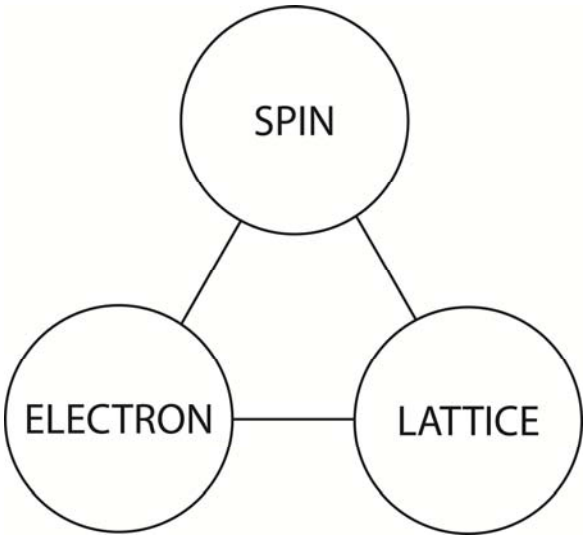

Figure 1.1. A ferromagnetic material can store the energy in electron, spin, and lattice degrees of freedom.

As the demand for denser memory pushes data storage technologies to nanometer length scales, spatial confinement and surface effect on energy dissipation and relaxation in and between various degrees of freedoms became very important. To systematically study these effects, colloidal magnetic nanocrystals provided an ideal platform due to the great chemical tunibility of particle size, shape, stoichiometry, and surface modification. For example, sizes of monodispersed Fe_3O_4 nanocrystals can be easily tuned from 5 nm to 20 nm with size distribution < 10 % by using reported method. The shape and metal ion doping control can be achieved by changing the reaction heating rate, crystal growth temperature and relative molar ratio between metal ions. Furthermore, researches on

static and dynamic electric and magnetic properties have been conducted on the bulk phase, which provided valuable spin and orbital information on *d*-electrons.

In this dissertation, we reported the time-resolved studies on the optically induced electronic and magnetization dynamics in size-controlled magnetic cobalt substituted iron oxide nanocrystals. Linearly polarized femtosecond optical pulses at 780 nm excited the weak absorption originating from the intervalence charge transfer transition (IVCT) between Fe^{2+} and Fe^{3+} ions. For electronic dynamics study, relaxation time scales and corresponding processes of optically excited IVCT transition and size effect on energy dissipation and relaxation of photoexcited Fe_3O_4 nanocrystals were discussed.

One interesting feature of electronic dynamics data of photoexcited Fe_3O_4 nanocrystals is the creation of coherent acoustic phonon which manifest itself as the modulation of transient absorption. The presence of coherent phonon implies the strong electron-phonon coupling in Fe_3O_4 nanocrystals and photoexcited electrons dump the energy to lattice degrees of freedom via phonon motion and increase the lattice temperature. Since changes in temperature can also disturb the magnetization of magnetic material, it is important to understand to what extend the lattice temperature can change magnetization so that an accurate picture of the dynamic magnetization in photoexcited magnetic nanocrystals can be obtained. Therefore, information on lattice temperature was obtained by measuring the period of coherent acoustic phonon as a function of excitation fluence and fit into a simple model based on Lamb's theory. The degree of demagnetization was further estimated by using Langevin function.

Finally, magnetization dynamics of photoexcited magnetic nanocrystals was studied by adapting pump-probe complex Faraday rotation technique. The photoexcitation resulted in an instantaneous decrease of Faraday rotation, indicating ultrafast demagnetization, and relax the energy via spin-lattice relaxation process. In this dissertation, we especially focused on the size and chemical effect on spin-lattice relaxation process. One of the key factors determining the rate of energy flow from spin to lattice degrees of freedom is effective spin-orbit coupling, which is determined by intrinsic atomic spin-orbit coupling strength and ligand field splitting energy. Intrinsic spin-orbit coupling strength typically is tuned by changing the chemical composition and ligand field can be tuned by modifying the local geometry structure. In nanoscale magnetic material, there are many surface spins under different ligand fields from those of the interior spins due to the structure discontinuity on the surface. Therefore, one would expect that the rate of energy and momentum transfer in spin degrees of freedom in nanoscale magnetic material be significantly influenced by the surface spins. One interesting question arises from this is whether the relative efficiency of the surface of the nanocrystals in spin-lattice relaxation will vary with intrinsic atomic spin-orbit coupling. Before being able to answer these questions, it is necessary to understand the background on concepts and phenomena involved in ultrafast electronic and magneto-optical experiments.

The dissertation is organized as follows: In Chapter II some basic concepts such as the origin of the magnetism and magnetism in nanoscale were addressed. A brief review of recent experiments studying laser induced magnetization dynamics will be presented

as well. Chapter III will introduce the sample preparation, basic physical properties characterization and the measurement techniques applied in our experiments. Phenomenological origin of magneto optical Faraday effect and implementation of such effect into real measurement were discussed. Chapters IV, V, and VI will cover the experimental results regarding the dynamic properties after photoexcitation. Specifically, Chapter IV will present the electronic dynamics of Fe_3O_4 nanocrystals as a function of probe wavelength, pump fluence and particle sizes. Laser excited intervalence charge transfer transition in nanocrystal resulted in the presence of coherent phonons by displacive excitation of coherent phonon mechanism. Chapter V will discuss the estimation of transient lattice temperature of photoexcited Fe_3O_4 nanocrystals from the oscillation frequencies of coherent acoustic phonons. Effect of transient temperature rise on magnetization will also be addressed. Chapter VI will focus on the slow magnetization recovery process, spin-lattice relaxation, after photoexcitation. Effects of surface spin and chemical tuning on spin-lattice relaxation will be addressed by comparing the size and chemical composition dependent magnetization dynamics, respectively. Experimental results were fitted into a simple model and the relative contribution of surface to interior spin to spin-lattice relaxation was estimated.

CHAPTER II

THEORETICAL BASICS

In this chapter, we will cover the theoretical basics of magnetism starting from discussing the atomic origin of magnetism and how angular momentum is related to magnetism.[1-3] After understanding the atomic origin of magnetism, the focus is then turned to the origin of long range magnetic ordering in materials, exchange interaction, where superexchange and double exchange are discussed in detail. Finally, magnetism in nanoscale magnetic material and recent research on laser induced magnetization dynamics is introduced.

2.1 Atomic Origin of Magnetism

2.1.1 From classic to quantum: origin of magnetism

In 1820, Danish scientist Oersted discovered that an electric current gave a force on and deflected the needle of a loadstone compass. This breakthrough eventually lead to the establishments of electromagnetism and Maxwell's equations. From electromagnetism's point of view, the origin of magnetism is due to the motion of electron which can be described with a current loop. For example, if there is an electron circulating a loop (radius $\boldsymbol{r}$, area $\boldsymbol{A}= \pi \boldsymbol{r}^2$) with angular velocity $\boldsymbol{\omega}$ (resulting current $\boldsymbol{I} = -\boldsymbol{e\omega}/2\pi$), then the magnetic moment ($\boldsymbol{\mu}$) is defined as

$$\boldsymbol{\mu} = \boldsymbol{I}\,\boldsymbol{A} \text{ (unit: A m}^2\text{)} \qquad 2.1$$

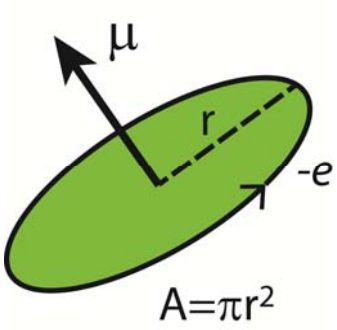

Figure 2.1. An elementary magnetic moment resulting from a current loop.

The direction of the vector is normal to the loop and corresponds to the north pole of a bar magnet if the current is circulating in a counter-clockwise direction (Figure 2.1). This simple picture not only satisfactorily explained macroscopic magnetism phenomena but also provided an insight to the microscopic origin of magnetism which is explained via orbit and spin angular momenta of electrons.

The relationship between the magnetic moment ($\boldsymbol{\mu}$) and angular momentum (**L**) is well demonstrated by the Einstein-de Haas effect. In short, a ferromagnetic material of cylindrical shape and originally at rest suspended with the aid of a thin string inside a coil. On driving an impulse of electric current through the coil (create magnetic moment, $\boldsymbol{\mu}$), a mechanical rotation (with angular momentum, **L**) of a ferromagnetic material is induced due to the conservation of total angular momentum (Figure 2.2). Therefore,

$$\boldsymbol{\mu} = \gamma \mathbf{L} \qquad 2.2$$

where γ is a constant known as the gyromagnetic ratio.

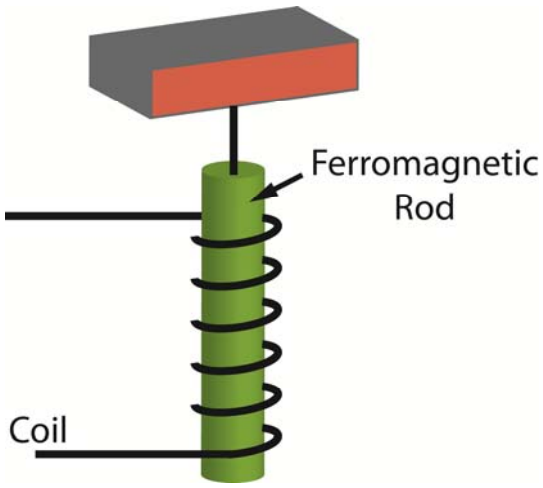

Figure 2.2. Experimental setup for study of Einstein-de Haas effect.

Once the link between magnetic moment and angular momentum is made, we now can understand the origin of the magnetism of free atom in a quantum mechanical way by utilizing the concept of angular momentum.

The magnetic moment of a free atom in the absence of a magnetic field consists of two contributions: (1) orbital angular momentum resulting from the electrons circulating the nucleus and (2) spin angular momentum of each electron arising from its spin. The total angular momentum with spin and orbital contribution accounts for the observed magnetic moment.

In quantum mechanics, orbital angular momentum is described by using orbital angular quantum number l and magnetic quantum number m_l. The magnitude of orbital angular momentum $|L|$ is related to l by $|L| = \sqrt{l(l+1)}\hbar$. When orienting the orbital angular momentum with respect to a magnetic field, the possible orientation can be

labeled by the magnetic quantum number m_l, which is allowed to take integer values from $-l$ to $+l$. The component of angular momentum along the field direction (z direction) is equal $m_l\hbar$ (Figure 2.3(a)). From equation 2.1, magnetic moment can be expressed as $\boldsymbol{\mu} = \boldsymbol{I}\,\boldsymbol{A} = -\,\mathbf{e}\boldsymbol{\omega}\boldsymbol{r}^2/2$, while angular momentum $\boldsymbol{p}$ of an electron is $\boldsymbol{m_e r^2 \omega}$, magnetic moment can be rewritten as $\boldsymbol{\mu} = -\,(\boldsymbol{e}/2\boldsymbol{m_e})\,\boldsymbol{p}$. By substituting $\boldsymbol{p}$ with $|L|$, the magnetic moment $\boldsymbol{\mu_L}$ due to the orbital motion of the electron will be

$$\boldsymbol{\mu_L} = -\,g_L\,(\boldsymbol{e}\hbar/2\boldsymbol{m_e})\,\frac{|L|}{\hbar} = -\,g_L\,\mu_B\,\frac{|L|}{\hbar} \qquad 2.3$$

where μ_B is the Bohr magneton, defined by $\mu_B = \boldsymbol{e}\hbar/2\boldsymbol{m_e} = 9.274\times10^{-24}$ Am^2, g_L is electron orbital g-factor and exactly equal to 1. The z-component of magnetic moment then becomes $\mu_Z = g_L\mu_B m_l$, which, since $g_L = 1$, is just $\mu_B m_l$.

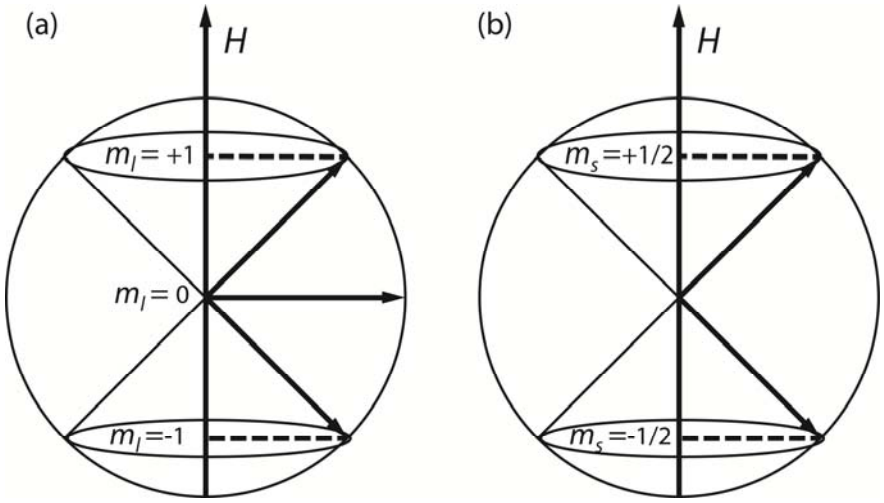

Figure 2.3. The component of (a) orbital angular momentum and (b) spin angular momentum along the field direction (z direction).

The second contribution to magnetic moment is the intrinsic angular momentum of an electron spin. The spin of an electron is characterized by a spin quantum number *s* (always has the value of $\frac{1}{2}$) and spin projection quantum number ms (either $+\frac{1}{2}$ or $-\frac{1}{2}$). The magnitude of the spin angular momentum $|S|$ is defined by $|S| = \sqrt{s(s+1)}\hbar$ and the component of spin angular momentum along the field direction is given by $m_s\hbar$ (Figure 2.3(b)). The magnetic moment due to the electron spin is

$$\boldsymbol{\mu_S} = -\, g_S\, \mu_B\, \frac{|S|}{\hbar} \qquad 2.4$$

where $g_S = 2.002319$ is called electron spin g-factor of the electron. The z-component of magnetic moment is then become $\mu_Z = g_S\mu_B m_s$. If we take $g_S = 2$, it means the spin magnetic moment along the field direction of a single electron is one Bohr magneton.

To obtain the total magnetic moment of an electron, the total angular momentum must be extracted first. So far we have kept the spin and orbital angular momentum separate since they are independent of one another. However, they do weakly couple via the spin-orbit interaction. Because of this, *L* and *S* are no longer separately conserved but the total angular momentum *J* is. For one electron case, the total angular momentum will be the sum of orbital and spin angular momentum, $J = L + S$. Similar to the orbit and spin angular momentum case, the magnitude of the total angular momentum is $|J| = \sqrt{J(J+1)}\hbar$ and the component is $m_J\hbar$. The total magnetic moment is

$$\boldsymbol{\mu} = -\, g_J\, \mu_B\, \frac{|J|}{\hbar} \qquad 2.5$$

where g_J is called *Landé* g-factor of the electron and is related with L and S by

$$g_J = \frac{3}{2} + \frac{S(S+1) - L(L+1)}{2J(J+1)} \quad 2.6$$

2.1.2 Total angular momentum of a multi-electron atom

When extending the idea to an atom with many electrons, the most important question is how to calculate the total angular momentum correctly. For an atom with many electrons, orbit-orbit and spin-spin interactions also need to be taken into account. Depending on the relative magnitudes of orbit-orbit, spin-orbit and spin-spin interactions, two different schemes will be adapted to calculate total angular momentum of all the electrons: (1) *L*-*S* and (2) *j*-*j* coupling.

(1) *L*-*S* coupling (*Russell-Saunders* coupling)

When the coupling of individual spin-spin and individual orbit-orbit is stronger than the spin-orbit coupling (which is the case for light atoms), *L*-*S* coupling scheme will be used. The way to calculate the total angular momentum is to first combine the orbit and spin angular momentum of each individual electron to obtain the total orbit and spin angular momentums, respectively (Equation 2.7). The total angular momentum is then the vector sum of the total orbit and total spin angular momentums (Equation 2.8).

$$L = \sum l_j \, , S = \sum s_j \quad 2.7$$

$$J = L + S = \sum l_j + \sum s_j \quad 2.8$$

Since the choice of *z*-component of *L* and *S* can be -*L*, -*L*+1, …, *L*-1, *L* and –*S*, -*S*+1, …, *S*-1, *S*, the orbital and spin angular momentum can therefore combine in (2*L*+1)(2*S*+1)

ways, which will cost different amounts of energy. To identify the ground state electron configuration of a partially filled ion, *Hund's* rules need to be followed.

I. Arrange the electrons to maximize their total spin, *S*.

II. For a given spin arrangement, the configuration with the largest total orbital angular momentum, *L*, lies lowest in energy.

III. For atoms with less than half-full shells, $J = |L - S|$ lies lowest in energy. For atoms with more than half-full shells, $J = |L + S|$ lies lowest in energy.

Once the values for *S*, *L*, *J* are determined, the ground state can be summarized using a term symbol of the form ${}^{2S+1}L_J$ and the magnetic moment of an ion can also be estimated via $\mu = - g_J \mu_B \sqrt{J(J+1)}$. As shown in Table 2.1, excellent agreement is usually found between the prediction and the measured values for 4*f* ions. However, when applying the same estimation for 3*d* ions, a distinct discrepancy is observed in Table 2.2. The reason for this discrepancy is that for 3*d* ions, the crystal field interaction is much stronger than the spin-orbit interaction. In this case, electrons in 3*d* ions cannot draw a definite orbit and this leads to the negligible orbital contribution to the magnetic moment. For 4*f* ions, the orbitals are much less extended away from the nucleus and lie beneath the 5*s* and 5*p* shells. Therefore the crystal field effect is much less distinct. By comparing the experimental data with $\mu = - g_J \mu_B \sqrt{S(S+1)}$, (assume $L = 0$), a much better correlation is observed for 3*d* ions. This effect is known as *orbital quenching* and indicates that magnetic moment in 3*d* magnetic materials is mainly caused by electron spins.

Table 2.1 Prediction of magnetic ground states of 4*f* ions using Hund's rules, $p = g_J[J(J+1)]^{1/2}$, is very close to the values, p_{exp}, from measurements.

ion	shell	S	L	J	term	p	p_{exp}
Ce^{3+}	$4f^1$	1/2	3	5/2	$^2F_{5/2}$	2.54	2.51
Pr^{3+}	$4f^2$	1	5	4	$^3H_4$	3.58	3.56
Nd^{3+}	$4f^3$	3/2	6	9/2	$^4I_{9/2}$	3.62	3.3-3.7
Pm^{3+}	$4f^4$	2	6	4	$^5I_4$	2.68	-
Sm^{3+}	$4f^5$	5/2	5	5/2	$^6I_{5/2}$	0.85	1.74
Eu^{3+}	$4f^6$	3	3	0	$^7F_0$	0.0	3.4
Gd^{3+}	$4f^7$	7/2	0	7/2	$^8S_{7/2}$	7.94	7.98
Tb^{3+}	$4f^8$	3	3	6	$^7F_6$	9.72	9.77
Dy^{3+}	$4f^9$	5/2	5	15/2	$^6H_{15/2}$	10.63	10.63
Ho^{3+}	$4f^{10}$	2	6	8	$^5I_8$	10.60	10.4
Er^{3+}	$4f^{11}$	3/2	6	15/2	$^4I_{15/2}$	9.59	9.5
Tm^{3+}	$4f^{12}$	1	5	6	$^3H_6$	7.57	7.61
Yb^{3+}	$4f^{13}$	1/2	3	7/2	$^2F_{7/2}$	4.53	4.5
Lu^{3+}	$4f^{14}$	0	0	0	$^1S_0$	0	0

Table 2.2 Prediction of magnetic ground states of 3*d* ions using Hund's rules, $p_1 = g_J[J(J+1)]^{1/2}$, is very different from the measurements. On the other hand, $p_2 = 2[S(S+1)]^{1/2}$ agrees much better with p_{exp}, which indicated orbital quenching.

ion	shell	S	L	J	term	$p1$	p_{exp}	$p2$
Ti^{3+}, V^{4+}	$3d^1$	1/2	2	3/2	$^2D_{3/2}$	1.55	1.70	1.73
V^{3+}	$3d^2$	1	3	2	$^3F_2$	1.63	2.61	2.83
Cr^{3+}, V^{2+}	$3d^3$	3/2	3	3/2	$^4F_{3/2}$	0.77	3.85	3.87
Mn^{3+}, Cr^{2+}	$3d^4$	2	2	0	$^5D_0$	0	4.82	4.90
Fe^{3+}, Mn^{2+}	$3d^5$	5/2	0	5/2	$^6S_{5/2}$	5.92	5.82	5.92
Fe^{2+}	$3d^6$	2	2	4	$^5D_4$	6.70	5.36	4.90
Co^{2+}	$3d^7$	3/2	3	9/2	$^4F_{9/2}$	6.63	4.90	3.87
Ni^{2+}	$3d^8$	1	3	4	$^3F_4$	5.59	3.12	2.83
Cu^{2+}	$3d^9$	1/2	2	5/2	$^2D_{5/2}$	3.55	1.83	1.73
Zn^{2+}	$3d^{10}$	0	0	0	$^1S_0$	0	0	0

(2) *j-j* coupling

When the spin-orbit coupling is stronger than the coupling of individual spin-spin and individual orbit-orbit, the Russell-Saunders coupling will fail to estimate the correct total angular momentum and *j-j* coupling scheme will be used instead. This typically is used when dealing with very heavy atom since spin-orbit coupling is proportional to the atomic number to the forth order (Z^4). Under this circumstance, the orbital and spin angular momentum of each electron combine to give the resultant total angular momentum per electron (Equation 1.9).

$$j_i = l_i + s_i \tag{2.9}$$

The resultant j_i then combine to form the total angular momentum J of an atom via

$$J = \sum j_i \tag{2.10}$$

For the materials studied here, estimation of angular momentum should follow the Russell-Saunders coupling scheme.

2.2 Magnetism in Materials

From the discussion of last section, isolated magnetic moments originated from the overall contribution of both orbital and spin angular momentum of atoms. Depending on the total spin quantum number, paramagnetism ($S \neq 0$) and diamagnetism ($S = 0$, orbital magnetic moment only) are defined. Furthermore, when the magnetic moments in solid communicate with each other and form long rage ordering, ferromagnetism, antiferromagnetism and ferrimagnetism can be observed.[1-2,4] The summary of different types of magnetism is in Figure 2.4. Among different interactions in magnetism,

exchange interactions lie at the heart of the phenomenon of long range magnetic ordering and will be addressed more in detail.

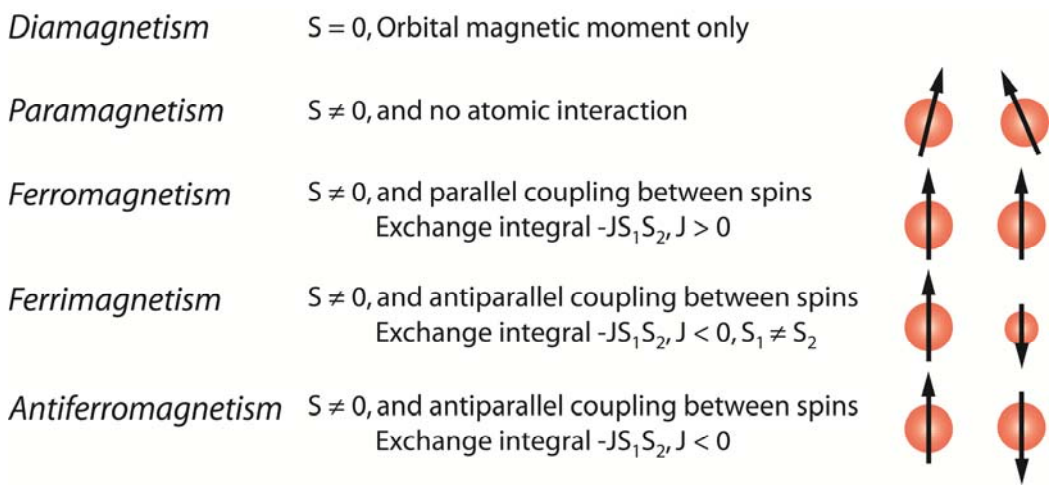

Figure 2.4. Summary of different types of magnetisms.

2.2.1 Long range ordering: exchange coupling

After Heisenberg's explanation about the singlet-triplet splitting of the excited states of Helium atoms, more calculations were preformed to explain the exchange interaction in molecules and solids. For the simplest molecular case, H_2, Heitler-London model provides a detail explanation of the origin of exchange interaction.

The H_2 Hamiltonian typically includes the kinetic energy, electron-nucleus and nucleus-nucleus Coulomb interaction and an electron-electron interaction term. To identify the exchange interaction, we first try to find a solution of the Hamiltonian without the electron-electron interaction then treat it as a perturbation later. Therefore,

the Hamiltonian can be written as follow according to the coordinates showed in Figure 2.5.

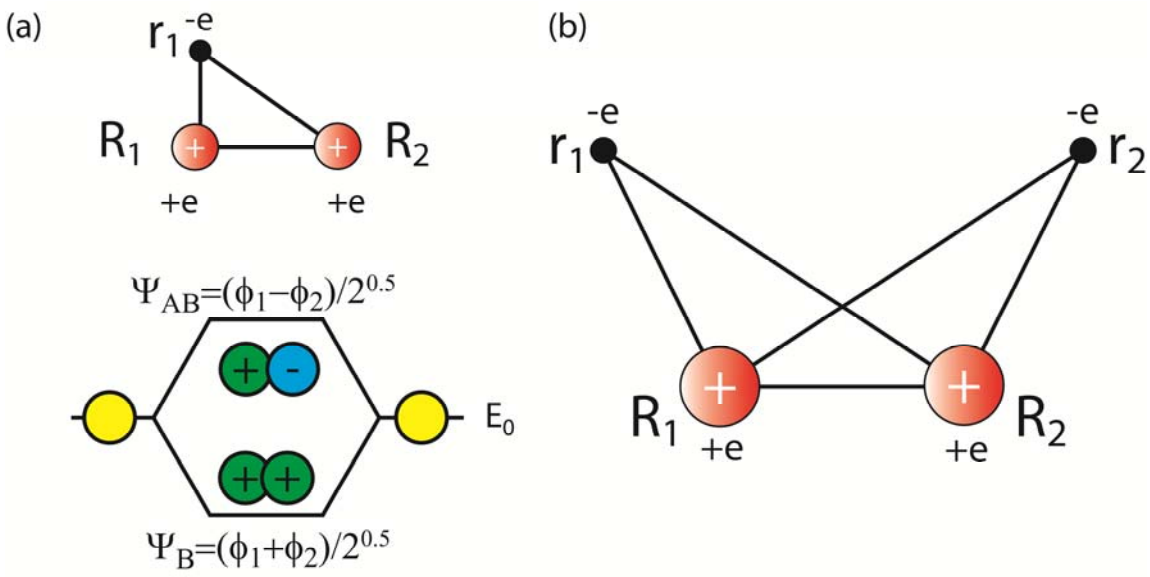

Figure 2.5. Coordinates of (a) one-electon H_2^+ molecule and (b) the two electron H_2 molecule. In (a) we give the energies and wavefunctions of the bonding and antibonding molecular states.

$$\boldsymbol{H}(\boldsymbol{r}_1,\boldsymbol{r}_2) = \underbrace{\frac{\boldsymbol{p}_1^2}{2\boldsymbol{m}_e} - \frac{\boldsymbol{e}^2}{4\pi\varepsilon_0}\left[\frac{1}{|\boldsymbol{r}_1-\boldsymbol{R}_1|}+\frac{1}{|\boldsymbol{r}_1-\boldsymbol{R}_2|}\right]}_{\boldsymbol{H}^1_{\boldsymbol{atom}}} + \underbrace{\frac{\boldsymbol{p}_2^2}{2\boldsymbol{m}_e} - \frac{\boldsymbol{e}^2}{4\pi\varepsilon_0}\left[\frac{1}{|\boldsymbol{r}_2-\boldsymbol{R}_2|}+\frac{1}{|\boldsymbol{r}_2-\boldsymbol{R}_1|}\right]}_{\boldsymbol{H}^2_{\boldsymbol{atom}}} + \frac{\boldsymbol{e}^2}{4\pi\varepsilon_0}\frac{1}{|\boldsymbol{R}_1-\boldsymbol{R}_2|} \qquad 2.11$$

Since the total symmetry of the wavefunction needs to be asymmetric, invoking the solution of one-electron linear combination of atomic orbital wavefunction of H_2^+gives us the wavefunction of H_2 as follow:

$$\Psi^{S}(\boldsymbol{r}_1\boldsymbol{s}_1;\boldsymbol{r}_2\boldsymbol{s}_2)=\frac{1}{\sqrt{2}}\left[\psi_{\boldsymbol{B}}(\boldsymbol{r}_1)\psi_{\boldsymbol{B}}(\boldsymbol{r}_2)+\psi_{\boldsymbol{B}}(\boldsymbol{r}_2)\psi_{\boldsymbol{B}}(\boldsymbol{r}_1)\right]\chi_{\boldsymbol{as}}(\boldsymbol{s}_1,\boldsymbol{s}_2) \qquad 2.12$$

$$\Psi^{T}(\boldsymbol{r}_1\boldsymbol{s}_1;\boldsymbol{r}_2\boldsymbol{s}_2)=\frac{1}{\sqrt{2}}\left[\psi_{\boldsymbol{B}}(\boldsymbol{r}_1)\psi_{\boldsymbol{AB}}(\boldsymbol{r}_2)+\psi_{\boldsymbol{B}}(\boldsymbol{r}_2)\psi_{\boldsymbol{AB}}(\boldsymbol{r}_1)\right]\chi_{\boldsymbol{sym}}(\boldsymbol{s}_1,\boldsymbol{s}_2) \qquad 2.13$$

where $\psi_{\boldsymbol{B}}$ and $\psi_{\boldsymbol{AB}}$ are bonding and antibonding wavefunction of H_2^+, $\chi_{\boldsymbol{as}}(\boldsymbol{s}_1,\boldsymbol{s}_2)$ $\chi_{\boldsymbol{s}}(\boldsymbol{s}_1,\boldsymbol{s}_2)$ and are symmetric and asymmetric spin functions given by

$$\chi_{\boldsymbol{as}}(\boldsymbol{s}_1,\boldsymbol{s}_2)=\frac{1}{\sqrt{2}}(\alpha\beta-\beta\alpha) \qquad 2.14$$

$$\chi_{\boldsymbol{s}}(\boldsymbol{s}_1,\boldsymbol{s}_2)=\begin{cases}\alpha\alpha\\ \dfrac{1}{\sqrt{2}}(\alpha\beta+\beta\alpha)\\ \beta\beta\end{cases} \qquad 2.15$$

The overlap integral S will be $\boldsymbol{S}=\left\langle\phi_1(\boldsymbol{r}_1)\phi_2(\boldsymbol{r}_2)\middle|\phi_1(\boldsymbol{r}_2)\phi_2(\boldsymbol{r}_1)\right\rangle$.

We can rewrite the singlet and triplet state solution as

$$\Psi^{\boldsymbol{S}}_{\boldsymbol{HL}}(\boldsymbol{r}_1\boldsymbol{s}_1;\boldsymbol{r}_2\boldsymbol{s}_2)=\frac{1}{2\sqrt{1+\boldsymbol{S}}}\left[\phi_1(\boldsymbol{r}_1)\phi_2(\boldsymbol{r}_2)+\phi_2(\boldsymbol{r}_1)\phi_1(\boldsymbol{r}_2)\right]\left[\alpha_1\beta_2-\beta_1\alpha_2\right] \qquad 2.16$$

$$\Psi^{\boldsymbol{T}}_{\boldsymbol{HL}}(\boldsymbol{r}_1\boldsymbol{s}_1;\boldsymbol{r}_2\boldsymbol{s}_2)=\frac{1}{2\sqrt{1-\boldsymbol{S}}}\left[\phi_2(\boldsymbol{r}_1)\phi_1(\boldsymbol{r}_2)+\phi_1(\boldsymbol{r}_1)\phi_2(\boldsymbol{r}_2)\right]\chi_{\boldsymbol{sym}} \qquad 2.17$$

By using Heitler-London singlet and triplet functions one obtains the energies

$$\boldsymbol{E}^{\boldsymbol{S}}=\frac{\left\langle\Psi^{\boldsymbol{S}}_{\boldsymbol{HL}}\middle|\boldsymbol{H}(\boldsymbol{r}_1,\boldsymbol{r}_2)\middle|\Psi^{\boldsymbol{S}}_{\boldsymbol{HL}}\right\rangle}{\left\langle\Psi^{\boldsymbol{S}}_{\boldsymbol{HL}}\middle|\Psi^{\boldsymbol{S}}_{\boldsymbol{HL}}\right\rangle}=2\boldsymbol{E}_0+\frac{\boldsymbol{C}+\boldsymbol{X}}{1+\boldsymbol{S}} \qquad 2.18$$

and

$$\boldsymbol{E}^{\boldsymbol{T}} = \frac{\left\langle \Psi_{\boldsymbol{HL}}^{\boldsymbol{T}} \middle| \boldsymbol{H}(\boldsymbol{r}_1, \boldsymbol{r}_2) \middle| \Psi_{\boldsymbol{HL}}^{\boldsymbol{T}} \right\rangle}{\left\langle \Psi_{\boldsymbol{HL}}^{\boldsymbol{T}} \middle| \Psi_{\boldsymbol{HL}}^{\boldsymbol{T}} \right\rangle} = 2\boldsymbol{E}_0 + \frac{\boldsymbol{C} - \boldsymbol{X}}{1 - \boldsymbol{S}} \qquad 2.19$$

where E_0 is the atomic energy of the H atom, which is given by

$$\boldsymbol{E}_0 = \left\langle \phi_1(\boldsymbol{r}_1) \middle| \boldsymbol{H}_{\boldsymbol{atom}}^1 \middle| \phi_1(\boldsymbol{r}_1) \right\rangle = \left\langle \phi_2(\boldsymbol{r}_2) \middle| \boldsymbol{H}_{\boldsymbol{atom}}^2 \middle| \phi_2(\boldsymbol{r}_2) \right\rangle \qquad 2.20$$

C is the Coulomb integral

$$\boldsymbol{C} = \left\langle \phi_1(\boldsymbol{r}_1)\phi_2(\boldsymbol{r}_2) \middle| \boldsymbol{H}' \middle| \phi_1(\boldsymbol{r}_1)\phi_2(\boldsymbol{r}_2) \right\rangle \qquad 2.21$$

and X is the exchange integral

$$\boldsymbol{X} = \left\langle \phi_1(\boldsymbol{r}_1)\phi_2(\boldsymbol{r}_2) \middle| \boldsymbol{H}' \middle| \phi_1(\boldsymbol{r}_2)\phi_2(\boldsymbol{r}_1) \right\rangle \qquad 2.22$$

It is worthy to point out that the exchange integral between two atoms falls off rapidly with increasing nuclear distance, which indicates the short-range interaction nature for magnetism.

Comparing equation 2.18 and 2.19, we obtain the singlet-triplet splitting as:

$$\boldsymbol{E}^{\boldsymbol{S}} - \boldsymbol{E}^{\boldsymbol{T}} = 2\boldsymbol{J} = 2\frac{\boldsymbol{X} - \boldsymbol{SC}}{1 - \boldsymbol{S}^2} \qquad 2.23$$

The results from Heitler-London model were connected to spin quantum number by Heisenberg where he rewrote the effective Hamiltonian in the form

$$\boldsymbol{H}_{\boldsymbol{eff}} = 2\boldsymbol{H}_0 + \boldsymbol{H}_{\boldsymbol{coul}} + \boldsymbol{H}_{\boldsymbol{exch}}, \qquad 2.24$$

where H_0 and H_{coul} corresponds to E_0 and C in equation 2.18 and 2.19. The exchange energies X are the singlet and triplet expectation values of the exchange Hamiltonian

H_{exch}. By extension of the two-spin Hamiltonian, the effective Heisenberg Hamiltonian for a many-electron system can be expressed as follows:

$$\boldsymbol{H}_{exch} = -\sum_{i \neq j}^{N} \boldsymbol{J}_{ij} \boldsymbol{s}_i \boldsymbol{s}_j = -2\sum_{i<j}^{N} \boldsymbol{J}_{ij} \boldsymbol{s}_i \boldsymbol{s}_j \qquad 2.25$$

If the electrons on neighboring magnetic atoms interact via an exchange interaction, this is known as direct exchange. In general, direct exchange is less common due to its distance dependence. On the other hand, in numbers of ionic solids, including our model system used in this study, exchange interaction actually was carried out via a non-magnetic atom. This situation is referred to as indirect exchange which includes superexchange, double exchange and RRKY exchange. Here we will discuss the first two in detail since they are particularly important in our system.

(1) Superexchange

Superexchange can be defined as an indirect exchange interaction between non-neighboring magnetic ions which is mediated by a non-magnetic ion placed in between the magnetic ions. It arises because there is a kinetic energy advantage for anti-ferromagnetism as shown in Figure 2.6, where we assume the metal atoms are magnetic due to a single unpaired electron. The arrows show the spins of the four electrons and how they are distributed over the transition metal (M) and oxygen (O) atoms.

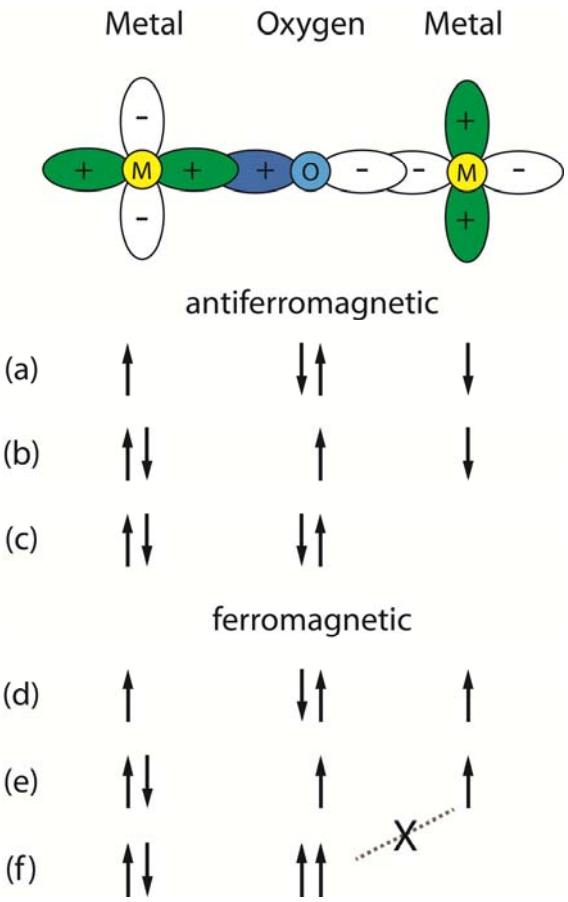

Figure 2.6. Illustration of superexchange interaction in a magnetic oxide. If the moments on the transition metal atoms are coupled antiferromagnetically (a,b,c), the ground state is (a) and this can mix with excited configuration (b) and (c). The magnetic electrons can be delocalized over the M-O-M, lowering the kinetic energy. If the moments of M are coupled ferromagnetically, the ground state (d) can not mix with other excited states like (e) and (f) due to exclusion principle. Such superexchange interaction therefore results in antiferromagnetic coupling of magnetic moments between metals.

If a system has a finite probability to be in several states, the true ground state wavefunction should be a linear combination of the states. In the case where the moments on the transition metal atoms are coupled antiferromagnetically (Figure 2.6(a), (b), and (c)); the ground state (a) can mix with excited configurations (b) and (c). The magnetic electrons can delocalize over the M-O-M and thus lower the kinetic energy. On the other hand, if the magnetic moments of the metal atoms are coupled ferromagnetically (Figure 2.6(d), (e), and (f)), the ground state (d) can not mixed with excited configurations (e) and (f) due to Pauli exclusion principle. The ferromagnetic configuration therefore costs more energy.

Such kinetic energy favorable term is called *kinetic exchange* which dominated in superexchange interaction and depended on M-O orbital overlap and the angle of the M-O-M bond. Furthermore, it also accounts for the favorable antiferromagnetic configuration in magnetic transition metal oxide materials.

(2) Double exchange

The indirect exchange interaction can also be ferromagnetic. This typically occurs in materials containing mixed valency metal ions and referred as double exchange. In this case, electron from one metal ion hops to another ion through an intervening O^{2-}. (Figure 2.7) Since the *p*-orbitals are fully occupied, the process has to proceed in two steps (an electron from O to one metal ion then another electron from the other metal ion to vacated O orbital) and thus named “double exchange”. Magnetite (Fe_3O_4) is a good example showed double exchange, where Fe^{2+} ($3d^6$) and Fe^{3+} ($3d^5$) are located at tetrahedral site of the crystal. When electron hopping process occurred, the spin needs to

be conserved. Under this circumstance, only two metal ion coupled ferromagnetically will allow the electron hopping between metals ions and result in energetically more favorable state as shown in Figure 2.7. In face, both superexchange and double exchange exist in magnetite, the Fe^{3+} in tetrahedral site and octahedral site coupled by superexchange and Fe^{2+} and Fe^{3+} in tetrahedral site coupled by double exchange interaction. Thus the magnetic moments of two Fe^{3+} cancelled out and left a net moment due to the Fe^{2+} alone. The measured magnetic moment per formula unit is very close to the expected 4 μ_B due to just the Fe^{2+} ions.

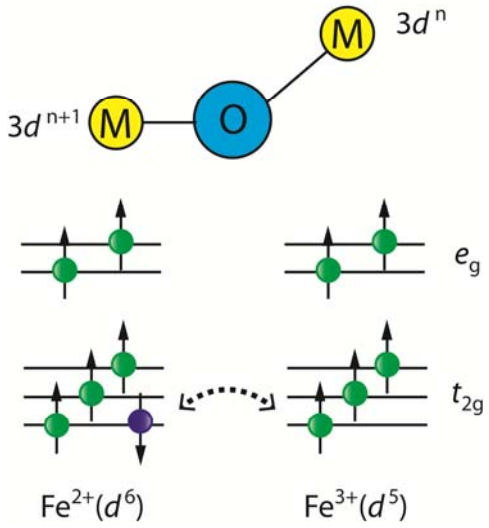

Figure 2.7. Illustration of indirect ferromagnetic exchange coupling (double exchange) for bonding of two 3*d* metal atoms M with different occupations $3d^{n+1}$ and $3d^{n}$ through an O atom.

2.2.2 Magnetism in nanoscale: superparamagnetism

When the volumes of ferro- or ferrimagnetic materials are reduced, the surface energies become progressively more important in overall contribution to the energy of the systems. This results in the removal of domain walls in the material and makes the material consist of a single magnetization domain. In ferromagnetic transition metals such as Fe, Co, and Ni, the characteristic size is around 100 nm.

The magnetization of such a small particle is often constrained to lie parallel or antiparallel to a particular direction. To be more quantitative, consider an assembly of uniaxial, single-domain particles, each with an anisotropy energy $E = K\sin^2\theta$ according to Stoner-Wohlfarth model, where K is the anisotropy constant and θ is the angle between magnetization and easy axis. If the volume of each particle is V, then the energy barrier needs to be overcome before a particle can reverse its magnetization (for example $\theta = 0$ to π or π to 0) will be KV (see Figure 2.8).

As the particle size is reduced to nanometer scale, KV would became so small that thermal energy fluctuation of the surrounding could overcome the anisotropy energy and spontaneously rotate the magnetization of the particle. While the external field is applied, the magnetic moments of particles will be aligned whereas thermal energy will tend to disalign them. This is very similar to the behavior of normal paramagnetic materials. However, the magnetic moment of a normal paramagnetic is only a few μ_B but that of the particle is 4 to 5 order magnitudes higher. As a result, *superparamagnetism* is used to describe the phenomena of magnetic behavior of small particles.

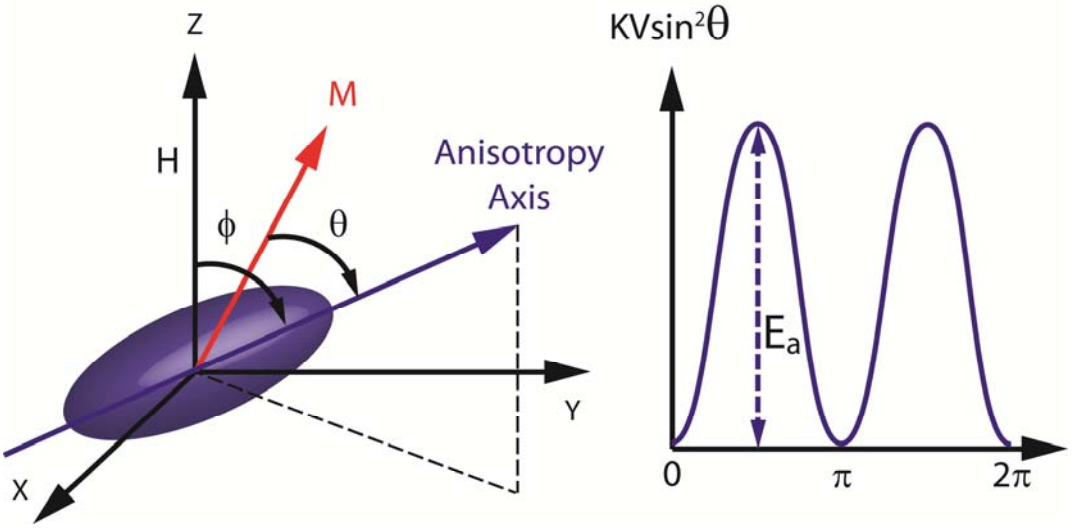

Figure 2.8. Left panel: System coordination showing the anisotropy axis in 3-dimension for an assembly of uniaxial, single-domain particles. Right panel: direction of magnetization of a material with single domain is limited by the anisotropic energy.

Superparamagnetic materials always show two distinct behaviors when they are superparamagnetic. First, magnetization curves measured at different temperatures are superimposed when M is plotted versus H/T. Second, there is no hysteresis. However, these behaviors are also dependent on the particle size, temperature and external field. To determine these critical values of temperature or size, we need to consider how quickly the system reaches its thermal equilibrium. Consider a distribution of particles brought to an initial magnetization state $\mathbf{M_i}$ by an applied field and the field is then removed at time zero. Once the field is turned off, magnetizations of some particles will immediately reverse due to the fact that thermal energy of surrounding is much larger

than the anisotropy energy gaps of the particles. The time-dependent magnetizations of particles can be expressed as

$$-\frac{dM}{dt} = f_0 M e^{-KV/k_B T} = \frac{M}{\tau} \qquad 2.26$$

where f_0 is the frequency factor and τ is the relaxation time. The time-dependent remanence $\mathbf{M_r}$ can be obtained via integrating equation 2.26 and will be $M_r = M_i e^{-t/\tau}$. Therefore, the τ represents the time for $\mathbf{M_r}$ to decrease to 1/e (or 37%) of its initial value. From equation 2.26, the relaxation time τ of the particle can be related to the particle volume V and temperature T as follows

$$\frac{1}{\tau} = f_0 \exp\left(\frac{-KV}{k_B T}\right) \qquad 2.27$$

Typically f_0 has a value of about 10^{-9} sec^{-1}. Defining stable state of relaxation is somewhat arbitrary and usually τ = 100 seconds. With this value of f_0 and τ, for a given size particle, there will be a temperature, $\mathbf{T_B}$, called the blocking temperature, below which the magnetization will be stable. For uniaxial particles,

$$T_B = \frac{KV}{25 k_B} \qquad 2.28$$

One thing we need to be more careful about is that equation 2.28 is only valid when the interparticle interaction is negligible. Furthermore, if the particles are not monodispersed, the distribution of the particle size results in a distribution of blocking temperature as well.

Like the case in paramagnetism, the magnetization of superparamagnetic material along the applied field can be calculated via a simple spherical model (as shown in Figure 2.9), assuming the magnetic moments of the particle can point along any direction. Consider a unit volume of material containing *n* atoms and each has magnetic moment μ. Let the direction of each moment be represented by a vector, and let all the vectors be drawn through the center of a sphere of unit radius. The number of magnetic moments directing a given direction will be simply proportional to the area they occupied on the sphere.

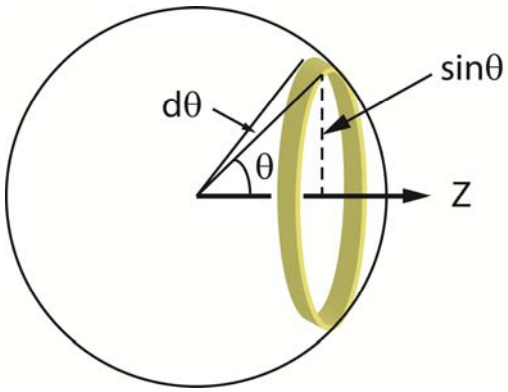

Figure 2.9. The fraction of paramagnetic moments between angles θ and $\theta + d\theta$ around the *z*-axis is equal to the fractional area that the $d\theta$ sweeps out on the surface of the sphere.

In the absence of the magnetic field, the number of magnetic moment vector in a given area $\boldsymbol{dA}$ will be all the same ($\boldsymbol{dA} = 2\pi \sin\theta \boldsymbol{d}\theta$ for a sphere of unit radius) at any

place on the sphere. However, when the field is applied along *z* direction, each atom has a potential energy $\boldsymbol{E_p} = -\mu \boldsymbol{H} \cos\theta$. For a given temperature T, the probability of an atom having energy $\boldsymbol{E_p}$ is proportional to the Boltzmann factor $\boldsymbol{e}^{-\boldsymbol{E_p}/\boldsymbol{k_B T}}$, where k_{B} is the Boltzmann constant. Therefore, the number of magnetic moment vectors in a given area for a given temperature will be simply the product of area and the Boltzmann distribution. The average moment along *z* direction is then

$$\langle \mu_z \rangle = \frac{\int_0^{\pi} \mu \cos\theta \exp(\mu \boldsymbol{H} \cos\theta / \boldsymbol{k}_{\mathrm{B}} \boldsymbol{T}) \sin\theta \boldsymbol{d}\theta}{\int_0^{\pi} \exp(\mu \boldsymbol{H} \cos\theta / \boldsymbol{k}_{\mathrm{B}} \boldsymbol{T}) \sin\theta \boldsymbol{d}\theta} \tag{2.29}$$

$$= \mu \frac{\int_{-1}^{1} \boldsymbol{x} \boldsymbol{e}^{\boldsymbol{y}\boldsymbol{x}} \boldsymbol{d}\boldsymbol{x}}{\int_{-1}^{1} \boldsymbol{e}^{\boldsymbol{y}\boldsymbol{x}} \boldsymbol{d}\boldsymbol{x}}, \tag{2.30}$$

where $\boldsymbol{y} = \mu \boldsymbol{H} / \boldsymbol{k}_{\mathrm{B}} \boldsymbol{T}$ and $\boldsymbol{x} = \cos\theta$. This leads to

$$\frac{\langle \mu_z \rangle}{\mu} = \coth \boldsymbol{y} - \frac{1}{\boldsymbol{y}} \equiv \boldsymbol{L}(\boldsymbol{y}), \tag{2.31}$$

where $\boldsymbol{L}(\boldsymbol{y}) = \coth \boldsymbol{y} - \frac{1}{\boldsymbol{y}}$ is called the Langevin function. From equation 2.31, once we know the field strength and temperature, the magnetization curve of the material can be estimated. In our study, we also apply Langevin function to estimate the temperature effects on magnetization of superparamagnetic nanocrystals.

2.3 Laser Induced Magnetization Dynamics

Fundamental study of magnetization dynamics typically is based on probing the magnetic system after certain perturbations. The three most common ways to disturb the magnetic system include (1) applying magnetic field, (2) laser heating and (3) spin-select

excitation by polarized light as shown in Figure 2.10. Even though different perturbations may result in the same effect, i.e. demagnetization, the microscopic mechanism is different for these perturbations. For example, when a sudden change of magnetic field is applied, a difference between different spin direction is generated (Figure 2.10(a)). When the perturbation is induced via heating a ferromagnetic material by a heating laser pulse, the energy of the photons is transferred to electronic degrees of freedom to create hot electrons (Figure 2.10(b)). The third perturbation represents a more direct interplay between photons and spins. When using circularly polarized light, spin-selective excitation directly changes the magnetization of materials (Figure2.10(c)).

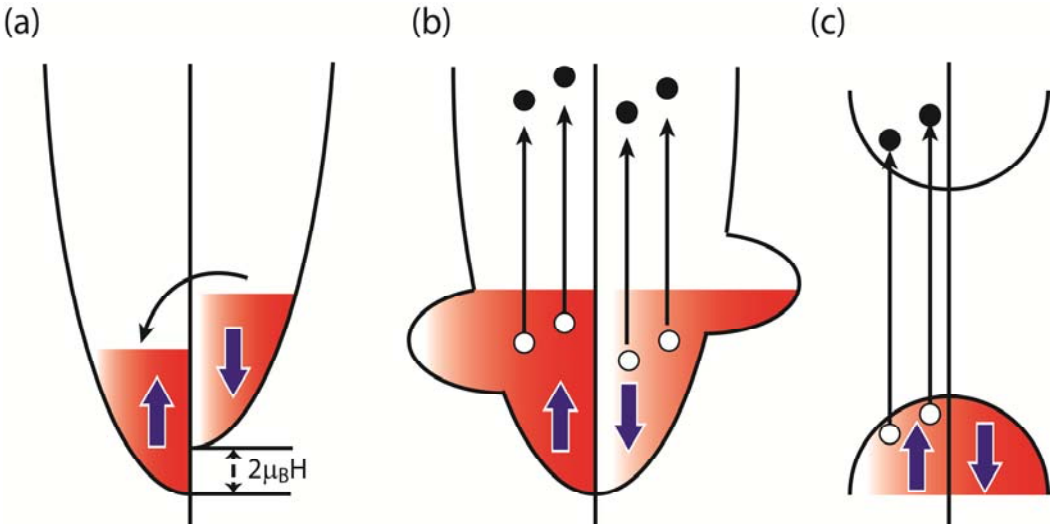

Figure 2.10. Perturbation of magnetic system can be achieved via (a) magnetically pumping, (b) laser heating and (c) spin-selective excitation.

To study different laser induced magnetization dynamics, various time domain spectroscopy techniques have been applied: (1) employing magneto-optic effect such as Faraday effect or Kerr effect, (2) inducing the emission of photoelectrons with higher energy (UV) photon pulses, and (3) Utilizing X-ray dichroism. Generally speaking, a number of well-discernible time scales have been identified in ferromagnetic materials after photoexcitation, which includes fast laser induced demagnetization (hundreds of femtoseconds) and slower processes (>100ps) such as magnetic precession, spin-lattice-driven demagnetization, and spin-lattice relaxation. In the following section, a brief review of main ultrafast magnetization dynamics studies on metallic, semiconducting and insulating ferromagnets after photoexcitation will be presented.

Ultrafast demagnetization in a metallic magnet was first reported by Bigot's group via time-resolved magneto-optic Kerr effect (TRMOKE). The ratio of rotation of the plane polarization of the linearly polarized probe with and without pump pulse excitation as a function of pump-probe time delay is used to represent the time dependent remanent magnetization in the Ni film (Figure 2.11).[5] The result is interpreted as an ultrafast loss of the magnetic ordering of the ferromagnetic material within a picosecond after laser excitation. The experiment finding of an ultrafast demagnetization was confirmed by several other groups. For example, Hohfeld et al. applied time-resolved second-harmonic generation (SHG), and Scholl et al. use time-resolve photoemission (TRPE) to study magnetization dynamics of Ni film under various excitation intensities.[6-7] This ultrafast magnetic response was explained by an effective electron-spin interaction mechanism among the strongly nonequilibrium electrons, leading to a rapid increase of

the spin temperature and destruction of magnetization. This observation triggered the interest of several groups and similar experiments have been conducted in other material systems.

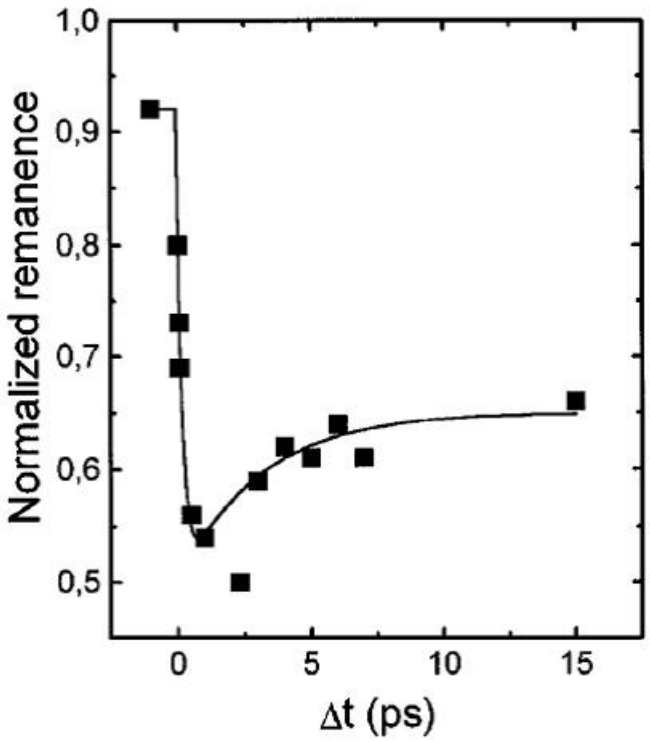

Figure 2.11. Time-resolved magneto-optic Kerr effect signal from a remanently magnetized polycrystalline Ni film after heating by a 60 fs laser pulse. Figure adapted from Beaurepaire's work.[5]

On the other hand, the slower processes (> 100ps) were attributed to various mechanisms such as magnetic precession, strain, spin-lattice related demagnetization or spin-lattice relaxation. Vaterlaus et al. measured the spin-lattice relaxation time of

ferromagnetic Gd via time-resolved spin polarized photoemission measurements.[8] In their study, the demagnetization resulted from the 10 ns heating pulse and the typical time for spin lattice relaxation is ~100 ps.

CHAPTER III

SAMPLE PREPARATION AND EXPERIMENTAL TECHNIQUES

This chapter presents the details of the sample preparation and characterization ,and approaches that allow us to access the study of magnetization dynamics. Wet chemical synthesis procedures and static physical properties of $Co_xFe_{3-x}O_4$ nanocrystals are introduced. Phenomenological origin of magneto-optic effect, magneto-optical response of magnetic material, experimental setup of static and time-resolved Faraday rotation measurement, measurement procedures and magnetic origin of the signal will be discussed

3.1 Sample Synthesis

3.1.1 Synthesis of Fe_3O_4 nanocrystals

The synthesis of Fe_3O_4 nanocrystals with average size smaller than 10 nm is done by employing the established one-pot synthetic methods.[9-11] The reaction scheme is summarized in Figure 3.1. For the synthesis of 5 nm Fe_3O_4 nanocrystals, 2 mmol of iron(Ⅲ) actylacetonate ($Fe(acac)_3$, 97%), 10 mmol of 1,2-dodecanediol (90%), 6 mmol of oleic acid (technical grade, 90%) and 6 mmol oleylamine (technical grade, 70%) were added in a 100 ml three-neck round-bottle flask. After injecting 20 ml of phenyl ether (99%), the chemicals were mixed via vigorously stirring the solution. The round-bottle flask is then attached to a condenser and thermal couple and connected to a Schlenk line system (Figure 3.2). Nitrogen environment for reaction is achieved via pumping and

purging nitrogen gas three times. The reaction temperature is then raised to 200 °C for 1 hour. The color of the solution changes from red to black due to the decomposition of $Fe(acac)_3$ and the formation of monomer for Fe_3O_4 nanocrystals. Reaction temperature is then further increased to 250 °C and maintained at this temperature for 30 minutes to obtain 5 nm Fe_3O_4 nanocrystals. After cooling down to room temperature, the reaction solution was poured into 20 ml ethanol solution and centrifuged for 10 minutes. The black 5 nm Fe_3O_4 nanocrystals precipitate was cleaned by the repeated precipitation and resuspension with ethanol and hexane, respectively.

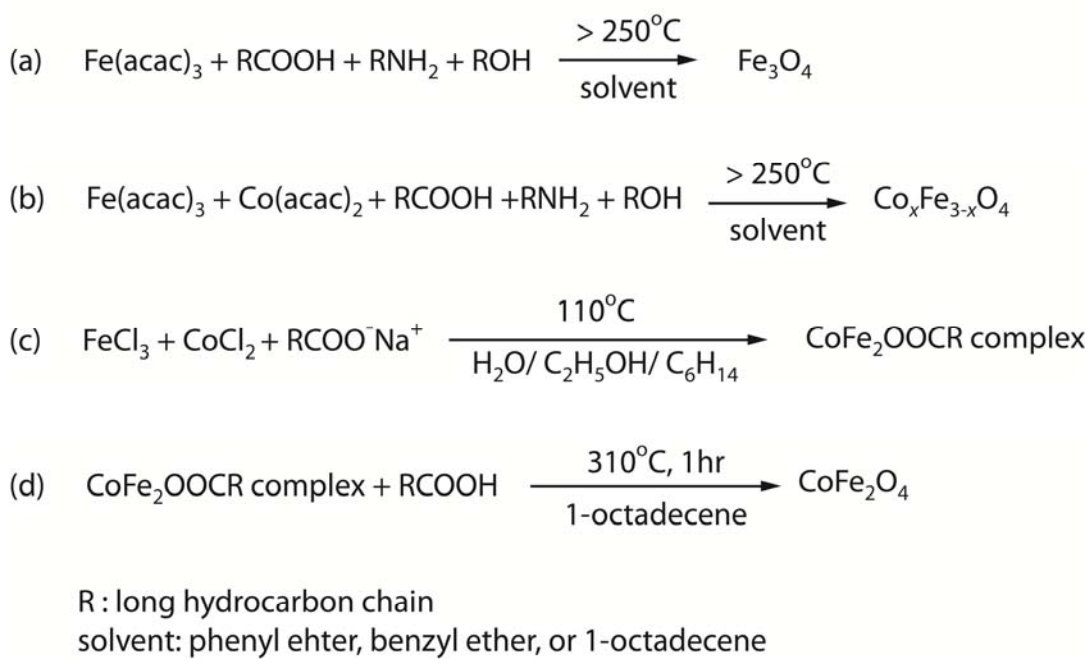

Figure 3.1. Synthetic schemes of $Co_xFe_{3-x}O_4$ nanocrystals: (a) for 5-15 nm Fe_3O_4 nanocrystals, (b) for $x < 0.6$ $Co_xFe_{3-x}O_4$ nanocrystals, (c) and (d) for $CoFe_2O_4$ nanocrystals.

The synthesis of larger nanocystals was achieved by modifying the reaction temperature and solvent. For example, 7 nm Fe_3O_4 nanocrystals can be synthesized via keeping the monomer growth at 290 °C for 1 hour in benzyl ether. However, to optimize the shape and size distribution, this method can only be applied to particle diameter smaller than 10 nm. For nanocrystals with diameter larger than 10 nm, seeded-growth method was adapted. In short, the smaller nanocrystals (for example, 7 nm Fe_3O_4 nanocrystals) were added into the reaction solution described above. At the growth stage, the nanocrystal is like a seed so that the monomer can keep growth on the nanocrystal and enlarge the size of the nanocrystal.

Figure 3.2. Typical setup for $Co_xFe_{3-x}O_4$ nanocrystals synthesis.

3.1.2 Synthesis of $Co_xFe_{3-x}O_4$ nanocrystals

The similar methods were also applied for the synthesis of the spherical $Co_xFe_{3-x}O_4$ nanocrystals with varying cobalt content (x) in the range of $0 < x < 0.53$. Different stoichiometries and sizes of $Co_xFe_{3-x}O_4$ nanocrystals are achieved by varying the molar ratio of $Fe(acac)_3$ and cobalt (II) actylacetonate ($Co(acac)_2$) and growth temperature and time, respectively.

Synthesis of high cobalt content $Co_xFe_{3-x}O_4$ nanocrystals is carried out by using a mix-metal complex. (See Figure 3.1) The mixed-metal ($Co^{2+}Fe_2^{3+}$)-oleate complex was prepared by the reaction of sodium oleate ($C_{18}H_{33}O_2Na$) and a mixture of iron and Cobalt chlorides. In a typical synthesis, 4 mmol of iron chloride ($FeCl_3$), 2 mmol of cobalt chloride ($CoCl_2$), 16 mmol of sodium oleate, 10 mL of H_2O, 10 mL of ethanol, and 20 mL of hexane were mixed and refluxed at 60 °C for 4 h. When the reaction is complete, the solution is poured into a separatory funnel. The mixed ($Co^{2+}Fe_2^{3+}$)-oleate complex was obtained by separation of the water phase and subsequent evaporation of the residual ethanol and hexane at 70 °C and water at 110 °C over night.

Five grams of the mixed-metal ($Co^{2+}Fe_2^{3+}$)-oleate complex, 20 mL 1-octadecene, and 0.5 g oleic acid were then mixed and magnetically stirred for 1 h under flowing N_2. The mixture was then heated to 310 °C at a heating rate of 1 °C/min and maintained at this temperature for 60 min under N_2 flow with continuous stirring. The reaction mixture was subsequently cooled to room temperature and precipitated with a 20 mL ethanol/hexane (volume ratio = 3:1) solution.

3.2 Static Physical Property Characterization

3.2.1 Size and crystal structure of $Co_xFe_{3-x}O_4$ nanocrystals

The average sizes of nanocrystals were determined by transmission electron microscopy (TEM). Figures 3.3 and 3.4 show the TEM images of $Co_xFe_{3-x}O_4$ nanocrystals of different sizes (x = 0, diameter: 5, 7, 9, and 15 nm) and chemical composition (x = 0.09, 0.18, 0.3, and 0.9). All the $Co_xFe_{3-x}O_4$ nanocrystals have nearly spherical shape and the size dispersion is less than 10%.

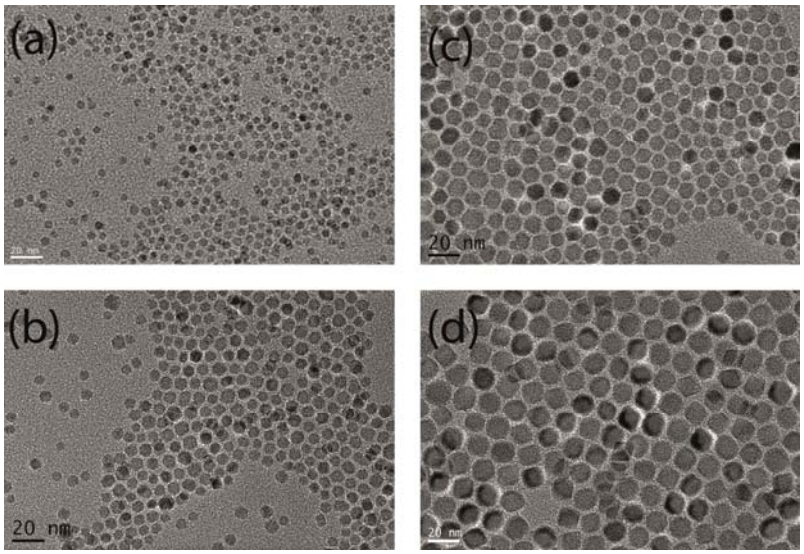

Figure 3.3. TEM images of Fe_3O_4 nanocrystals with different sizes, 5, 7, 9, 15 nm for a-d, respectively.

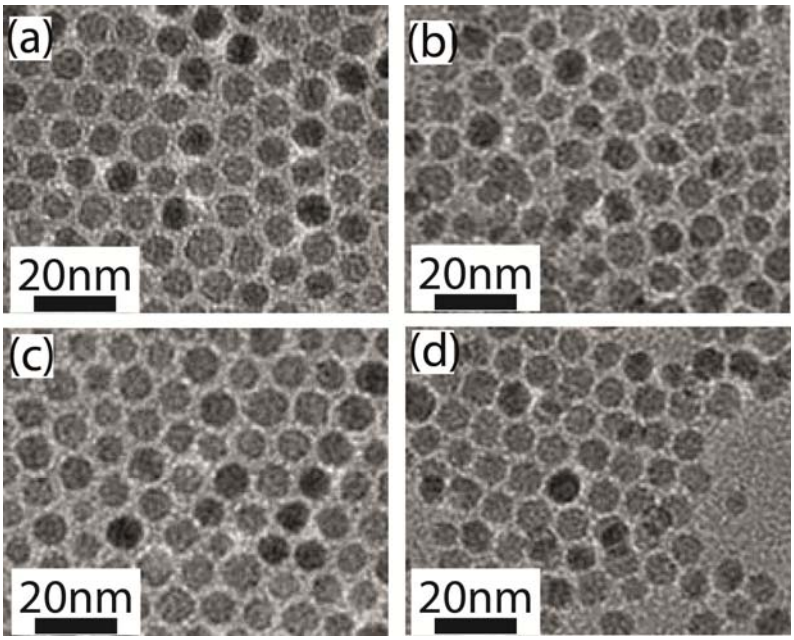

Figure 3.4. TEM images of $Co_xFe_{3-x}O_4$ nanocrystals with x = 5, 7, 9, 15 nm for a-d, respectively.

The crystal structure of Fe_3O_4 nanocrystals was confirmed by X-ray diffraction crystallography (XRD). In bulk phase, both Fe_3O_4 and $CoFe_2O_4$ have inverse spinel crystal structure. The inverse spinel structure has chemical composition AB_2O_4, where the oxide anions are arranged in a cubic close-packed lattice (fcc) and the cations are occupying the tetrahedral (A) and octahedral (B) sites in the lattice. For bulk $Co_xFe_{3-x}O_4$, Co^{2+} just simply replaces Fe^{2+} in the octahedral site without affecting the crystal structure. Figure 3.5 show the XRD patterns of $Co_xFe_{3-x}O_4$ nanocrystals. All materials showed a very similar XRD pattern, consistent with the identical crystal structures (cubic inverse spinel) of Fe_3O_4 and $CoFe_2O_4$ with < 0.2% difference in bulk lattice parameters: a = 8.391 and 8.381 Å for Fe_3O_4 and $CoFe_2O_4$, respectively.

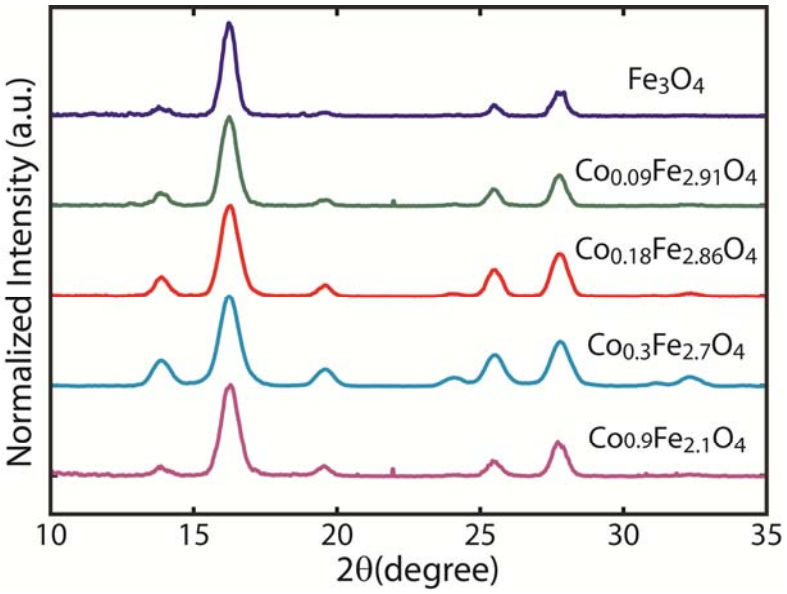

Figure 3.5. XRD data of 7 nm $Co_xFe_{3-x}O_4$ nanocrystals.

3.2.2 Absorption spectra of $Co_xFe_{3-x}O_4$ nanocrystals

The $Co_xFe_{3-x}O_4$ nanocrystal is a mixed-valence metal oxide. Its crystals appear black and absorb light from the UV to NIR region. Due to the oxygen nuclei around the metallic ion, the *d* electron becomes localized and thus most of the absorptions at Vis and NIR region are originating from intervalence charge transfer transition. For higher energy region, the absorptions are from the combination of intersublattice charge transfer and localized *d-d* transitions as shown in Figure 3.6.

Cobalt and iron ions content in $Co_xFe_{3-x}O_4$ nanocrystals were determined via elemental analysis of the nanocrystal samples employing inductively coupled plasma atomic emission spectroscopy (ICP-AES). For this measurement, dried $Co_xFe_{3-x}O_4$ nanocrystals samples were digested in 1 ml of aqueous (12 M) HCl solution. The

solution, further diluted to a ppm level of metal ion concentration in 1% aqueous HNO_3 solution, was used to measure both Fe and Co ion concentrations.

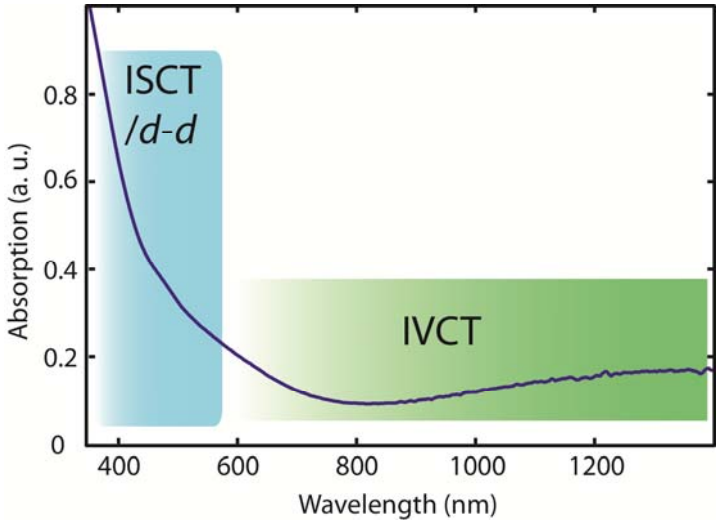

Figure 3.6. UV-Vis-NIR absorption spectrum of $Co_xFe_{3-x}O_4$ nanocrystals and the corresponding electronic transitions.

3.2.3 Static magnetic properties of $Co_xFe_{3-x}O_4$ nanocrystals

The static mass magnetization of $Co_xFe_{3-x}O_4$ nanocrystal samples was measured by using a superconducting quantum interference device (SQUID) magnetometer (MPMS-XL, Quantum Design). Saturation magnetization of $Co_xFe_{3-x}O_4$ nanocrystal samples was obtained from the field-dependent magnetization measurement at the temperature of 5 K. Similar to the results from previous studies, the saturation magnetization exhibited only a very weak dependence on cobalt content (< 4%).

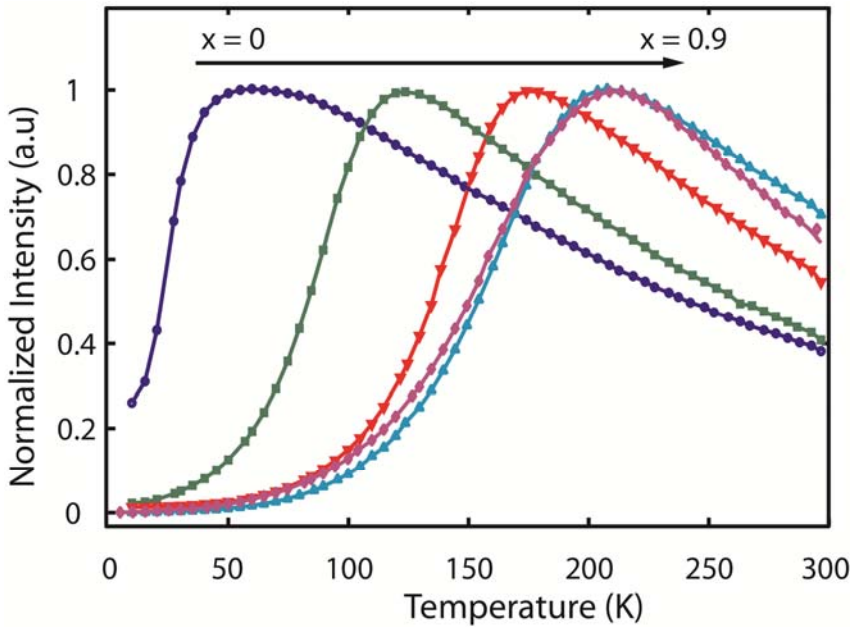

Figure 3.7. Zero-field cooling (ZFC) data of $Co_xFe_{3-x}O_4$ nanocrystals. The blocking temperatures (T_B) were determined by the peak vale of each curve. T_B increases as x increases due to stronger intrinsic spin-orbit coupling strength.

In order to estimate the magnetic anisotropy constant (K_{aniso}) of the nanocrystals, blocking temperature (T_B) was also obtained from the zero-field-cooled (ZFC) magnetization measurement within the temperature range of 10-300 K. In the ZFC curve, the temperature at which the magnetization reaches the maximum value was taken as T_B (Figure 3.7). The magnetic anisotropy constant (K_{aniso}), partially reflecting the strength of spin-orbit coupling was obtained from $K_{aniso} = 25k_BT_B/V$, where k_B is Boltzmann constant and V is the volume of the nanocrystal. The chemical composition dependent blocking temperature and anisotropy energy results were summarized in Table 3.1. For all the SQUID measurements, the nanocrystal samples were dispersed in liquid eicosane

to avoid the aggregation and subsequently solidified to prevent the agitation of the nanocrystals in the matrix during the measurements.

Table 3.1. Chemical composition dependent blocking temperature and anisotropy energy of 7 nm $Co_xFe_{3-x}O_4$ nanocrystals.

x	0	0.09	0.18	0.3	0.9
TB	65	125	175	210	230
K x10^6 (erg/cm^3)	1.25	2.40	3.36	4.03	4.42

3.3 Experimental Setup of Magneto-optical Faraday Effect

3.3.1 Magneto-optical Faraday effect

The magneto-optical effect arises from the interaction between light and a matter which is magnetic or subjected to a magnetic field.[12] The presence of a magnetic field changes the dispersion curves of the absorption coefficient due to Zeeman effect and thus leads to the appearance or variation of optical anisotropy. To probe magneto-optical response of materials, the Faraday and Kerr effects are widely adapted. For the Faraday effect, the magneto-optic response of magnetized material manifests itself in the *transmission* of light passing through the medium. On the other hand, for the Kerr effect, optical anisotropy of a magnetized medium manifests itself in the *reflection* of light from its surface. Here we will only focus on the transmission type magneto-optical effect

(Faraday effect) and will introduce a few different magneto-optic response in more detail in the following section.

Basic magneto-optic phenomena of Faraday effect can be classified according to few things: relative orientation of wavevector $\vec{k}$ of the light and magnetic field $\boldsymbol{H}$ and ways to manifest the Zeeman effect. According to the relative orientation of wavevector $\vec{k}$ of the light and magnetic field $\boldsymbol{H}$, Faraday effect presents in two different geometries:

(1) Faraday geometry: the light travels along the field direction. ($\vec{k} \parallel \boldsymbol{H}$)

(2) Voigt geometry: the light travels perpendicular to the field direction. ($\vec{k} \perp \boldsymbol{H}$)

In both geometry the Zeeman effect is studied, however, the Faraday geometry obtained the information in longitudinal mode and Voigt geometry in transverse mode.

When light passes through a medium, the Faraday effect can be reflected from the dispersion of refractive index or the absorption of the incident light and results in birefringence and dichroism. For example, under $\vec{k} \parallel \boldsymbol{H}$ geometry, a linearly polarized light (can be represented as a superposition of right-hand and left-hand polarized waves) passed through a magnetic material and rotates the plane of polarization due to the different refractive index (the right- and left-hand waves propagates with different velocities) between right- and left-hand waves. This magneto-optic phenomenon is called magnetic circular birefringence (MCB) or Faraday rotation. On the other hand, under the same situation, if a medium exhibits different absorptions of right- and left-hand circularly polarized waves, as a linearly polarized light passed through a magnetic material, its polarization is changed from linear to elliptical. This magneto-optic

phenomenon is called magnetic circular dichroism (MCD). Similar analysis can be applied to the Voigt geometry ($\vec{k} \perp \boldsymbol{H}$) for magnetic linear birefringence (MLB) and magnetic linear dichroism (MLD), a summary of different mageto-optic phenomena of Faraday effect is shown in Figure 3.8. Since experiments carried out in this dissertation are always in Faraday geometry, we will discuss the magnetic circular birefringence and magnetic circular dichroism more quantitatively.

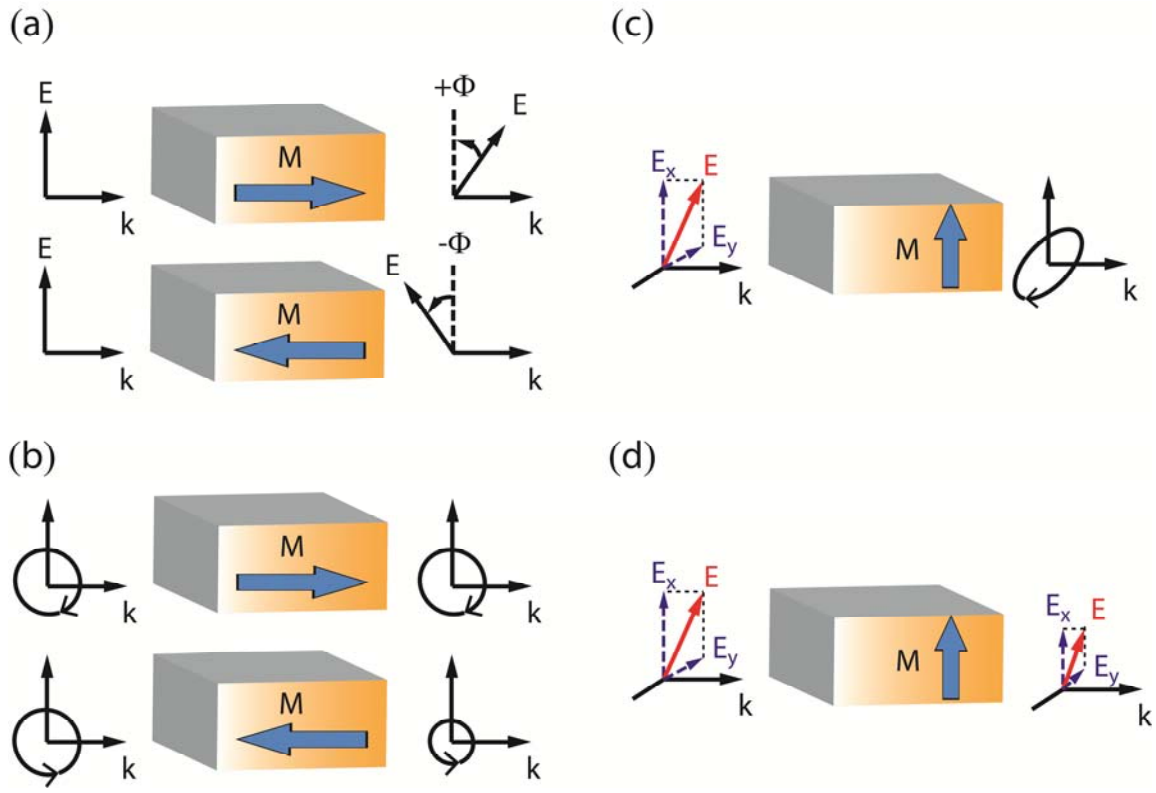

Figure 3.8. Summary of different magneto-optic Faraday effect: (a) magnetic circular birefringence (MCB) or Faraday rotation. (b) Magnetic circular dichroism (MCD). (c) Magnetic linear birefringence (MLB). (d) Magnetic linear dichroism.

3.3.2 Phenomenological origin of magneto-optic Faraday rotation

To further understand the magneto-optic Faraday effect, the first question we need to understand is how magnetic material changes the plane of polarization and intensity of light. The dielectric tensor (ε) for a crystal with cubic symmetry magnetization in the z direction can be expressed by a 3×3 matrix as following

$$\varepsilon = \begin{vmatrix} \varepsilon_{xx} & \varepsilon_{xy} & 0 \\ -\varepsilon_{xy} & \varepsilon_{xx} & 0 \\ 0 & 0 & \varepsilon_{zz} \end{vmatrix} = \varepsilon_{xx} \begin{vmatrix} 1 & -iQ & 0 \\ iQ & 1 & 0 \\ 0 & 0 & 1 \end{vmatrix} \quad 3.1$$

The optical response is defined by the local dielectric tensor, related to magneto-optic susceptibility (χ_{ij}) via

$$\boldsymbol{Q} \propto \varepsilon_0 \chi_{ij}^{(m)} \boldsymbol{H} \quad 3.2$$

Off-diagonal elements provide the direct information of magnetization due to the unique time reversal properties of magnetization, i.e., the off-diagonal element is odd in magnetization but diagonal elements are even ($\varepsilon_{xx} = \varepsilon_{yy} = \varepsilon_{zz}$, independent of magnetization).

One way to access the off-diagonal dielectric tensor elements is by invoking circularly polarized electromagnetic waves. As a light propagates along z direction, the dielectric elements of right- and left-hand circularly polarized ($\boldsymbol{n}_+$ and $\boldsymbol{n}_-$) can be related to **Q** via

$$\boldsymbol{n}_+ - \boldsymbol{n}_- \equiv \boldsymbol{n}_{+-} \propto \boldsymbol{Q} \quad 3.3$$

In other words, once we figure out the differential dielectric element between right- and left-hand circularly polarized light of magnetic materials, magnetization information can

be resolved. Actually, this is exactly the same definition of magnetic circular birefringence (MCB) or Faraday rotation which will be shown in the following section.

In general, the Faraday rotation means when a linearly polarized light passes through a magnetic material, the plane of polarization will rotate angle θ which related to the magnetic field via

$$\theta = \mathrm{V}HL \tag{3.4}$$

where the V is the Verdet constant, and L is the length of the material light passing through. A linearly polarized light with a given plane of polarization can be represented as a superposition of right- and left-hand circularly polarized waves with a given phase difference. Form a phenomenological point of view, the Faraday effect is due to the right- and left-hand circularly polarized light travels in different velocities, c/n_+ and c/n_-. To find out how θ is related to c/n_+ and c/n_-, Jonse matrix is used. By doing so, a linearly p-polarized light can be expressed as the sum of right- and left-hand circularly polarized wave:

$$\underset{\substack{\textit{linearly}\\ \textit{p-polarized}\\ \textit{light}}}{\begin{pmatrix}1\\0\end{pmatrix}} = \underset{\substack{\textit{right - hand}\\ \textit{cicularly polarized}\\ \textit{light}}}{\frac{1}{2}\begin{pmatrix}1\\-\boldsymbol{i}\end{pmatrix}} + \underset{\substack{\textit{left - hand}\\ \textit{cicularly polarized}\\ \textit{light}}}{\frac{1}{2}\begin{pmatrix}1\\\boldsymbol{i}\end{pmatrix}} \tag{3.5}$$

After passing through the magnetic material by L, the phase delay for right- and left-hand circularly polarized light will be:

$$\varphi_{\boldsymbol{R}} = \boldsymbol{k}_{\boldsymbol{R}}\boldsymbol{L} = \frac{\lambda}{2\pi}\boldsymbol{n}_{+}\boldsymbol{L} \quad \textit{Right - hand circularly polarized light}$$

$$\varphi_{\boldsymbol{L}} = \boldsymbol{k}_{\boldsymbol{L}}\boldsymbol{L} = \frac{\lambda}{2\pi}\boldsymbol{n}_{-}\boldsymbol{L} \quad \textit{Light - hand circularly polarized light} \tag{3.6}$$

where $\boldsymbol{k_R}$ and $\boldsymbol{k_L}$ are the wavevectors for right- and left-hand circularly polarized light.

The resulting light will be

$$\begin{aligned} \boldsymbol{E_{PR}} &= \frac{1}{2}\begin{pmatrix} 1 \\ -\boldsymbol{i} \end{pmatrix}\boldsymbol{e}^{\boldsymbol{i}\phi_R} + \frac{1}{2}\begin{pmatrix} 1 \\ \boldsymbol{i} \end{pmatrix}\boldsymbol{e}^{\boldsymbol{i}\phi_L} \\ &= \frac{1}{2}\begin{pmatrix} 1 \\ -\boldsymbol{i} \end{pmatrix}\boldsymbol{e}^{\boldsymbol{i}k_R L} + \frac{1}{2}\begin{pmatrix} 1 \\ \boldsymbol{i} \end{pmatrix}\boldsymbol{e}^{\boldsymbol{i}k_L L} \\ &= \frac{1}{2}\boldsymbol{e}^{\boldsymbol{i}\frac{(k_R+k_L)}{2}L}\left(\begin{pmatrix} 1 \\ -\boldsymbol{i} \end{pmatrix}\boldsymbol{e}^{\boldsymbol{i}\frac{(k_R-k_L)}{2}L} + \begin{pmatrix} 1 \\ \boldsymbol{i} \end{pmatrix}\boldsymbol{e}^{-\boldsymbol{i}\frac{(k_R-k_L)}{2}L}\right) \end{aligned} \tag{3.7}$$

Let

$$\begin{aligned} \phi &= \frac{(\boldsymbol{k_R}+\boldsymbol{k_L})}{2}\boldsymbol{L} \\ \theta &= \frac{(\boldsymbol{k_R}-\boldsymbol{k_L})}{2}\boldsymbol{L} \end{aligned} \tag{3.8}$$

The final electromagnetic wave $\boldsymbol{E_{PR}}$ will be

$$\boldsymbol{E_{PR}} = \boldsymbol{e}^{\boldsymbol{i}\phi}\begin{pmatrix} \frac{1}{2}\left(\boldsymbol{e}^{\boldsymbol{i}\theta}+\boldsymbol{e}^{-\boldsymbol{i}\theta}\right) \\ -\frac{1}{2}\left(\boldsymbol{e}^{\boldsymbol{i}\theta}-\boldsymbol{e}^{-\boldsymbol{i}\theta}\right) \end{pmatrix} = \boldsymbol{e}^{\boldsymbol{i}\phi}\begin{pmatrix} \cos\theta \\ \sin\theta \end{pmatrix} \tag{3.9}$$

which represents the rotation of linearly polarized light by an angle θ.

Applying the same approach for s-polarized light, $\boldsymbol{E_{SR}}$ will then be

$$\boldsymbol{E_{SR}} = \boldsymbol{e}^{\boldsymbol{i}\phi}\begin{pmatrix} -\sin\theta \\ \cos\theta \end{pmatrix} \tag{3.10}$$

Therefore, the rotation can be expressed by using a rotation matrix, $\boldsymbol{J_R(\theta)}$

$$\boldsymbol{J_R}(\theta) = \begin{pmatrix} \cos\theta & -\sin\theta \\ \sin\theta & \cos\theta \end{pmatrix} \tag{3.11}$$

From equation 3.6 and 3.8, the relation between angle θ and n_+ and n_- can be established

$$\theta = \frac{\pi}{\lambda}(\boldsymbol{n}_+ - \boldsymbol{n}_-)\boldsymbol{L} \qquad 3.12$$

Comparing equation 3.2, 3.3 and 3.12, a clear connection between Faraday rotation angle θ and magnetization is demonstrated.

3.3.3 Implementation of magneto-optic Faraday effects

After understanding the phenomenological origin of magneto-optic Faraday effect, now the next question will be how to extract magnetization information from instrument response? The general experimental layout of static magneto-optical Faraday rotation measurement is shown in Figure 3.9. In short, a p-polarized light is first rotated to 45° by a half waveplate, passing through the magnetic material, decomposing electric field information into horizontal and vertical components by using Wollaston prism and finally reaching the detector.

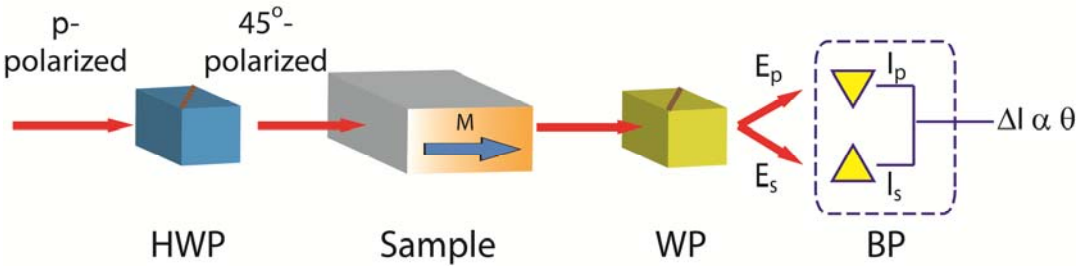

Figure 3.9. Experimental layout of static magneto-optical Faraday rotation measurements.

To see how polarization evolves, Jonse matrices were applied here as well. The Jonse matrices for half-waveplate and Wollaston prism (s/p polarization) are $\left[\frac{\boldsymbol{i}}{\sqrt{2}}\begin{pmatrix}1\\1\end{pmatrix}\right]$, $\begin{bmatrix}1\\0\end{bmatrix}/\begin{bmatrix}0\\1\end{bmatrix}$, respectively. After linearly polarized light entering the magnetic materials in 45°, leaving the sample and separating into s- and p-polarized light by Wollaston prism, the outcome electromagnetic field of s-component can be expressed as

$$\begin{aligned}\boldsymbol{E}_s &= [HWP][\boldsymbol{J}_{\boldsymbol{R}}(\theta)][Wollaston] \\ &= \left[\frac{\boldsymbol{i}}{\sqrt{2}}\begin{pmatrix}1\\1\end{pmatrix}\right]\left[\begin{pmatrix}\cos\theta & -\sin\theta\\ \sin\theta & \cos\theta\end{pmatrix}\right]\left[\begin{pmatrix}1\\0\end{pmatrix}\right] \\ &= \frac{\boldsymbol{i}}{\sqrt{2}}\begin{pmatrix}\cos\theta+\sin\theta\\ \cos\theta-\sin\theta\end{pmatrix}\begin{pmatrix}1\\0\end{pmatrix} \\ &= \frac{\boldsymbol{i}}{\sqrt{2}}(\cos\theta+\sin\theta)\end{aligned} \qquad 3.13$$

and p-component is

$$\begin{aligned}\boldsymbol{E}_p &= [HWP][\boldsymbol{J}_{\boldsymbol{R}}(\theta)][Wollaston] \\ &= \left[\frac{\boldsymbol{i}}{\sqrt{2}}\begin{pmatrix}1\\1\end{pmatrix}\right]\left[\begin{pmatrix}\cos\theta & -\sin\theta\\ \sin\theta & \cos\theta\end{pmatrix}\right]\left[\begin{pmatrix}0\\1\end{pmatrix}\right] \\ &= \frac{\boldsymbol{i}}{\sqrt{2}}\begin{pmatrix}\cos\theta+\sin\theta\\ \cos\theta-\sin\theta\end{pmatrix}\begin{pmatrix}0\\1\end{pmatrix} \\ &= \frac{\boldsymbol{i}}{\sqrt{2}}(\cos\theta-\sin\theta)\end{aligned} \qquad 3.14$$

Since the intensity is defined as the square of electric field amplitude, the signal read from the detector will be $\boldsymbol{I}_s = |\boldsymbol{E}_s|^2$ and $\boldsymbol{I}_p = |\boldsymbol{E}_p|^2$ and correlates with rotation angle via equation 3.15.

$$\begin{aligned} \boldsymbol{I}_s &= \left|\boldsymbol{E}_s\right|^2 = \frac{1}{2}\left(1+2\sin\theta\cos\theta\right) \\ \boldsymbol{I}_p &= \left|\boldsymbol{E}_p\right|^2 = \frac{1}{2}\left(1-2\sin\theta\cos\theta\right) \end{aligned} \qquad 3.15$$

Comparing the intensity difference between $\boldsymbol{I}_s$ and $\boldsymbol{I}_p$, we got

$$\begin{aligned} \frac{\Delta \boldsymbol{I}}{\boldsymbol{I}} &= \frac{\boldsymbol{I}_s - \boldsymbol{I}_p}{\boldsymbol{I}_s + \boldsymbol{I}_p} = -2\sin\theta\cos\theta \\ &= -\sin(2\theta) \\ &\cong -2\theta, \textit{when } \theta \textit{ is small} \end{aligned} \qquad 3.16$$

Therefore, by measuring the intensity difference between s- and p- components of the light, Faraday rotation angle θ, which represents the magnetization of the material, can be resolved.

3.4 Methods for Investigating Photoexcited Dynamics

The following section will focus on the techniques adapted to study the time-resolved electronic and magneto-optic response of photoexcited $Co_xFe_{3-x}O_4$ nanocrystals.

3.4.1 Transient absorption spectroscopy

Figure 3.10 schematically depicts a typical setup for pump-probe transient absorption measurement. A diode laser (Photonics DM 50-527) pumped Ti:Sapphire laser (KMlab Dragon Amplifier) produced pulses of 60 fs centered at 780 nm at 3 kHz repetition rate. The linearly polarized femtosecond laser pulses from amplified Ti:Sapphire laser are split into a strong pump pulse and a significantly weaker probe pulse by a beam splitter in a ratio of 10:1. For the pump beam either 780 nm fundamental or 390 nm doubled

beam in beta barium borate (BBO) were used to excite the material. For the probe beam, white light continuum generated by focusing 780 nm beam on a 2 mm thick sapphire crystal was used to measure the optical repose of the material. The probe beam passed through a prism dispersion compensator, which was also used to preselect the wavelength of the probe light before the sample. Preselection of the probe wavelength greatly diminished the artifact near zero time delay arising from the cross phase modulation under intense excitation. Typical pump/probe cross correlation was 70 fs and beam diameters were 150 μm and 30 μm, respectively.

The probe beam was further split into sample and reference beams by a neutral density filter before hitting the sample. The intensity of the reference beam is tuned to match the intensity of the sample beam by using a rotational neutral density filter before the measurement is started. The absorption of the material then can be obtained by comparing the intensity of sample ($\boldsymbol{I_{sam}}$) and reference ($\boldsymbol{I_{ref}}$) beams. This approach also greatly improved the signal to noise ratio by taking the effect of fluctuation of probe light intensity into account. Excited state absorption of the material was measured by comparing the absorption of the sample with and without the pump pulses excitation, (i.e., $\log\left(\frac{\boldsymbol{I}_{\boldsymbol{ref}}^{\boldsymbol{on}}}{\boldsymbol{I}_{\boldsymbol{sam}}^{\boldsymbol{on}}}\right) - \log\left(\frac{\boldsymbol{I}_{\boldsymbol{ref}}^{\boldsymbol{off}}}{\boldsymbol{I}_{\boldsymbol{sam}}^{\boldsymbol{off}}}\right)$). The optical path of the pump pulses was adjusted by using the delay stage (Newport, XPS) which enables the control of time delay between the pump and probe pulses and allow us to map out carrier dynamics of materials.

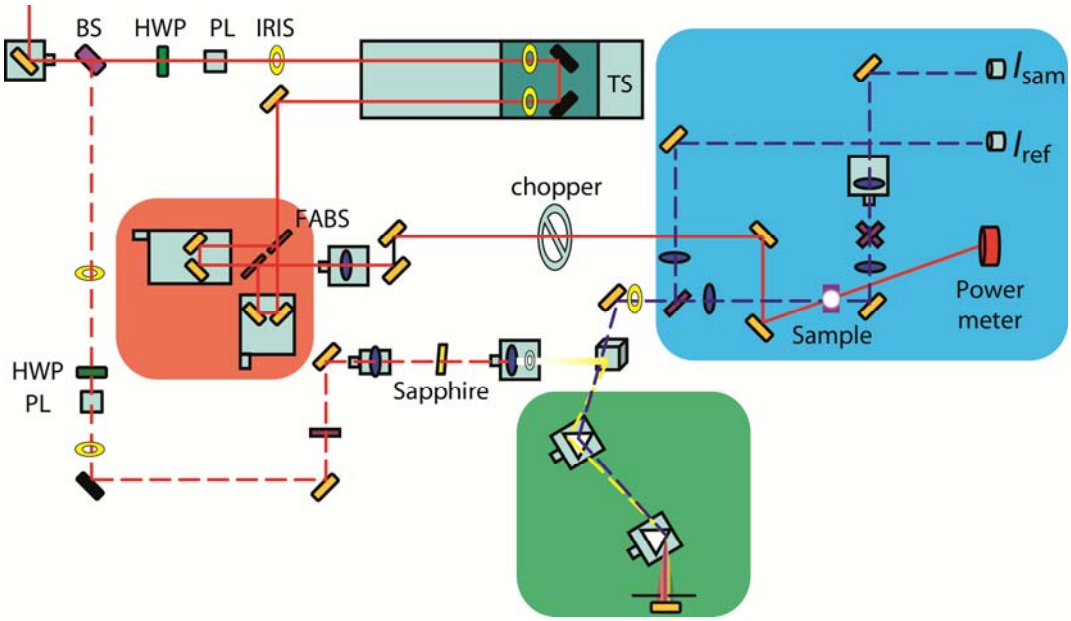

Figure 3.10. Typical setup for pump-probe transient absorption measurements. The solid red line represents the pump beam and dash line represents the probe beam. The red color area is the setup for two-pump one-probe experiment. The green area shows the preselection of probe beam wavelength by using two prism pairs. The blue area shows the pump-probe transient absorption detection setup. The abbreviations of optical components are as follow: BS: beam splitter, HWP: half waveplate, PL: polarizer, TS: translation stage, FABS: fast autocorrelator beam splitter.

In order to implement this scheme, the pump is modulated by an optical chopper (Terahertz Technology Inc C-995) with half-frequency of the laser repetition rate (~1.5 kHz). Intensities of sample and reference beams with and without the presence of pump pulses were simultaneously recorded by two boxcars (Stanford research SRS, SR250),

triggered by laser reference and synchronized with each laser shot, as a function of pump-probe time delay. As shown in Figure 3.11, after recording the raw data sets, (I_{sam}^{on}, I_{ref}^{on}, I_{sam}^{off}, and I_{ref}^{off}) at each time delay, we can derive the optical density with and without the presence of pump via $OD_{pump\ on} = -\log\left(\frac{I_{sam}^{on}}{I_{ref}^{on}}\right)$ and $OD_{pump\ off} = -\log\left(\frac{I_{sam}^{off}}{I_{ref}^{off}}\right)$. By taking the difference between $OD_{pump\ on}$ and $OD_{pump\ off}$, we can extract the transient absorption data and study the electronic dynamics of materials. With the current setup, the typical noise level of ΔOD is 4×10^{-4} with averaging 1500 pulses.

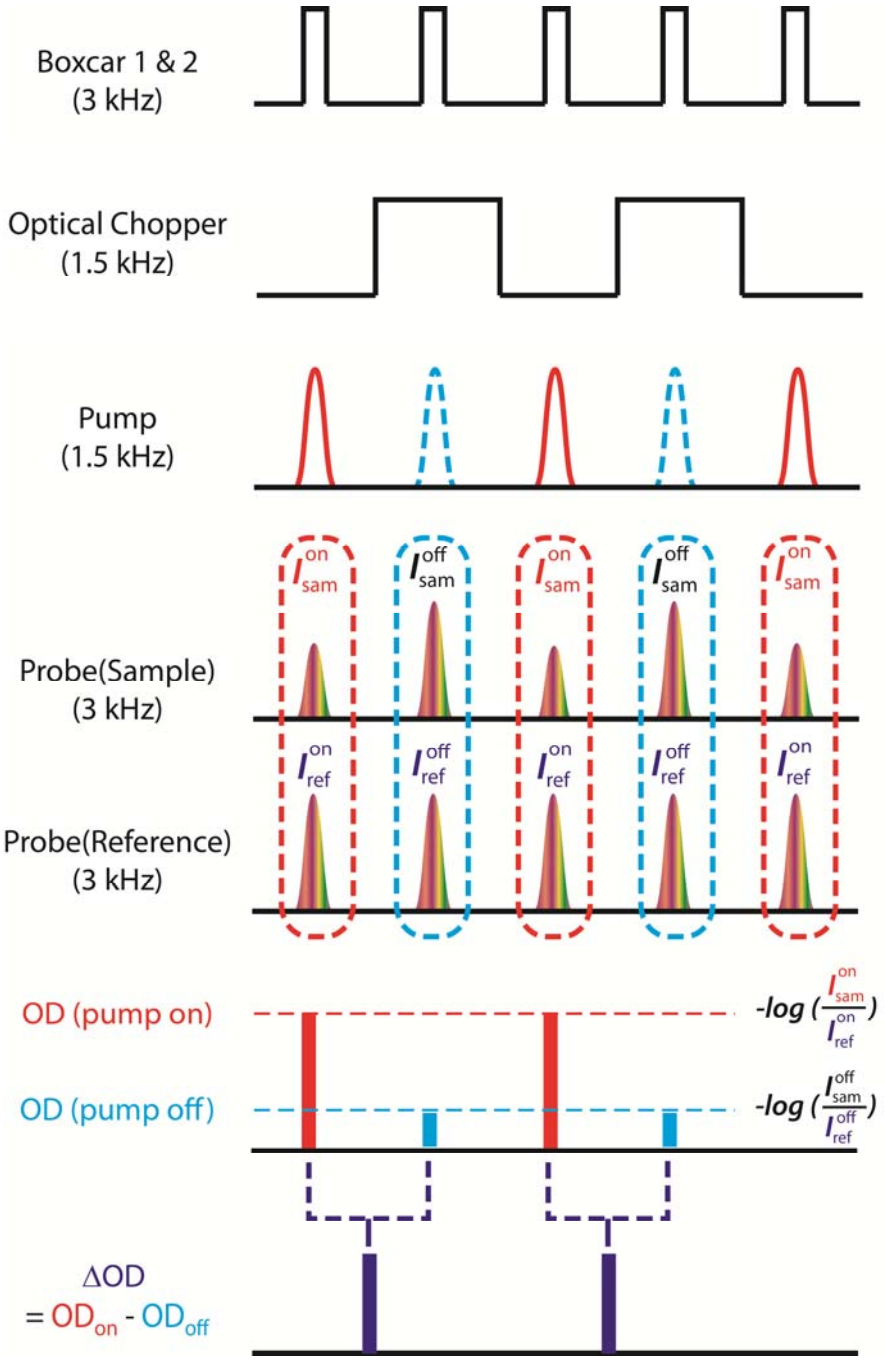

Figure 3.11. The principle of shot by shot detection of photoinduced transient absorption using two boxcar integrators.

3.4.2 Pump-probe Faraday rotation spectroscopy

Figure 3.12 schematically depicts a typical setup for pump-probe Faraday rotation measurement. The laser system is exactly the same as described in transient absorption measurement; however, to probe the magneto-optic response of materials, few changes were made and will be discussed now.

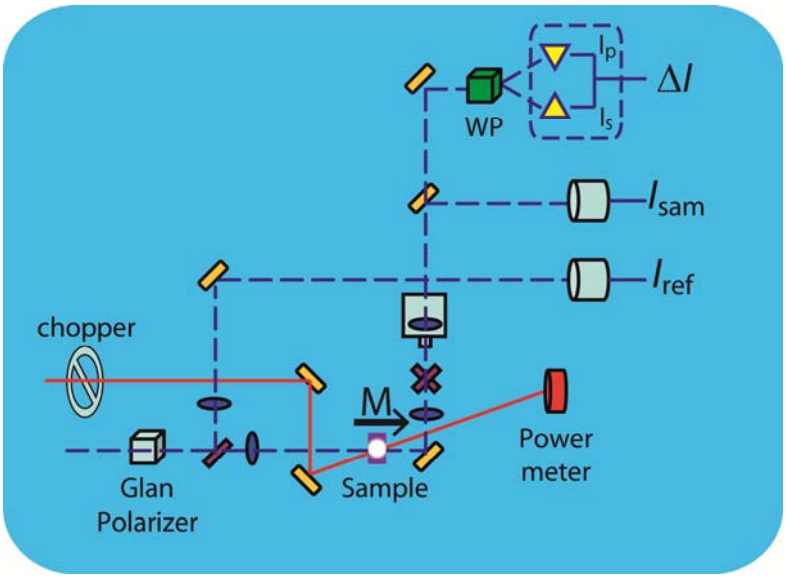

Figure 3.12. Typical detection setup for pump-probe magnetooptic Faraday rotation. The solid red line represents the pump beam and dash line represents the probe beam. A Glan polarizer was placed in front of sample to set the incident angle to be 45 respective to the Wollaston prism (WP).

A Glan linear polarizer was used to set the polarization angle of the probe light before it entered the sample. A Wollaston prism was placed after the sample, with its polarization axis set at 45° with respect to Glan polarizer. Faraday rotation was measured from the intensity difference between the two orthogonal polarization components of the probe light detected by a pair of balanced photodiodes. In this process, the probe beam was split after the sample so that time-dependent absorption of the probe light by the sample was corrected for by simultaneously measuring the total intensity of the transmitted probe light.

Schematic analysis is depicted in Figure 3.13. The external magnetic field of 0.35 T was provided by a pair of permanent magnets in the direction either parallel or antiparallel to the direction of the probe beam. As shown in Figure 3.13, after recording the raw data sets, ($\boldsymbol{I}_{\boldsymbol{BPD}}^{\boldsymbol{on}}$, $\boldsymbol{I}_{\boldsymbol{sam}}^{\boldsymbol{on}}$, $\boldsymbol{I}_{\boldsymbol{BPD}}^{\boldsymbol{off}}$, and $\boldsymbol{I}_{\boldsymbol{sam}}^{\boldsymbol{off}}$) at each time delay, we can derive the transmittances with and without the presence of pump via $T_{\text{pump on}} = \left(\frac{\boldsymbol{I}_{\boldsymbol{BPD}}^{\boldsymbol{on}}}{\boldsymbol{I}_{\boldsymbol{sam}}^{\boldsymbol{on}}} \right)$ and $OD_{\text{pump off}} = \left(\frac{\boldsymbol{I}_{\boldsymbol{BPD}}^{\boldsymbol{off}}}{\boldsymbol{I}_{\boldsymbol{sam}}^{\boldsymbol{off}}} \right)$. By taking the difference between $T_{\text{pump on}}$ and $T_{\text{pump off}}$, we can extract the transient differential magneto-optic Faraday rotation data. By further normalize with static Faraday rotation data, time-dependent fractional changes in magnetization can be obtained. With the current setup, the typical noise level of $\Delta\theta$ is 2×10^{-4} with averaging 1500 pulses.

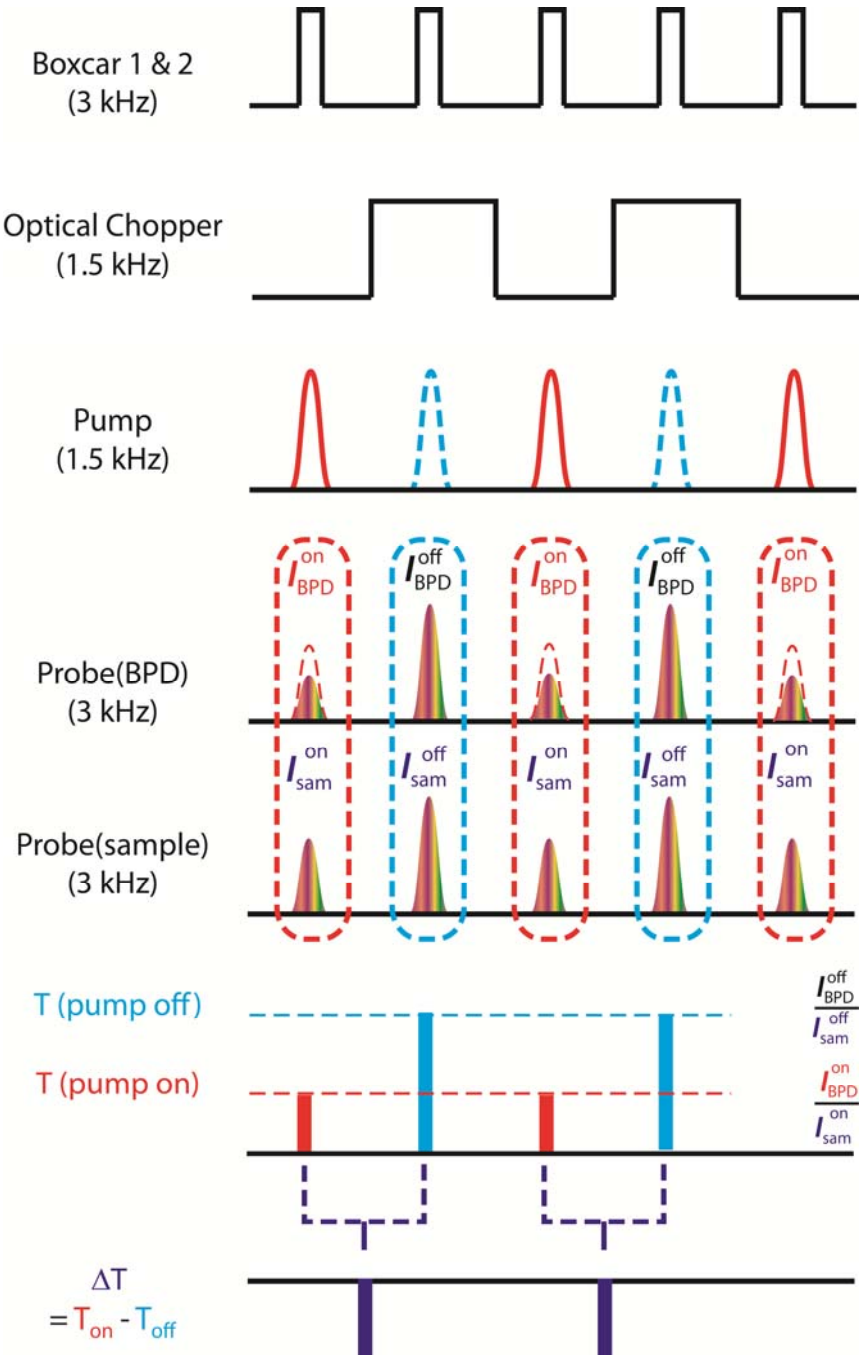

Figure 3.13. The principle of shot by shot detection of pump-probe magneto-optic Faraday rotation using two boxcar integrators.

In order to remove any potential non-magnetic contribution to Faraday rotation signal, the difference between the two data sets obtained with the magnetic fields parallel and antiparellel to the probe beam was taken to report $\Delta\theta(t)/\theta_0$.

CHAPTER IV

ELECTRONIC DYNAMICS OF PHOTOEXCITED COLLOIDAL Fe_3O_4 NANOCRYSTALS*

4.1 Introduction

Transition metal oxides exhibit interesting magnetic, electronic and optical properties, which have been utilized in a variety of applications such as magnetic resonance imaging, catalysis and solar cell.[13-16] Many of the electronic and magnetic properties of transition metal oxides are ruled by the electronic and spin states of the *d*-electrons of the transition metal ions under the influence of periodic potentials provided by mix-valence transition metal centers. The state of *d*-electrons can be varied by many means, such as direct optical excitation and modification of the ligand field via application of the pressure and temperature.[17-19] Optical excitations with ultrashort pulses, in particular, can directly access many intervalence charge transfer states and modify electronic and magnetic properties in a very fast time scale. For instance, insulator-conductor phase transition and changes in magnetism in a sub-picosecond time scale have been recently demonstrated in bulk transition metal oxides.[20-21]

---

* Reprinted in part with permission from J. Am. Chem. Soc, *129* Chen, T. –Y.; Hsia, C.-H.; Son, H. S.; Son, D. H.; "Ultrafast Energy Transfer and Strong Dynamic non-Condon Effect on Ligand Field Transition by Coherent Phonon in γ-Fe_2O_3 Nanocrystals" 10829, Copyright 2007 by the American Chemical Society.

It is important to note that an ultrashort optical excitation is often accompanied by coherent lattice motions, i.e. coherent phonons, through electron-phonon coupling in crystalline solids of various dimensionalities.[22-24] The excitation of coherent phonons can have a significant consequence on the properties of optically excited transition metal oxides, since they can directly influence the ligand field strength acting on the transition metal ions. The influence of the coherent phonon on the material properties can be more pronounced in nanocrystals than in bulk, since the energy barriers for various processes involving atomic motions in nanocrystals are typically lower than in bulk.[25-26] In addition, the time scale of the lattice motion, particularly for acoustic phonon, is dependent on the size of the nanocrystals, which provides an additional control in the dynamic modification of the material properties.[27-29] So far, the excitation of the coherent acoustic phonon and its influence on the optical properties in nanocrystals was observed only in metal and semiconductor nanocrystals. Plasmonic or excitonic transition in metal and semiconductor nanocrystals created coherent acoustic phonons via impulsive heating or displacive mechanism, inducing periodic shift of exciton resonance peak or bandgap. While a number of studies investigated the ultrafast electronic relaxation dynamics of transition metal oxide nanocrystals, observation of the coherent phonons has not been reported so far.[30-31]

In the chapter, we report the first observation of the coherent phonon and its influence on the optical properties in transition metal oxide nanocrystals created by the ultrafast excitation of intervalence charge transfer. Our interest in this study is investigating the influence of the coherent lattice motion on the optical properties of

transition metal oxide nanocrystals, particularly on the properties of ligand field transitions. In this study, we focused our discussion on two main issues: (i) the size effect on relaxation dynamics of the optically excited intervalence charge transfer transition, and (ii) the mechanism of excitation of coherent phonons. In this study, we chose Fe_3O_4 as a model system of nanocrystalline transition metal oxides, for which synthetic methods of making size-controlled and monodisperse nanocrystals are well established. An ultrafast near-infrared pump pulse prepared the intervalence charge transfer from Fe^{2+} to Fe^{3+} in the octahedral site of the unit cell. Through time-resolved absorption measurements in the visible region, no distinct size effect on relaxation dynamics of Fe_3O_4 nanocrystals was observed. On the other hand, intense particle size-dependent oscillations in the transient absorption data, due to the excitation of a coherent acoustic phonon, were observed in the entire visible region covering many ligand field transitions. Excitation of each Fe^{2+} ion in a nanocrystal was found to modulate up to 60% of its contribution to the overall absorption intensity of the nanocrystal. The large modulation of the absorption intensity has been attributed to the strongly modulated oscillator strength rather than oscillating Frank-Condon overlap. This study demonstrates that a direct optical excitation of an intervalence charge transfer can efficiently induce a coherent lattice motion, which can dynamically modify the optical properties of the transition metal oxide nanocrystals. The insight obtained here will also be a useful guide to the investigation of the possible dynamic modification of the magnetic properties in transition metal oxide nanocrystals via coherent lattice motions.

4.2 Experimental Section

4.2.1 Sample preparation and characterization

Three different sizes of spherical Fe_3O_4 nanocrystals (4.5, 7.5, and 10 nm in diameter, ~10% size dispersity) were synthesized as described in Chapter III. The resulting sample was characterized by using transmission electron microscopy (TEM), X-ray diffraction (XRD), and Raman scattering. The absorption cross section of the nanocrystals were obtained by measuring the concentration of Fe ion in the Fe_3O_4 nanocrystal samples of known size and optical density. Inductive coupled plasma atomic emission spectroscopy (ICP-AES) was used to measure the Fe ion concentration of the nanocrystal samples dissolved in hydrochloric acid (HCl). The sizes of the nanocrystals were obtained from the analysis of TEM images. The measured absorption spectra for Fe_3O_4 nanocrystals of 7.5 and 10 nm normalized to iron concentration = 30 ppm were shown in Figure 4.1.

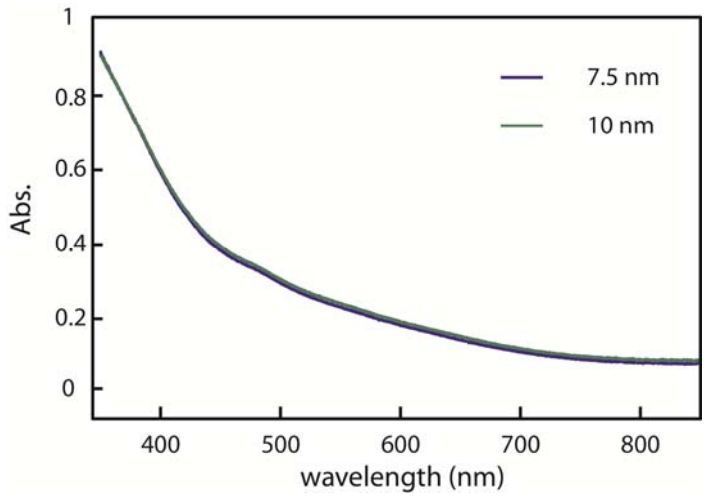

Figure 4.1. UV-Vis spectra of 7.5 and 10 nm Fe_3O_4 nanocrystals with [Fe] = 30 ppm.

4.2.2 Pump-probe transient absorption measurements

The pump-probe transient absorption measurement was made as described in Chapter III. The optical density at the pump wavelength was kept around 0.1 to minimize the variation of the pump intensity within the sample. The average pump fluence under the probe pulse area was varied between 15 and 61 mJ/cm^2 for studying pump fluence dependence, while most of the data reported here were obtained at the fluence of 80 mJ/cm^2.

Fe_3O_4 nanocrystal samples were dispersed in cyclohexane and continuously circulated through a jet nozzle to produce a free streaming jet to ensure excitation of the fresh sample area for each pump pulse. The thickness of the sample jet was 400 μm. In metallic nanocrystals, intense excitations could induce thermal lensing or the formation of bubbles due to the very rapid electronic relaxation that heated the lattice and the surrounding solvent molecules.[32-33] However, combined with much slower electronic relaxation (~ hundreds of ps) compared to the metal nanocrystals (several ps), the flowing jet was effective in preventing the problems arising from the rapid local solvent heating. X-ray diffraction data of the sample taken before and after a long period of measurements (typically 10 hours) showed no indication of phase transition by continued exposure to the pump pulse.

4.3 Electronic Structures of Inverse Spinel Fe_3O_4 Nanocrystals

Magnetite, Fe_3O_4, is the oldest magnetic material people have studied so far. However, due to its complicated magnetic structure (containing three inequivalent iron

atoms), temperature dependent conductivity (Verwey transition), and entangled indirect exchange interaction (superexchange and double exchange), studies of electronic and magnetic structure, and optical or magnetic response of magnetite is still of fundamental importance and attracts a lot of attention.

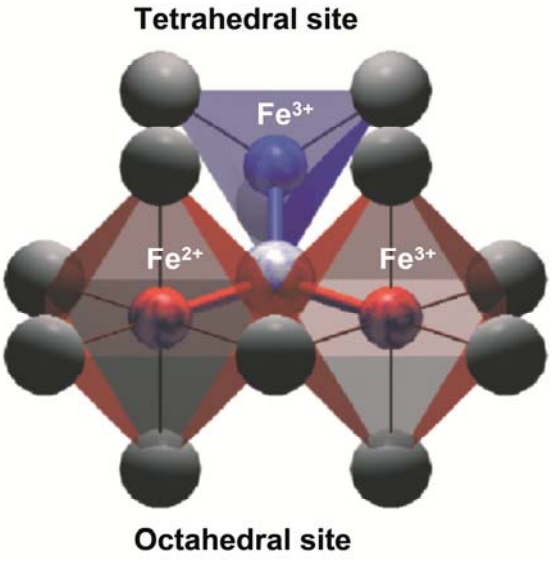

Figure 4.2. Crystallographic structure of magnetite, one Fe^{3+} occupied tetrahedral site (A site) and one Fe^{2+} and one Fe^{3+} occupied the octahedral site (B Site), Figure adapted from Stöhr's book.[4]

The key features of the crystallographic and magnetic structure of magnetite are shown in Figure 4.2. The crystal structure is called inverse spinel structure where the oxygen ions composed a face center cubic packed structure and the Fe atoms occupied either the octahedral or tetrahedral sites. Specifically, the tetrahedral site is occupied by a

Fe^{3+} ion and the octahedral site occupied by one Fe^{3+} and one Fe^{2+} ions. The molecular formula can be written as $(Fe^{3+})_A[Fe^{3+}\ Fe^{2+}]_BO_4$, where A and B represent the tetrahedral and octahedral sites, respectively. The magnetic moment on a given Fe atom is coupled antiferromagnetically via superexchange to another Fe atom of the same valency, and ferromagnetically via double exchange to a Fe atom of different valency.

The local electronic structure of each iron atom is determined by the geometry of oxygen atoms surrounding it. For example, the degenerated *d* electrons of Fe^{3+} in the octahedral site were left to t_{2g} and e_g. In Fe_3O_4, the real electronic structure became more complicated due to the fact that the *d* electron in three different Fe atoms will interact with each other. Because of that, such mixed valence iron oxides often exhibit electron hopping between adjacent Fe^{2+} and Fe^{3+} cations and optically induced charge transfer transitions. Fortunately, many studies of static electronic and magneto-optic calculation of Fe_3O_4 have been carried out by many research groups. Figure 4.3 shows the simplified band structure of bulk Fe_3O_4. Comparing with the UV-Vis-NIR absorption spectrum of Fe_3O_4, (Figure 4.1), it is clear that in the visible to near infrared region, the absorption is mainly from intervalence charge transfer transitions ($Fe^{2+} \rightarrow Fe^{3+}$). For the UV region, on the other hand, the absorption is from the mixture of intervalence charge transfer ($Fe^{2+} \rightarrow Fe^{3+}$) and intersublattice charge transfer transitions ($Fe^{3+} \rightarrow Fe^{3+}$).

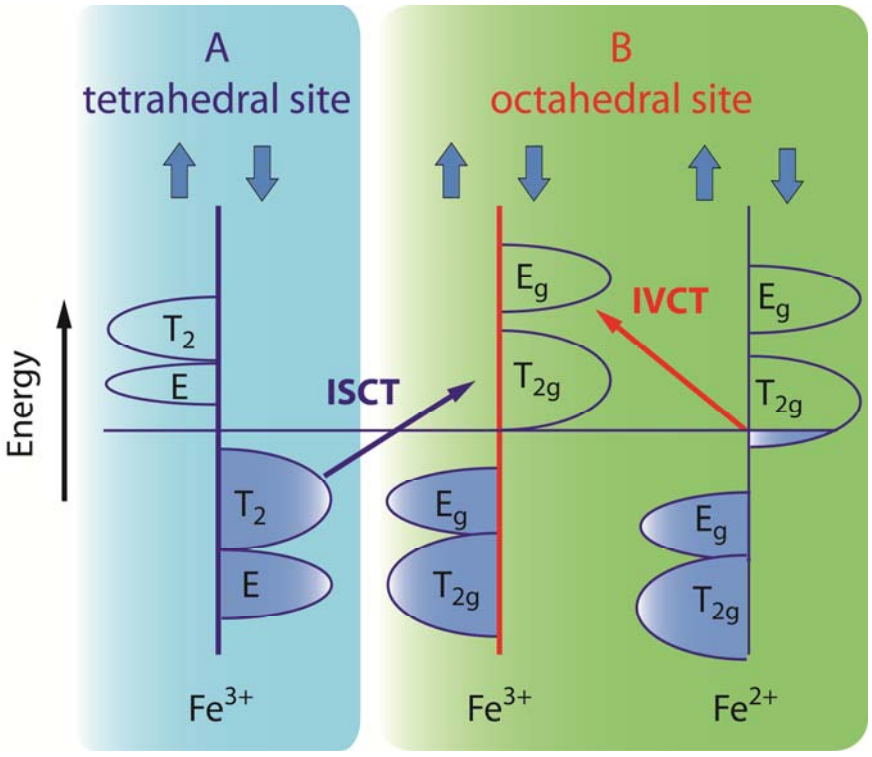

Figure 4.3. Simplified band structure of bulk Fe_3O_4, ISCT and IVCT represent inter sublattice charge transfer and intervalence charge transfer, respectively.

4.4 Electronic Dynamics of Photoexcited Colloidal Fe_3O_4 Nanocrystals

4.4.1 Dynamic features in transient absorption data

Figure 4.4 shows the transient absorption data of spherical (7 nm diameter) Fe_3O_4 nanocrystals, pumped at 780 nm and probed at various visible wavelengths. In Figure 4.4, the data exhibit dynamics occurring on multiple time scales. In addition, intense oscillatory features from coherent phonons are superimposed on the decaying induced absorption at all probe wavelengths. The transient absorption data were well fit to a sum of exponential functions and an exponentially decaying cosine function. From this fit,

the oscillatory and non-oscillatory features of the transient absorption data were separated to reveal the underlying dynamics more clearly as shown in Figure 4.5.

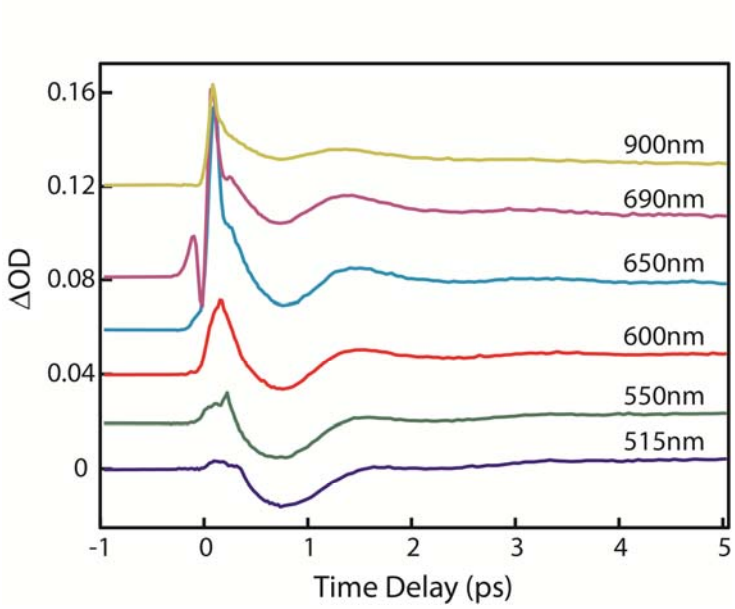

Figure 4.4. Transient absorption data of 7.5 nm Fe_3O_4 nanocrystals pumped at 780 nm and probed at various wavelengths indicated above each data.

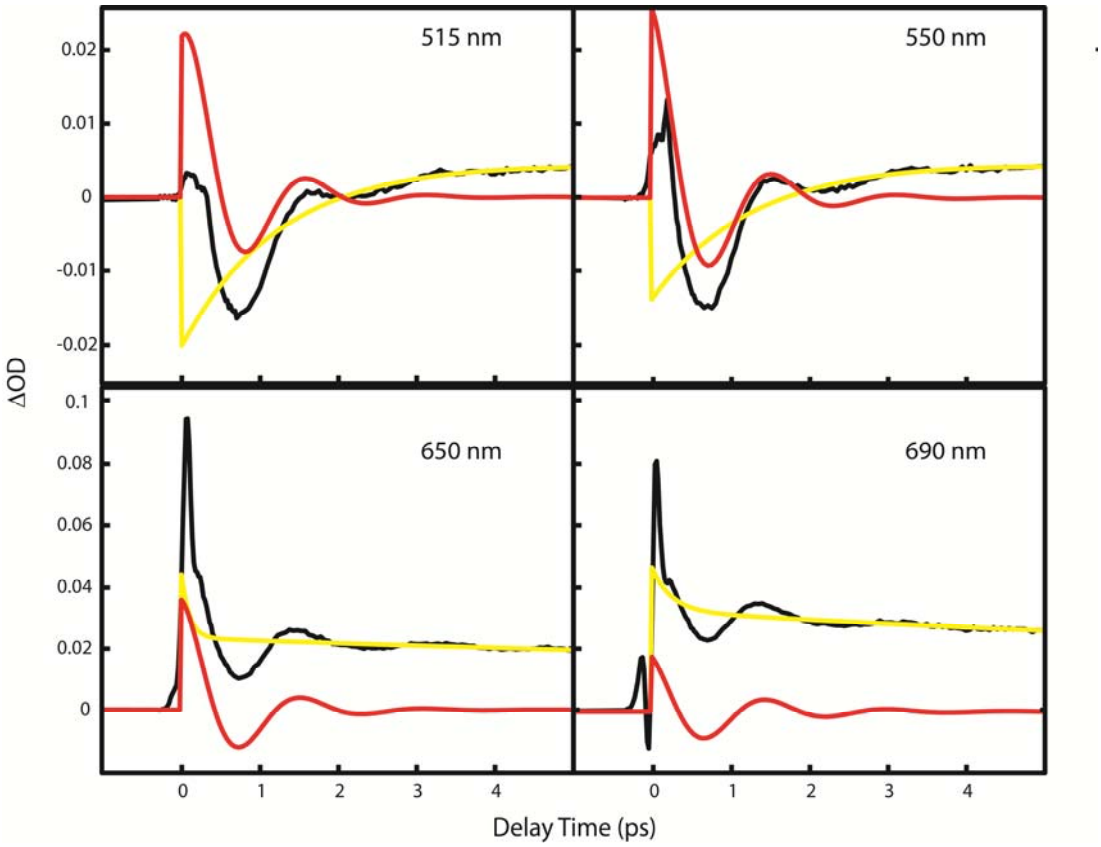

Figure 4.5. Transient absorption data of 7.5 nm Fe_3O_4 nanocrystals. Oscillatory and nonoscillatory parts are separated to reveal the dynamics more clearly. Note different y-scale for upper and lower panels. Probe wavelength is indicated in each panel. Original transient absorption data (black), $\boldsymbol{A}\cdot\cos(2\pi t/\tau+\phi)$ function to fit the oscillatory part (red), oscillation subtracted data (yellow).

Longer time scale dynamics at the 650 nm probe wavelength is also shown in Figure 4.6. The main features in the dynamics are: i) an immediate rise and decay of the pump-induced absorption in 100 fs, ii) a build-up of the induced absorption in 1 ps at shorter

probe wavelengths (e.g. 515, 550 nm), iii) a decay of the induced absorption on tens and hundreds of ps, and vi) prominent oscillations with a size-dependent period.

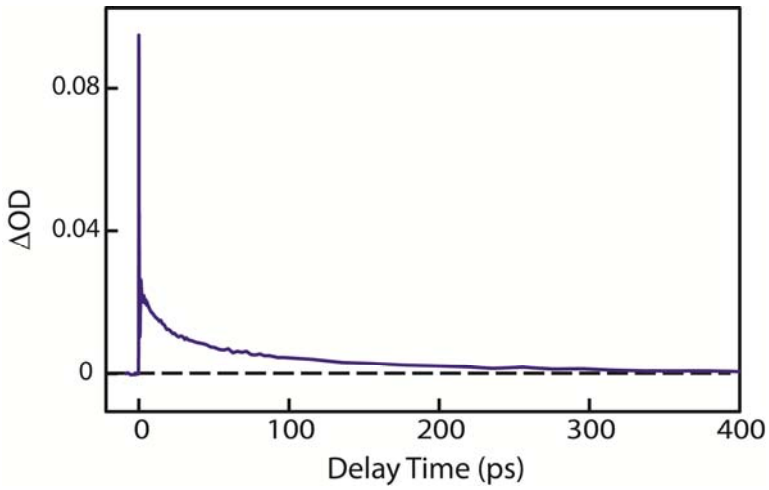

Figure 4.6. Long-time window transient absorption data of 7.5 nm Fe_3O_4 nanocrystals obtained with 780 nm pump and 650 nm probe.

From the absorption cross section of Fe_3O_4 nanocrystals at the pump wavelength measured in a separate experiment ($\sigma = 6.9 \times 10^{-15} cm^2$ for 7.5 nm nanocrystal), it was estimated that about 10 % of the Fe^{3+} ions in each nanocrystal were excited at the pump fluence of 45 mJ/cm^2. With this estimation and the oscillation-subtracted transient absorption traces, absorption spectra of the excited state at several time delays were constructed using the following equation:

$$\Delta OD(t,\lambda) = x(t)\cdot[OD_e(t,\lambda) - OD_g(\lambda)] \qquad 4.1$$

where $\Delta OD(t,\lambda)$ is the oscillation-subtracted transient absorption signal at time t, $x(t)$ is the average fraction of the excited Fe^{2+} ions in each nanocrystal, $OD_e(t,\lambda)$ and $OD_g(\lambda)$ are the excited and ground state absorptions of the nanocrystals, respectively. In equation 4.1, we assumed that the absorption cross section of each nanocrystal for the charge transfer transitions can be roughly represented as a sum of contributions from all local absorbing Fe^{2+} ions.

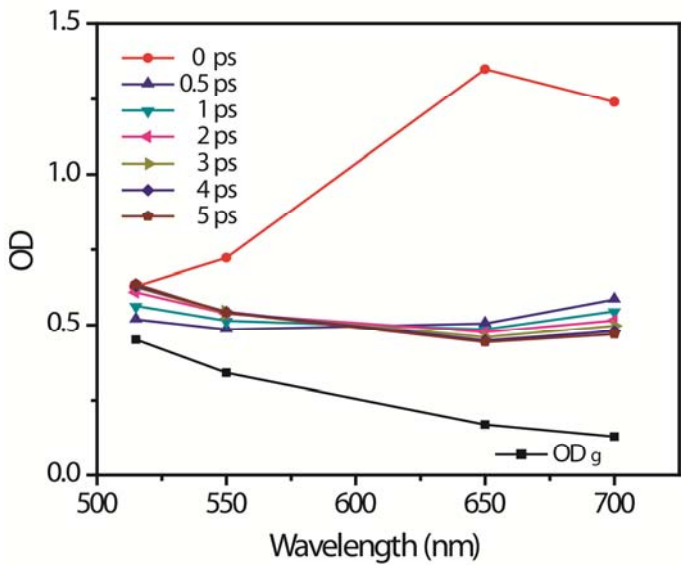

Figure 4.7. Ground-state absorption (OD_g) and excited-state absorption (OD_e) spectra constructed by using equation 4.1 at different delay times.

In Figure 4.7, the calculated $OD_e(t,\lambda)$ are plotted together with $OD_g(\lambda)$. The excited state absorption, right after the excitation, is significantly more intense than the ground state absorption, particularly in the longer probe wavelength region. After the initial fast

decay, the excited state absorption decreases and shows a flatter spectrum. The excited states have more intense absorption than the ground states because all the ligand field states except the ground state have the same spin multiplicity, which lifts the restriction imposed by the spin selection rule.

As far as dynamic features are concerned, in Figure 4.5, the immediate rise and fast decay (~100fs) of the induced absorption are observed in the entire range of the probe wavelength covered in this study. This indicates that part of the initially excited-states relaxes immediately after the excitation. A closer look at the oscillation subtracted transient absorption data (Figure 4.5) reveals that the induced absorption rises on a 1 ps time scale at 515 and 550 nm probe wavelengths, while it continues to decrease at the longer wavelengths. The apparent blue-shift of the excited state absorption on a 1 ps time scale can be attributed to the relaxation within the vibronic manifold. A similar assignment has been made earlier by Juban et al. in a transition metal complex with an octahedral coordinated Cr^{3+} center.[34] In their study, the dynamics occurring on 1.1 ps time scale were attributed to the relaxation in the vibronic manifold of the ligand field state following the ultrafast intersystem crossing from a charge transfer to a ligand field state.

4.4.2 Size effect on transient absorption

The transient absorption measurements were also performed with 4.5 and 10 nm Fe_3O_4 nanocrystals with 780nm pump and 620 nm probe. The size dependent transient absorption data were shown in Figure 4.8. Time scales extracted from the fitting of three

different sizes did not show strong size dependence. This may not be surprising since the carrier created via intervalence charge transfer in Fe_3O_4 nanocrystals is not really delocalized through the whole volume but is iterating between two metal ions.

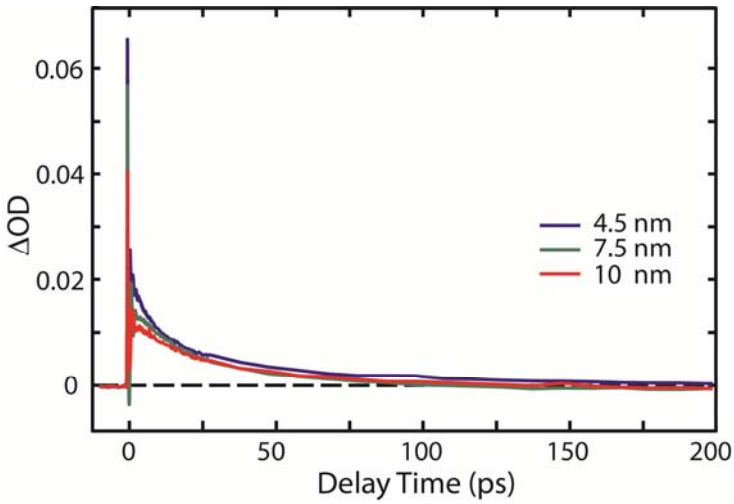

Figure 4.8. Size dependent ΔOD data of Fe_3O_4 nanocrystals at the excitation fluence 46 mJ/cm^2.

4.5 Photoinduced Coherent Acoustic Phonon

4.5.1 Creation of coherent phonon from intervalence charge transfer transition

The oscillatory features in the transient absorption data indicate creation of coherent phonons by the optical excitation. Coherent phonons are usually excited by either displacive or impulsive mechanisms depending on the electronic structure of the sample and the properties of the excitation pulse.[35-36] For Fe_3O_4 nanocrystals excited at 780 nm, the coherent phonon is likely to be created through the displacement of the equilibrium

lattice geometry upon $Fe^{2+}(O_h)$ to $Fe^{3+}(O_h)$ intervalence charge transfer excitation rather than the impulsive stimulated Raman scattering considering the cosine phase of the oscillation.

The origin of the displacement of the equilibrium geometry from intervalence charge transfer transition is the change of the electronic configuration in *d*-orbitals that shifts one electron from Fe^{2+} to Fe^{3+} in the octahedral site which results in the decrease in the metal-ligand equilibrium distance. Although the contraction of the lattice in the excited state of Fe_3O_4 has not been experimentally observed yet, recently developed tools such as time-resolved X-ray absorption or diffraction will be particularly suitable for making such a measurement.[22,37]

The period (τ) of the oscillation was dependent on the radius (r) of the nanocrystals, where τ = 0.87 and 1.55 ps for r = 2.2 and 3.7 nm respectively. The phonon mode responsible for the oscillation of the absorption intensity is most likely the lowest-order radially symmetric mode of the confined acoustic phonon.[27] The size dependence of the coherent acoustic phonon in nanocrystals has been usually explained by Lamb's theory of the confined acoustic mode in the spherical elastic particles.[38] For the lowest-order radial breathing mode, the period (τ) of the acoustic phonon can be calculated from equation 4.2, which predicts a linear relationship between the radius (r) of the particle and the period (τ) of the phonon.

$$\tau = \frac{2\pi r}{\eta c_L}, \quad \eta \cot(\eta) = 1 - \left(\frac{\eta c_L}{2c_T}\right)^2 \qquad 4.2$$

c_L and c_T are the longitudinal and transverse speeds of sound, respectively, which are related to the Young's moduli (C_{11} and C_{44}) and the density (ρ) through $c_L = \sqrt{C_{11}/\rho}$, $c_T = \sqrt{C_{44}/\rho}$. Because of the lack of information on the Young's moduli of Fe_3O_4, we could not compare the measured periods with the predictions from Lamb's theory. However, the period of the oscillation was within the typical range that would be expected for the materials of similar structure.[39] While Lamb's theory predicts a linear relationship between the vibrational period and the size of the particle, the experimental result deviates from this prediction. This is probably due to the variation of the Young's moduli of Fe_3O_4 with the size in nanometer range, where the fraction of the surface atoms is a strong function of the size. Indirect evidence for the size-dependent Young's moduli can be obtained from the size-dependent bulk modulus.[40] The bulk modulus of Fe_3O_4 nanocrystals measured under the hydrostatic pressure increased with the radius of the nanocrystal, which suggests a similar size-dependence of the Young's moduli. According to this assumption, the Young's moduli of 7.5 nm nanocrystals are about 15 % larger than 4.5 nm nanocrystals. This can partly explain the sub-linear relationship between the radius and the oscillation period observed in this study.

4.5.2 Strong modulation of oscillator strength by coherent phonon

The oscillation in the transient absorption data, whose amplitudes are as large as ΔOD, indicates the strong vibronic coupling nature of charge transfer transition. However, it seems unusually intense for the transitions exhibiting rather broad and featureless absorption spectra in both the ground and excited states.

For more quantitative analysis of the oscillation amplitude, we calculated the relative amplitude of the oscillation with respect to the total absorption intensity (*OD*) at a given time delay. $OD(t,\lambda)$ was calculated simply from the following equation:

$$OD(t,\lambda) = \Delta OD(t,\lambda) + OD_g(\lambda) \qquad 4.3$$

where ΔOD and OD_g are defined in the same way as in equation 4.1. As discussed in the previous section, we estimated that about 10 % of the total Fe^{2+} ions in each nanocrystal were excited initially based on the measured absorption cross section and the pump fluence. Under this condition, the modulation of the absorption was 1-6 % of the total absorption (OD) depending on the probe wavelength.[41] The modulation depth also increased linearly to the pump fluence within the fluence range of 15-61 mJ/cm^2 as shown in Figure 4.9. This indicates that the excitation of each Fe^{2+} ion modulates 10-60 % of its contribution to the total absorption intensity of the nanocrystal within the pump fluence range of our study.

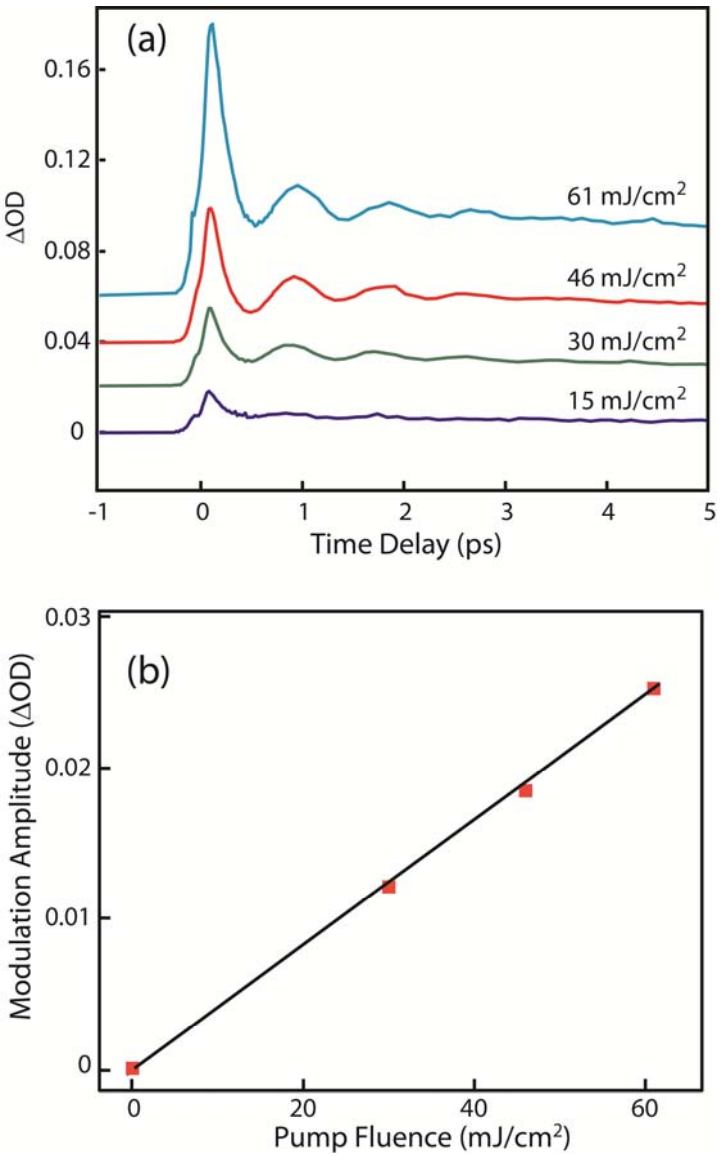

Figure 4.9. (a) Pump fluence dependence of the transient absorption data with 780 nm pump and 620 nm probe for 4.5 nm Fe_3O_4 nanocrystals. (b) Pump fluence dependence of the oscillation amplitude.

Another notable feature is the wavelength dependence of the modulation depth. Typically, coherent phonons or vibrational wavepackets in crystalline solids and molecules shift only the bandgap or the peak of the absorption spectrum periodically without changing the oscillator strength. In this case, the relative amplitude and phase of the oscillations at different probe wavelengths reflect the slope of the absorption spectrum.[36] For Fe_3O_4 nanocrystals, the observed modulation depth is too large to be explained simply by the periodic shift of the relatively flat ground and excited absorption spectra, particularly at the longer wavelength region. Furthermore, the oscillation amplitude increases with the probe wavelength, while the slope of the absorption spectra decreases with the wavelength or show a flat shape as shown in Figure 4.7. This suggests that the oscillations in the transient absorption are primarily due to the modulation of the oscillator strength rather than the oscillating Frank-Condon overlap.

Finally, it is noteworthy to compare the influence of coherent phonons on transition metal oxide nanocrystals with those on metal and semiconductor nanocrystals. For many metal and semiconductor nanocrystals, relatively simple changes in the energy band structure can usually explain the effect of coherent phonons on the optical properties via periodic shift of the plasmon resonance or bandgap.[24,28] On the other hand, the effect can be more pronounced and complex in transition metal oxide nanocrystals. Multiple factors, such as the metal-ligand orbital overlap, magnetic interaction between the metal ions, and asymmetry of the ligand field can affect the properties of interavlence charge transfer with a varying sensitivity. Additionally, coherent phonons may also influence the magnetic properties of the transition metal oxide nanocrystals. Since the magnetic

moment has it origin also on the unpaired *d*-electrons, periodic modulation of the metal-ligand distance may redistribute the spin density, thereby changing the magnetic moment on the metal ions.[42-43]

4.6 Summary

Relaxation dynamics of an optically excited intervalence charge transfer state and the effect of the coherent phonon on the intensities of intervalence charge transfer in Fe_3O_4 nanocrystals were investigated. We were interested in studying the dynamics of the optical transitions in Fe_3O_4 nanocrystals, particularly following the excitation of the charge transfer, due to the capability of directly modifying the electronic and/or spin states of *d*-electrons. The excited charge transfer state exhibited an ultrafast (100 fs) back energy transfer to the neighboring octahedral Fe^{2+} ions, and subsequently went through the vibrational and electronic relaxation. Size effect on electronic dynamics of Fe_3O_4 nanocrystals is not distinct. Furthermore, the charge transfer excitation created coherent acoustic phonon, resulting in strong oscillations in the transient absorption data. The strong oscillation of the absorption has been explained in terms of the modulated oscillator strength of the charge transfer transitions. The present observation demonstrates that the charge transfer excitation can create coherent phonons in the transition metal oxide nanocrystals, which can dynamically modify their material properties.

CHAPTER V

TRANSIENT LATTICE TEMPERATURE OF PHOTOEXCITED COLLOIDAL Fe_3O_4 NANOCRYSTALS*

5.1 Introduction

Nanoscale magnetic materials have been attracting much attention in recent years due to the wide range of technological applications ranging from biomedical imaging to magnetic data storage devices.[13,44-46] Chemically synthesized colloidal magnetic nanocrystals are serving as a particularly useful material platform in many studies for a variety of reasons. Easy control of the size, morphology and stoichiometry and facile chemical functionalization enabled systematic studies of the magnetic properties in nanometer length scale in diverse chemical environments.[10,47-49] Recently, optically induced dynamic magnetization in magnetic nanocrystals is gaining interest due to the potential applications in high-density and high-speed magnetic data storage devices.[50-51] Optical manipulation of magnetization using femtosecond laser pulses on bulk surfaces has been extensively investigated in the last decade. Various mechanisms of thermal and non-thermal optical control of the magnetization were proposed from these earlier studies.[20,52-54]

---

* Reprinted in part with permission from J. Phys. Chem. C, *112* Chen, T. –Y.; Hsia, C.-H.; Son, D. H.; "Time-Dependent Elastic Property and lattice Temperature of the Photoexcited Iron Oxide Nanocrystals" 10125, Copyright 2008 by the American Chemical Society.

The coupled nature of the magnetization dynamics to the dynamics in electronic and lattice degrees of freedom has also been investigated in these studies. For instance, optically induced demagnetization in ferromagnetic metals has often been explained phenomenologically using the three-temperature model.[5] This model described the time evolution of the magnetization in terms of the equilibration of the electronic, lattice and spin temperatures. Modulation of the magnetization by coherent phonon on sub-picosecond time scale was also observed, which demonstrated the presence of the ultrafast coupling pathway between the spin and lattice degrees of freedom.[55]

The fundamental mechanisms of optical manipulation of the magnetization and the nature of the coupling among the electronic, lattice and spin degrees of freedom should be the same regardless of the dimension of the magnetic materials. However, the dynamic magnetization in nanocrystals can exhibit a dependence on the size unlike in bulk phase. In principle, variation of the size of magnetic nanocrystals can influence the dynamics in spin degrees of freedom directly or indirectly through the coupling of the spin to the electronic and lattice degrees of freedom. For instance, size-dependent magnetization dynamics in iron oxide nanocrystals discussed in our earlier work proposed the size-dependent spin correlation as its origin.[56] On the other hand, size-dependence of the lattice temperature due to different lattice cooling rate may also result in the size-dependent magnetization, especially when the thermal excitation of spins becomes important. Therefore, it will be important to obtain an understanding on the energy dissipation in electronic and lattice degree of freedom to obtain an accurate picture of the dynamic magnetization in photoexcited magnetic nanocrystals.

In this chapter, we investigated the elastic property and the lattice temperature of the photoexcited iron oxide (Fe_3O_4) nanocrystals as the prototypical magnetic ferrite nanocrystals. Information on the elastic properties and lattice temperature was obtained by measuring the period of coherent acoustic phonon as a function of excitation fluence and delay time after the excitation. The period of the radial breathing mode of coherent acoustic phonon in spherical nanocrystals is determined by sound velocity and the radius of the nanocrystal according to a simple model based on Lamb's theory.[38] Therefore, information on the elastic property can be obtained from the measurement of the period of coherent acoustic phonon. A rough estimation of the lattice temperature after the excitation was made from the knowledge of temperature-dependent sound velocity in a closely related ferrite material. Time-dependent period of coherent acoustic phonon was also measured by employing two-pump/probe measurement, where the first pump pulse acted as a heating pulse and the weaker second pump pulse created coherent phonon at various delay times. From this measurement, time-dependent lattice temperature of the photoexcited Fe_3O_4 nanocrystals was estimated.

5.2 Experimental Section

5.2.1 Sample preparation

Colloidal iron oxide nanocrystals (Fe_3O_4) were synthesized and characterized as described in Chapter III. 4.8 and 8.4 nm Fe_3O_4 nanocrystals were used for the measurement specifically. According to the analysis of Vis-NIR absorption spectra of the sample, the final samples used in the experiment were more oxidized than the Fe_3O_4

nanocrystals initially synthesized. The nanocrystal samples used in all the measurements were dispersed in cyclohexane. The sample solutions were continuously circulated through a flat nozzle to create a 400 μm-thick jet of the sample solutions. The free streaming jet of samples with linear flow speed of 2-3 meters/sec was used to prevent potential sample damage from repeated exposure of the sample on the same sample region. The concentrations of the nanocrystal samples were adjusted such that total Fe ion concentration was kept approximately at 1.8 mM.

5.2.2 Two pulse transient absorption measurement

Pump-probe transient absorption traces of the nanocrystal samples were recorded as described in Chapter III. For the pump fluence dependence experiment, the pump fluence was varied up to 290 mJ/cm^2. For two-pump/probe experiment, the intensity ratio of the two pump beams was set to 90:10 using a beam splitter. The stronger pump is used as heating pulses and the weaker one use to estimate the lattice temperature at a given time. Time delay between heating and second pump pulse was controlled by manually controlling the translation stage.

5.3 Lattice Temperature Estimated from Phonon Frequency

Figure 5.1 shows the pump/probe transient absorption (ΔOD) data of colloidal Fe_3O_4 nanocrystal samples (4.8 nm in diameter) at various pump fluences obtained with 780 nm pump and 550 nm probe light. With increasing excitation fluence, the amplitudes of both the oscillatory and non-oscillatory components increased. The oscillatory

component is due to coherent acoustic phonon, which has been observed in many nanocrystalline materials including semiconductor and metal nanocrystals.[57-58] In the case of Fe_3O_4 nanocrystals excited at 780 nm, coherent phonon is probably generated by the displacive mechanism from intervalence charge transfer transition between Fe^{2+} and Fe^{3+} ions as discussed in the previous chapter.

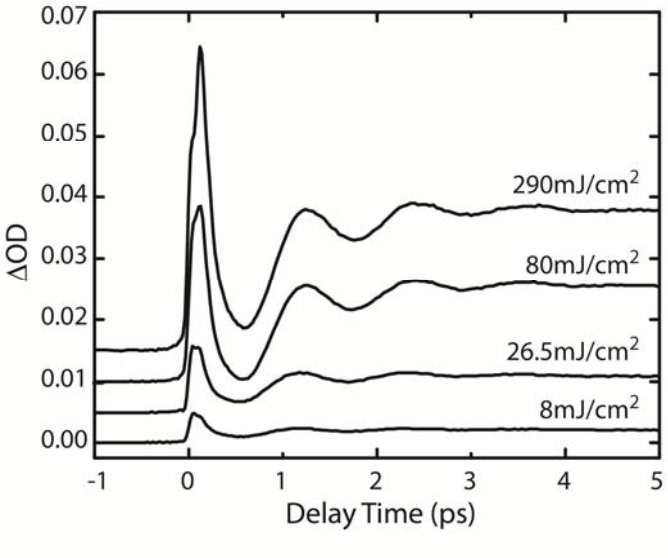

Figure 5.1. Pump-probe transient absorption data of colloidal Fe_3O_4 nanocrystals obtained with 780 nm pump and 550 nm probe at various excitation fluences.

Nanocrystal samples of two different sizes (4.8 and 8.3 nm in diameter) were used for the measurement of the excitation fluence-dependent period and amplitude of coherent acoustic phonon. For both samples, concentration of the total Fe ions in nanocrystal solution was maintained approximately the same. Based on the measurement of the pump beam absorption by the sample solution, the average excitation density per

nanocrystal was also similar in both samples. In order to obtain the amplitude (a_o) and period (τ) of the oscillation due to coherent phonon, the transient absorption data (ΔOD) were fit to the sum of multi-exponential functions and an exponentially decaying cosine function as shown in equation 5.1.

$$\Delta OD(t) = \Sigma a_i \cdot exp(t/\tau_i) + a_o \cdot cos(2\pi t/\tau + \phi) \cdot exp(-t/\tau_o) \qquad 5.1$$

The extracted period and amplitude of the oscillation as a function of the excitation fluence for two nanocrystal samples are shown in Figure 5.2(a)-(c). The period (τ) is shorter for smaller nanocrystal as predicted from a model based on Lamb's theory.[38] In spherical nanocrystals, the period of coherent acoustic phonon corresponding to the radial breathing mode is related to the radius (r) and sound velocity of the nanocrystal as shown in equation 5.2.

$$\tau = \frac{2\pi r}{\eta c_L}, \quad \eta \cot(\eta) = 1 - \left(\frac{\eta c_L}{2 c_T}\right)^2 \qquad 5.2$$

c_L and c_T are longitudinal and transverse velocity of sound respectively, which are related to Young's modulus (C_{11} and C_{44}) and density (ρ) through $c_L = \sqrt{C_{11}/\rho}$, $c_T = \sqrt{C_{44}/\rho}$.

With the increasing excitation fluence, the period of coherent phonon increased as shown in Figure 5.2(a) and (b). This is most likely due to the heating of the lattice by photoexcitation resulting in the softening of the lattice. A similar fluence dependence of the coherent phonon period was observed previously in metallic nanocrystals, where the decrease of the coherent phonon period was attributed to the lattice heating.[59] Nonthermal softening of the lattice is not likely to play a significant role, since the effect

of the excitation on the period of coherent acoustic phonon persists much longer (>100 ps) than would be expected from a purely electronic origin.[60] More detailed discussion on time dependence of coherent phonon will be made in the following section. The amplitude of oscillation also increases with increasing excitation fluence as shown in Figure 5.2(c). The amplitude of oscillation increases linearly to the excitation fluence up to 100 mJ/cm^2 and saturated at higher fluences. A similar increase of the amplitude with the excitation fluence was observed in semiconductor nanocrystals as well.[29] The increase of the oscillation amplitude with the excitation fluence can be interpreted as the increasing magnitude of lattice displacement, although there is not a simple and quantitative relationship between the oscillation amplitude of ΔOD and lattice displacement.

The fractional change of the period at fluence F with respect to the period extrapolated to zero fluence, $[\tau(F)-\tau(0)]/\tau(0)$, is indicated on the right y-axes of Figure 5.2(a) and (b). Both samples exhibit a very similar fluence dependence of the fractional change of period, indicating that the effect of excitation on the elastic constants is comparable in both samples. This may not be surprising since approximately the same excitation densities in both samples will result in the lattice heating to a comparable level if the cooling of the lattice at early delay time is ignored.

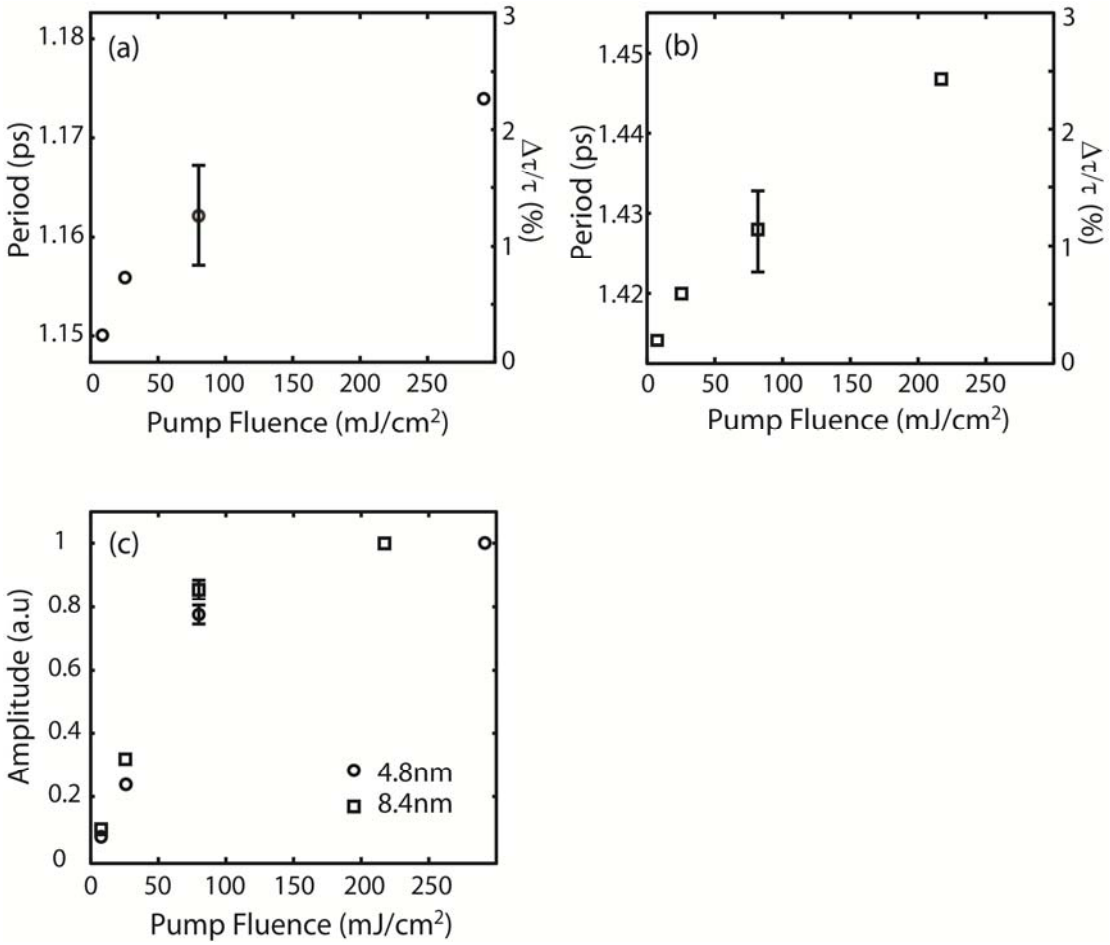

Figure 5.2. Excitation fluence dependence of coherent phonon period for 4.8 nm (a), and 8.3 nm (b) nanocrystals. Typical error bar is shown on each panel. On the right y-axis of (a) and (b), $\Delta\tau/\tau$ represents the fractional change of period $[\tau(F)-\tau(0)]/\tau(0)$ described in the text. (c) Excitation fluence dependence of the amplitude of oscillation in transient absorption data. The amplitudes are normalized to the maximum value for the nanocrystals of both sizes.

Excitation fluence-dependent period of coherent acoustic phonon is due to the temperature dependence of longitudinal and transverse sound velocities according to equation 5.1. For a majority of the materials, sound velocity can be approximated as a linearly decreasing function of temperature.[61] Therefore, the data shown in Figure 5.2 can be used to estimate the average lattice temperature if temperature-dependent sound velocity is known. Unfortunately, the data of temperature-dependent sound velocity are not available for Fe_3O_4 above 300K, making the direct determination of the lattice temperature from the present experimental data difficult. Nevertheless, a rough estimate of the lattice temperature has been made using the temperature-dependent sound velocity of $MgFe_2O_4$, which has the same cubic spinel structure as Fe_3O_4 with only 0.3% difference in the lattice parameter. The temperature dependence of the coherent phonon period calculated for $MgFe_2O_4$ was decreasing almost linearly to the temperature. From the comparison of the calculated fractional changes of the coherent phonon period at temperature T, $[\tau(T)-\tau(294\ K)]/\tau(29\ 4K)$, with $[\tau(F)-\tau(0)]/\tau(0)$ displayed in Figure 5.2, a rough estimate of the average lattice temperature was made. Figure 5.3 shows the excitation fluence dependence of the lattice temperature estimated as described above for both nanocrystal samples. This analysis indicates that the temperature rise (ΔT) of the lattice can be 300 K after the excitation at the highest excitation fluence of this study. The theoretical maximum ΔT, if the energy of all the absorbed photons is released as heat, is calculated to be 800 K under the same excitation fluence.[62] Actual temperature rise will be less than 800 K due to the finite time scale of the electronic relaxation and heat dissipation from the lattice to the surrounding. Considering the uncertainty in the

temperature-dependent sound velocity used, ΔT of 300 K seems a reasonable estimate for the temperature rise by the photoexcitation. Since the intervalence charge transfer transition centered at 1.5 μm was excited with 780 nm pump pulse, such temperature rise in the lattice may be possible from the rapid energy relaxation in the excited state.

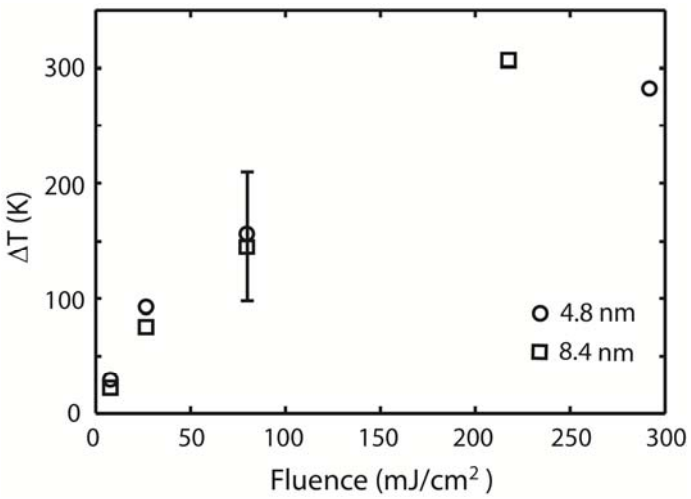

Figure 5.3. Excitation fluence dependence of the lattice temperature estimated from the period of coherent phonon. Error bar shown in the figure is a typical value.

5.4 Transient Lattice Temperature

In order to obtain information on the time dependent elastic property and the lattice temperature after the excitation, pump/probe transient absorption was measured employing two pump pulses. The first pump pulse with fluence of 265 mJ/cm^2 was used as the heating pulse. The second, weak pump pulse was used as the excitation pulse generating coherent phonon at various delay times with respect to the first pump pulse.

The combined energy of both pump pulses was 290 mJ/cm^2. The probe pulse with a variable time delay with respect to the second pump pulse recorded the transient absorption data. Typical two-pump/probe transient absorption data from 8.4 nm samples is shown in Figure 5.4(a). The period of the oscillation following the second pump pulse was extracted from the fitting of the data as described in the previous section. Figure 5.4(b) shows the period of coherent acoustic phonon at various time delays between the two pump pulses. The increased coherent phonon period due to the heating pulse recovered continuously as the time delay between the two pump pulses increased.

The recovery of the coherent phonon period with time represents the cooling of the lattice via dissipation of the heat to the surrounding solvent medium. Time-dependent temperature of the lattice was estimated from the time-dependent period of coherent phonon as described in the previous section. The temperature scale is indicated on the right y-axis of Figure 5.4(b). Although the number of data points is limited to reliably extract the time scale of lattice cooling, the lattice temperature recovered by about 40% after 100 ps. According to the earlier studies on the time-dependent lattice temperature of the photoexcited metal colloidal nanocrystals, the time scale of the temperature decay was relatively well described by a simple heat dissipation model; a sphere immersed in an infinite bath.[58,63] The following simple expression has been used to estimate the characteristic time scale for the heat dissipation (τ_d) in the limit of no interface effect on thermal conductance.[64]

$$\tau_d = \frac{r^2 C_p^2}{9 C_f \Lambda_f} \qquad 5.3$$

r and C_p are the radius and heat capacity per unit volume of the particle respectively. C_f and Λ_f are the heat capacity per unit volume and thermal conductivity of the fluid respectively. Although the temperature of the lattice in real situation does not decay exponentially and τ_d sets only a lower limit to the time scale the temperature decay, equation 5.3 can still gives a useful insight into the rate of heat dissipation in the nanocrystals. By using the literature value of C_p=3.22 J/cm^3·K, C_f =1.44 J/cm^3·K , and Λ_f = 0.123 W/m·K,[65-66] τ_d is calculated to be 110 ps for 8.4 nm Fe_3O_4 nanocrystals dispersed in cyclohexane. Considering the neglected effect of the finite interfacial heat conductance, the experimentally measured time scale of the lattice temperature decay is in reasonable agreement with the calculation using a crude model.

The result from this study can be applied, for instance, to assist the interpretation of the data from our earlier studies on the size-dependent magnetization dynamics in optically excited Fe_3O_4 nanocrystals.[56] Strongly size-dependent amplitude of the optically induced demagnetization was obtained at the excitation fluence of 50 mJ/cm^2. Based on the result from this study, the temperature rise (ΔT) in the nanocrystal at 100 ps is estimated to be about 50 K for 8.4 nm nanocrystals. Such temperature rise in the lattice is too small to explain the observed size-dependent demagnetization amplitude on ~100 ps time scale in terms of thermal excitation of spins by the heated lattice with size-dependent cooling rate.[67] Therefore, the possibility of the heated lattice with the size-dependent cooling rate being the origin of the size-dependent magnetization dynamics can be eliminated.

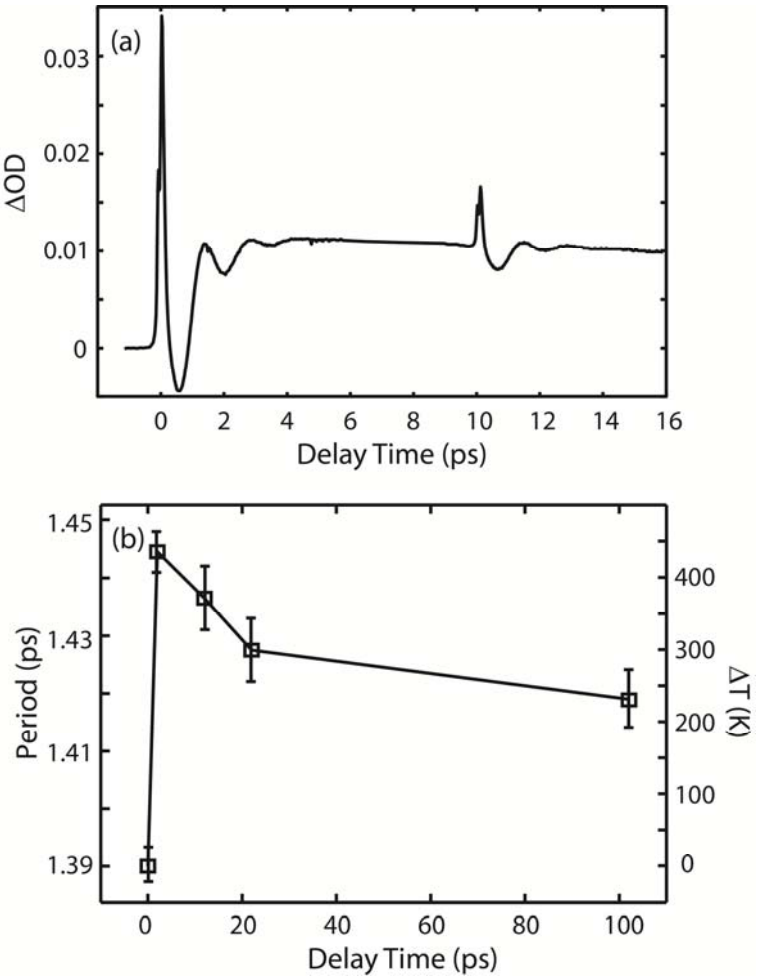

Figure 5.4. (a) Transient absorption data from two-pump/probe measurement. (b) Time dependence of the coherent phonon period and the estimated lattice temperature obtained from two-pump/probe measurement.

5.5 Summary

Excitation fluence and time-dependent elastic property and lattice temperature of the photoexcited colloidal magnetic nanocrystals were investigated by employing transient absorption spectroscopy. The period of coherent acoustic phonon was extracted by

fitting the oscillatory feature of the transient absorption data to an exponentially decaying cosine function. Since the period of coherent acoustic phonon is determined by the elastic constants, the lattice temperature was estimated from the temperature dependence of the elastic constants. Time-dependent lattice temperature was also estimated by employing two-pump/probe technique, where the first pump pulse acted as a heating pulse and the weaker second pump pulse created coherent phonon at various delay times. Information on the excitation fluence and time-dependent lattice temperature obtained in this study will be important in the investigation of optically induced dynamic magnetization and thermal transport in magnetic nanocrystals.

CHAPTER VI

SURFACE SPIN AND CHEMICAL TUNING EFFECT ON SPIN-LATTICE RELAXATION OF PHOTOEXCITED $Co_xFe_{3-x}O_4$ NANOCRYSTALS*

6.1 Introduction

Dynamics of spin relaxation in magnetic materials is a topic of active investigations in magnetism research in recent years.[20,68-69] The rate of energy and momentum flow between the spin and lattice, determining the time evolution of the magnetization, is not only of a fundamental interest in the study of magnetism but also has a strong technological relevance in the application of magnetic materials in spin-based electronic or data storage devices.[44,70-71]

One of the key factors determining the rate of energy flow from spin to lattice degrees of freedom, i.e., spin-lattice relaxation, is spin-orbit coupling.[4] The effective strength of spin-orbit interaction in ferromagnetic solids is determined not only by the intrinsic atomic spin-orbit coupling strength but also by the ligand field that depends on the details of the local lattice structure and symmetry.[4,72] In nanoscale magnetic materials, there are many surface spins under different ligand fields from those of the interior spins due to the structural discontinuity on the surface.

---

* Reprinted in part with permission from J. Phys. Chem. C, *114* Chen, T. –Y.; Hsia, C.-H.; Chen, H. –Y.; Son, D. H.; "Size Effect on Chemical Tuning of Spin-Lattice Relaxation Dynamics in Superparamagnetic Nanocrystals" 9713, Copyright 2010 by the American Chemical Society.

Therefore, one would expect that the rate of energy and momentum transfer in spin degrees of freedom in nanoscale magnetic materials be significantly influenced by the surface spins.

On the other hand, spin-orbit coupling can often be tuned by varying the stoichiometry of the materials as well. For example, the average spin-orbit coupling in ferrites ($M_xFe_{3-x}O_4$, M = divalent metal ion) can be tuned by varying the identity and composition of M.[73-74] Earlier studies on the dynamics of spin-lattice relaxation and its correlation to the structure of the magnetic materials have focused primarily on bulk and thin film phases.[75-78] Recently, interests in the dynamic magnetism in nanoscale magnetic materials are growing rapidly,[69] since the reduction in length scale generally has a strong influence on the dynamics of energy relaxation in various degrees of freedom.[79]

The dynamics of energy relaxation in nanoscale materials has been well studied for the electronic relaxation in semiconductors and metals, where the quantum confinement in combination with the large surface area plays a critical role in modifying the dynamics.[80-82] In the case of spin-lattice relaxation in magnetic materials, a large portion of the surface in nanocrystals can also influence the dynamics of spin-lattice relaxation due to the potentially different spin-orbit coupling or (and) vibronic coupling from the bulk.

Since both surface spins and chemical tuning will affect effective spin-orbit coupling strength and therefore spin-lattice relaxation. One interesting question that arises from this is that whether the relative efficiency of the surface of the nanocrystals in spin-

lattice relaxation will vary with spin-orbit coupling of the bulk phase. An equivalent question from a different perspective is how the large surface area in nanocrystals would affect the chemical tunability of spin-lattice relaxation rate.

In this chapter, we discuss the chemical tunabililty of spin-lattice relaxation rate in nanoscale magnetic materials using size and composition-controlled colloidal superparamagnetic $Co_xFe_{3-x}O_4$ nanocrystals as the model system. $Co_xFe_{3-x}O_4$ is particularly useful for the purpose of this study, since magnetocrystalline anisotropy reflecting the bulk spin-orbit coupling strength can be varied by ~20 fold by tuning cobalt content (x) without changing the lattice structure and static magnetization significantly.[2,83-86] Furthermore, highly dispersible nature of the superparamagnetic nanocrystals in liquid medium allows us to study the dynamic magnetism unaffected by the interparticle magnetic dipole-dipole interaction.[87] While superparamagnetism is less useful for device applications, fine tunability of the size and stoichiometry of the nanocrystals offers a unique opportunity to obtain a useful insight into the dynamics of spin-lattice relaxation in nanoscale materials.

To measure the spin-lattice relaxation rate of $Co_xFe_{3-x}O_4$ nanocrystals, we employed pump-probe Faraday rotation technique that allowed us to monitor the time-dependent magnetization with a very high time resolution (< 100 fs). The results of this study indicate that the chemical tunability of spin-lattice relaxation rate becomes weaker with decreasing particle size and that the size dependence of spin-lattice relaxation rate becomes weaker with increasing bulk spin-orbit coupling. These observations were explained in terms of the weaker chemical tunability of spin-orbit coupling on the

surface than in the interior of the nanocrystal using a simple model for spin-lattice relaxation that has both surface and interior contributions.

6.2 Experimental Section

6.2.1 Sample preparation

Spherical $Co_xFe_{3-x}O_4$ nanocrystals passivated with oleic acid with varying cobalt content (x) in the range of $0 < x < 0.9$ and diameter range of 5-15 nm were synthesized and characterized as described in Chapter III.

6.2.2 Measurement of static mass magnetization and blocking temperature

Static mass magnetization and blocking temperature of spherical $Co_xFe_{3-x}O_4$ nanocrystals with various particle diameters were measured as described in Chapter III.

6.2.3 Pump-probe Faraday rotation measurement

Spin-lattice relaxation rate in $Co_xFe_{3-x}O_4$ nanocrystals following an optical excitation was measured employing pump-probe Faraday rotation technique as described in Chapter III. Faraday rotation is a magnetooptic technique that measures the relative magnitude of the magnetization indirectly from the rotation of polarization angle of the linearly polarized light passing through the magnetic material. In this process, time-dependent absorption of the probe light by the sample was corrected for by simultaneously measuring the total intensity of the transmitted probe light. The external magnetic field of 0.35 T was provided by a pair of permanent magnet in the direction

either parallel or antiparallel to the direction of the probe beam. Pump-probe Faraday rotation normalized to static Faraday rotation, $\Delta\theta(t)/\theta_0$, was taken to represent the time-dependent fractional changes in magnetization $|\Delta M(t)|/|M_0|$. In order to remove any potential non-magnetic contribution to Faraday rotation signal, the difference between the two data sets obtained with the magnetic fields parallel and antiparellel to the probe beam was taken to report $\Delta\theta(t)/\theta_0$.

For all the measurements, colloidal $Co_xFe_{3-x}O_4$ nanocrystal samples dispersed in 1-octadecene at room temperature were used. The sample solutions were continuously circulated at the linear speed of several m/sec through a jet nozzle (400 μm thick, 4 mm wide) to prevent potential thermal effect and sample damage by the repeated exposure of the same sample region to the pump beam. Relatively high viscosity of 1-octadecene provided a sufficiently stable jet stream with a flat surface for the reliable measurements of Faraday rotation. The concentration of nanocrystals was maintained near 10^{-5} M or below to avoid interparticle dipole-dipole interaction that can potentially influence the dynamics.[87] Since the absorbance of $Co_xFe_{3-x}O_4$ nanocrystal samples at the pump wavelength (λ = 790 nm) varied slightly with cobalt content (Figure 6.1), the pump fluence was adjusted to ensure the same average excitation density, i.e., number of photons absorbed per unit volume of nanocrystal, in all the measurements. All the fluence values reported here are the average fluence within the fwhm (30 μm) of the probe beam.

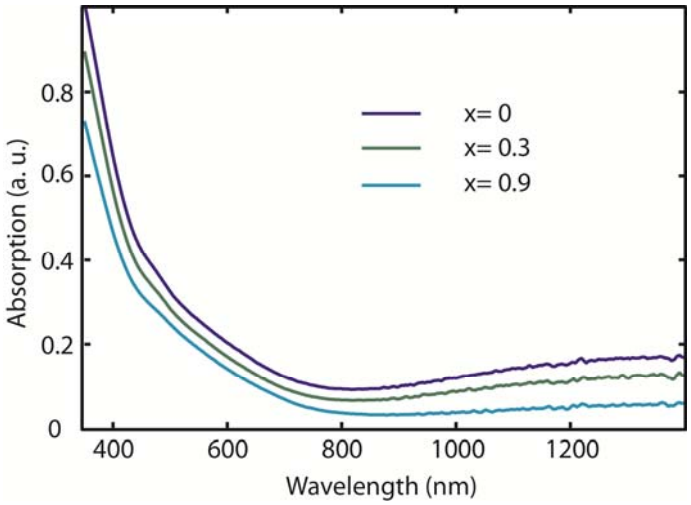

Figure 6.1. UV-Vis-NIR spectra of 7 nm $Co_xFe_{3-x}O_4$ nanocrystals.

6.3 Measurement of Spin-Lattice Relaxation Rate of Spherical $Co_xFe_{3-x}O_4$ Nanocrystals

Spin-lattice relaxation rate of $Co_xFe_{3-x}O_4$ nanocrystals was obtained from the pump-probe Faraday rotation data showing the recovery of the magnetization following the optically induced demagnetization. Figure 6.2 shows the representative pump-probe Faraday rotation data from 7 nm $Co_{0.9}Fe_{2.1}O_4$ nanocrystals under the external magnetic field applied parallel ($\Delta\theta_1$) and antiparallel ($\Delta\theta_2$) to the direction of the probe beam. All the reported $\Delta\theta(t)/\theta_0$ data here were obtained from $\Delta\theta(t) = (\Delta\theta_2-\Delta\theta_1)/2$ to remove the potential non-magnetic component of the signal not sensitive to the polarity of the external magnetic field. The general feature of the pump-probe Faraday rotation data of $Co_xFe_{3-x}O_4$ nanocrystals is the immediate demagnetization by the absorption of the pump beam followed by the recovery of the magnetization. While the photoinduced ultrafast

demagnetization in magnetic materials is also a topic of strong interest by itself,[46,75,88-89] we will mainly focus on the dynamics of the recovery of the magnetization occurring via spin-lattice relaxation in this study.

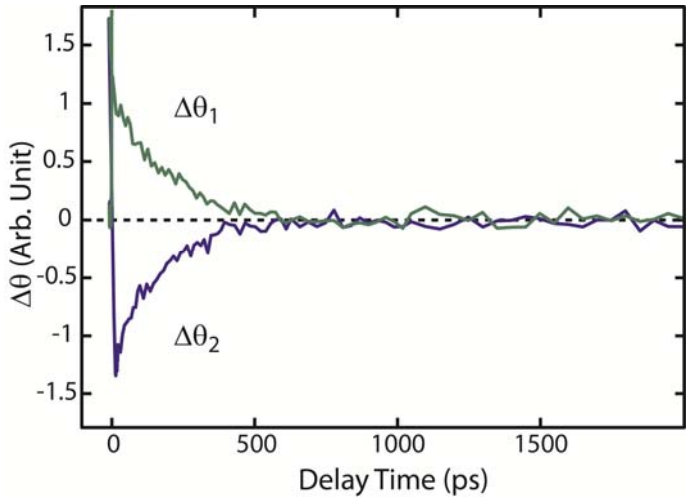

Figure 6.2. Pump-probe Faraday rotation data of 7 nm $Co_{0.9}Fe_{2.1}O_4$ nanocrystals under opposite external magnetic fields.

The time scale of spin-lattice relaxation (τ_{SLR}) was extracted by biexponetial fitting of $\Delta\theta(t)/\theta_0$ data. For all the data, the recovery of the signal could be fitted with two exponential time constants: ~ 10 ps and several hundreds of ps. Such multiexponential recovery of magnetization has been previously observed in a number of ferromagnetic thin films.[76,90-91] Here, the recovery of $\Delta\theta(t)/\theta_0$ on the time scale of hundreds of ps is of our interest, which is ascribed to spin-lattice relaxation. The origin of the dynamics on

~10 ps time scale, on the other hand, is less clear although the dynamics on short time scale has been previously associated with spin-spin relaxation between spin waves of different wavelengths in ferromagnetic metals.[92] Rotational diffusion of nanocrystal in the solvent medium and directional fluctuation of magnetization is much slower than the time scale of the process we are interested in this study and do not affect the dynamics reported here.[86]

In order to obtain a reliable spin-lattice relaxation rate of photoexcited $Co_xFe_{3-x}O_4$ nanocrystals, the Faraday rotation data were obtained at several different probe wavelengths and excitation fluences to check the consistency of the dynamics. Figure 6.3(a) shows $\Delta\theta(t)/\theta_0$ data from 7 nm $Co_{0.9}Fe_{2.1}O_4$ nanocrystals probed at three different wavelengths, λ = 560, 635, and 900 nm. The dynamics represented in these data do not exhibit significant spectral dependence as expected from $\Delta\theta(t)/\theta_0$ representing the magnetization dynamics.[78]

In order to avoid potential alteration of the dynamics of magnetization recovery by the heated lattice, dependence of $\Delta\theta(t)/\theta_0$ on the excitation intensity was also checked. Figure 6.3(b) shows $\Delta\theta(t)/\theta_0$ data from 7 nm $Co_{0.9}Fe_{2.1}O_4$ nanocrystals at three different excitation fluences normalized to the excitation fluence. At these fluences, the amplitudes of the signal increased linearly to the excitation fluence and were almost identical when normalized to the excitation fluence. At higher excitation fluences, however, peak amplitude near zero time delay began to saturate and exhibited a non-monotonic recovery dynamics. In this study, the excitation fluence was maintained on the low side of the linear regime (< 50 mJ/cm^2) to avoid any potential complications by

the heated lattice. According to our earlier study on the transient lattice temperature in photoexcited Fe_3O_4 nanocrystals, the initial temperature rise a few ps after the excitation at the pump fluence of this study was < 100 K and became < 50 K within 100 ps in 7 nm nanocrystals.[93]

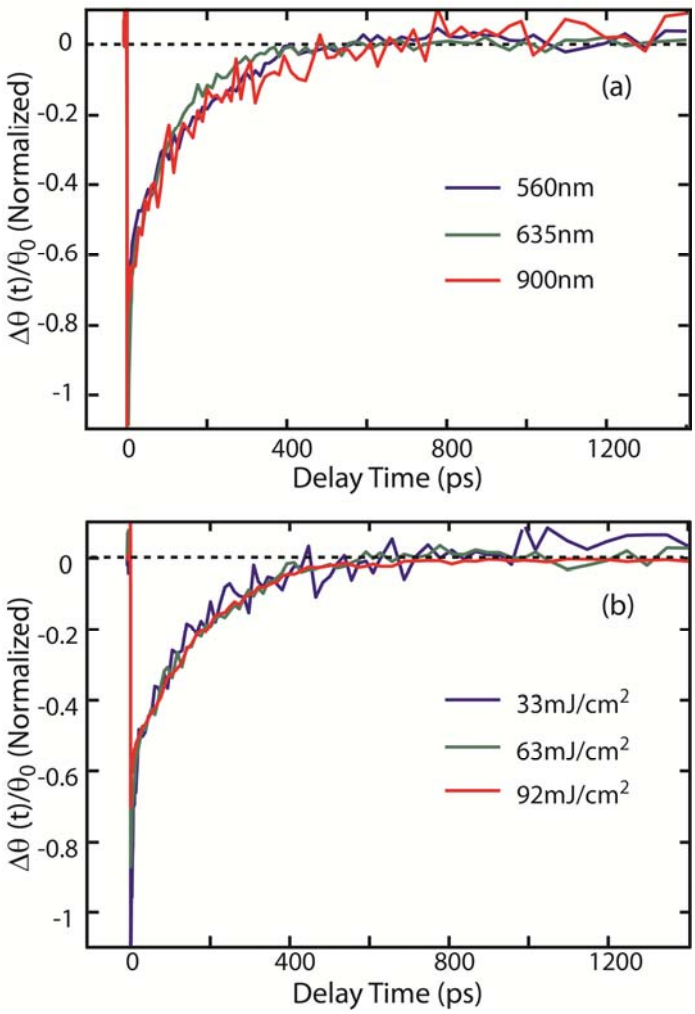

Figure 6.3. (a) Probe wavelength-dependent $\Delta\theta(t)/\theta_0$ of 7 nm $Co_{0.9}Fe_{2.1}O_4$ nanocrystals. (b) Excitation fluence-dependent $\Delta\theta(t)/\theta_0$ data normalized to pump fluence.

Insensitivity of the dynamics to the pump fluence shown in Figure 6.3(b) suggests that the relatively low temperature rise and fast cooling of the lattice combined with high Curie temperature of $Co_xFe_{3-x}O_4$ does not affect the dynamics of the magnetization recovery. In this study, all the reported spin-lattice relaxation rates are the average of the values obtained from the measurements at these probe wavelengths and at the excitation fluence of < 50 mJ/cm^2.

6.4 Chemical Tuning of Spin-Lattice Relaxation Rate of $Co_xFe_{3-x}O_4$ Nanocrystals

In order to investigate the effect of varying cobalt content (x) on spin-lattice relaxation rate and examine the correlation with spin-orbit coupling, the pump-probe Faraday rotation data of $Co_xFe_{3-x}O_4$ nanocrystal samples were obtained in the range of $0 < x < 0.9$. Figure 6.4(a)-(e) show $\Delta\theta(t)/\theta_0$ data of 7 nm $Co_xFe_{3-x}O_4$ nanocrystals measured with 790 nm pump and 635 nm probe. Spin-lattice relaxation time (τ_{SLR}) obtained as described in the previous section is also displayed for each value of x. Figure 6.5(a) shows spin-lattice relaxation rate ($1/\tau_{SLR}$) as a function of x. As cobalt content increases from $x = 0$ to 0.9, $1/\tau_{SLR}$ also increases by ~ 60%. On the other hand, transient absorption dynamics did not exhibit significant dependence on cobalt content, suggesting relatively week influence of cobalt substitution on the dynamics of electronic relaxation (Figure 6.6).

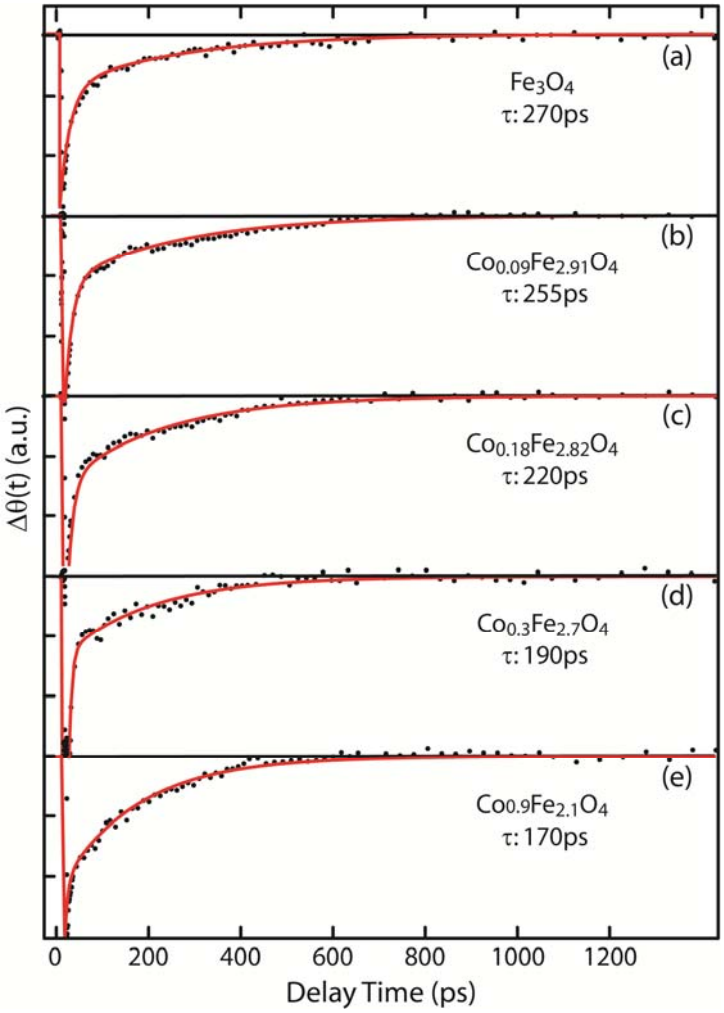

Figure 6.4. Cobalt content-dependent Δθ(t) data of 7 nm $Co_xFe_{3-x}O_4$ nanocrystals, x = 0, 0.09, 0.18, 0.3, and 0.9 for (a) to (e) respectively.

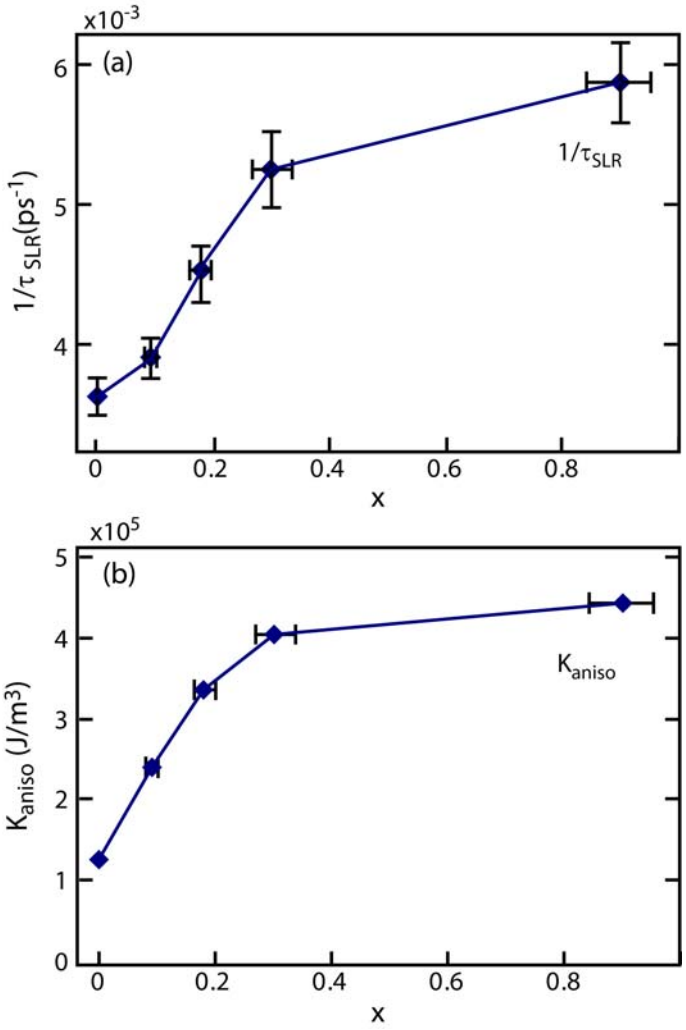

Figure 6.5. (a) Spin-lattice relaxation rate ($1/\tau_{SLR}$) and (b) magnetic anisotropy constant (K_{aniso}) of 7 nm $Co_xFe_{3-x}O_4$ nanocrystals as a function of cobalt content (x).

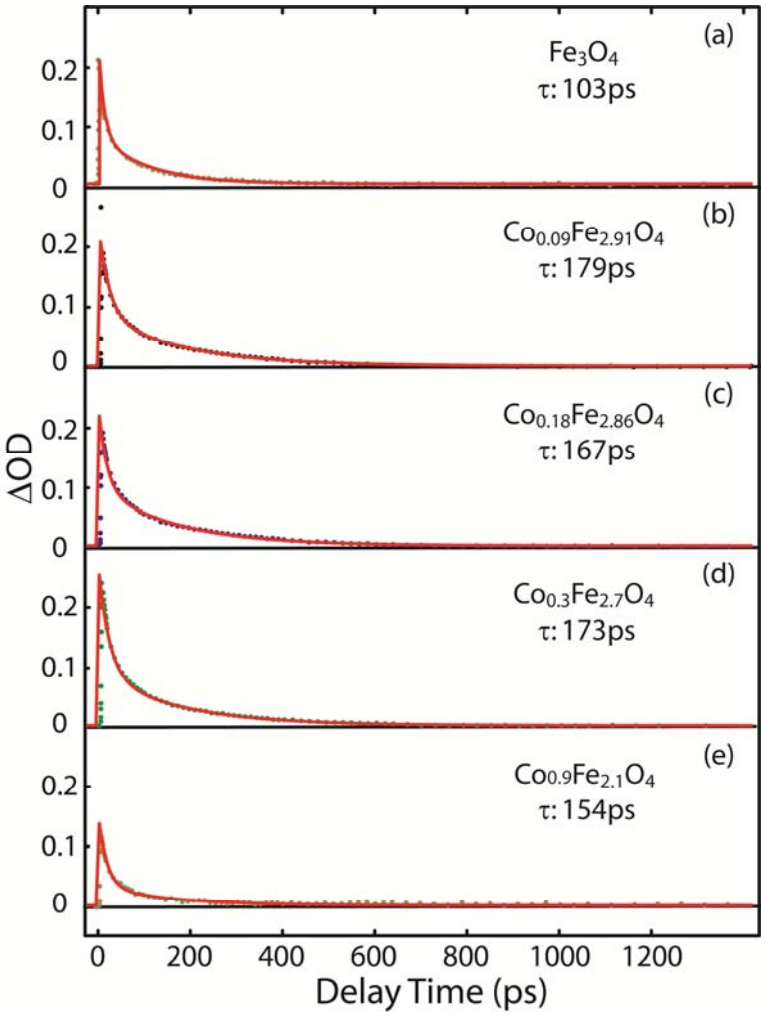

Figure 6.6. Cobalt content-dependent transient absorption data of 7 nm $Co_xFe_{3-x}O_4$ nanocrystals with 780 nm pump and 635 nm probe, x = 0, 0.09, 0.18, 0.3, and 0.9 for (a) to (e) respectively.

In principle, the dependence of τ_{SLR} on cobalt content can originate from both the differences in spin-orbit coupling and vibronic coupling, since spin-lattice relaxation requires both of them. Because $CoFe_2O_4$ and Fe_3O_4 have very similar lattice structures,

heat capacities, and vibrational spectra,[2,83-84] while their bulk magnetocrystalline anisotropies are different by a factor of ~20 (1.1-1.3×10^4 J/m^3 for Fe_3O_4, 1.8-3.0×10^5 J/m^3 for $CoFe_2O_4$),[85-86] *x*-dependent τ_{SLR} observed in $Co_xFe_{3-x}O_4$ nanocrystals can be ascribed mainly to the differences in spin-orbit coupling.

In order to further examine the connection between the spin-lattice relaxation rate ($1/\tau_{SLR}$) with spin-orbit coupling of $Co_xFe_{3-x}O_4$ nanocrystals, *x*-dependence of magnetic anisotropy (K_{aniso}) is also measured as shown in Figure 6.5(b). For bulk magnetic materials, magnetocrystalline anisotropy (K_{mca}) reflecting the strength of spin-orbit coupling of the bulk is the dominating component of the total magnetic anisotropy (K_{aniso}). In materials with simple uniaxial anisotropy, K_{mca} essentially represents the difference in spin-orbit energy between the direction of easy and hard axis, which is quadratically proportional to spin-orbit coupling.[94] For this reason, spin-lattice relaxation rate of bulk magnetic materials was often correlated with K_{mca} in the earlier studies. In this study, we will use K_{aniso} as only an approximate parameter reflecting average spin-orbit coupling strength in $Co_xFe_{3-x}O_4$ nanocrystals as will be discussed further in detail later.

In Figure 6.5(a) and 6.5(b), both $1/\tau_{SLR}$ and K_{aniso} exhibit a similar trend, including the initial increase in the range of $0 < x < 0.3$ and subsequent saturation at higher values of *x*. This resemblance strongly indicates that the variation of spin-lattice relaxation rate is correlated with *x*-dependent spin-orbit coupling strength in $Co_xFe_{3-x}O_4$ nanocrystals. However, K_{aniso} should be taken more cautiously as a measure of the average spin-orbit coupling strength of $Co_xFe_{3-x}O_4$ nanocrystals. In the case of nanocrystals, other

contributing components to K_{aniso}, such as surface anisotropy (K_s), becomes significant and can even dominate in small nanocrystals. For spherical magnetic nanocrystals of diameter *d*, the following empirical relationship has often been used to describe K_{aniso}, although K_s is a more complex function of the surface and lattice structure in reality.

$$K_{aniso} = (K_{mca} + 6K_s/d) \quad 6.1$$

The connection between surface anisotropy (K_s) and surface spin-orbit coupling is more complicated than in the bulk due to the complexity of the surface structure and symmetry that influences the surface anisotropy.[95-96] This introduces some uncertainty in K_{aniso} as the parameter representing the average spin-orbit coupling of the nanocrystals, making a quantitative correlation between K_{aniso} and $1/\tau_{SLR}$ more challenging in nanocrystals than in bulk. Nevertheless, the similarity of *x*-dependence of $1/\tau_{SLR}$ and K_{aniso} shown in Figure 6.5(a) and 6.5(b) clearly exhibits the tunablity of spin-lattice relaxation rate in nanocrystals via chemical tuning of the average spin-orbit coupling strength of the nanocrystals.

It is noteworthy to point out that 60% change in spin-lattice relaxation rate observed in 7 nm $Co_xFe_{3-x}O_4$ nanocrystals within the range of $0 < x < 0.9$ in Figure 6.5(a) is narrower than what one might expect in bulk phase. In bulk phase of $Co_xFe_{3-x}O_4$, magnetocrystalline anisotropy increases by ~20 fold from Fe_3O_4 to $CoFe_2O_4$. According to the earlier studies on spin relaxation dynamics in thin films of chromium chalcogenides, spin-lattice relaxation rate increased roughly linearly to bulk magnetocrystalline anisotropy although the correlation was crude.[97] In a recent study by Hübner et al., spin-lattice relaxation rate in bulk metallic ferromagnets was predicted to

be quadratically proportional to K_{mca} at high temperatures, while more comprehensive experimental verification has yet to be made.[98] Despite the uncertainties in the correlation between spin-orbit coupling and spin-lattice relaxation rate from the studies in bulk, the range of spin-lattice relaxation rates observed in $Co_xFe_{3-x}O_4$ nanocrystals still seems significantly narrower than that of K_{mca}.

This raises an interesting question on whether the chemical tuning of spin-lattice relaxation rate is affected by the length scale of the materials. Considering our recent findings of the presence of the size effect on spin-lattice relaxation rate in Fe_3O_4 nanocrystals arising from the stronger spin-orbit coupling of surface,[99] such possibility is conceivable. In order to examine whether the range of chemical tuning in nanocrystals differ from the bulk, information on spin-lattice relaxation rate in bulk $Co_xFe_{3-x}O_4$ is needed. Unfortunately, the data on spin-lattice relaxation rate in bulk phase required to make a direct comparison with the result from this work are not so far available. Although previous studies employing ferromagnetic resonance investigated spin relaxation rate indirectly from the resonance line width, it was considered to reflect mostly spin-spin relaxation rather than spin-lattice relaxation.[100] Despite the lack of bulk data, a valuable insight can be obtained by comparing the spin-lattice relaxation rates in $Co_xFe_{3-x}O_4$ nanocrystals of varying particle sizes. In the next section, we will discuss how the chemical tuning of spin-lattice relaxation is influenced by the size of the nanocrystals in more detail.

6.5 Size Effect on Chemical Tuning of Spin-Lattice Relaxation in $Co_xFe_{3-x}O_4$ Nanocrystals

In order to investigate the potential effect of varying the size on the chemical tuning of spin-lattice relaxation rate in $Co_xFe_{3-x}O_4$ nanocrystals, more extensive measurements of *x*-dependent spin-lattice relaxation rate were made at varying particle sizes. The diameter of the spherical $Co_xFe_{3-x}O_4$ nanocrystal was varied in the range of 5-15 nm, while keeping all the samples below the superparamagnetic limit. Spin-lattice relaxation rates ($1/\tau_{SLR}$) of these nanocrystal samples measured under the identical excitation densities are summarized in Table 6.1.

Table 6.1. Spin-lattice relaxation rates ($1/\tau_{SLR}$) of $Co_xFe_{3-x}O_4$ nanocrystals.

Diameter (nm)	*x*					
	0	0.09	0.18	0.3	0.53	0.9
5	3.9 ± 0.1					
7	3.6 ± 0.1	3.9 ± 0.1	4.5 ± 0.2	5.3 ± 0.3	5.5 ± 0.3	5.8 ± 0.3
9	3.4 ± 0.1					
10	3.1 ± 0.1	3.9 ± 0.1		4.8 ± 0.2	5.2 ± 0.3	5.5 ± 0.3
15	2.9 ± 0.1				5.0 ± 0.3	

unit: 10^{-3} ps^{-1}

In Figure 6.7, the ranges of the chemical tuning of spin-lattice relaxation rates of $Co_xFe_{3-x}O_4$ nanocrystals are compared for the two particle diameters, 7 and 10 nm. To delineate the difference more clearly, relative values of $1/\tau_{SLR}$ normalized to that of Fe_3O_4 nanocrystal samples are compared. For both sizes, spin-lattice relaxation becomes faster with the increase of cobalt content. However, the ranges of the relative and

absolute values of $1/\tau_{SLR}$ are larger in the larger nanocrystals. As cobalt content increased from x = 0 to 0.9, $1/\tau_{SLR}$ increased by 60% and 80% for 7 nm and 10 nm nanocrystals respectively. 15 nm nanocrystals follows the same trend between x = 0 and 0.53. This result indicates that the chemical tunability of spin-lattice relaxation rate becomes weaker as the nanocrystal becomes smaller.

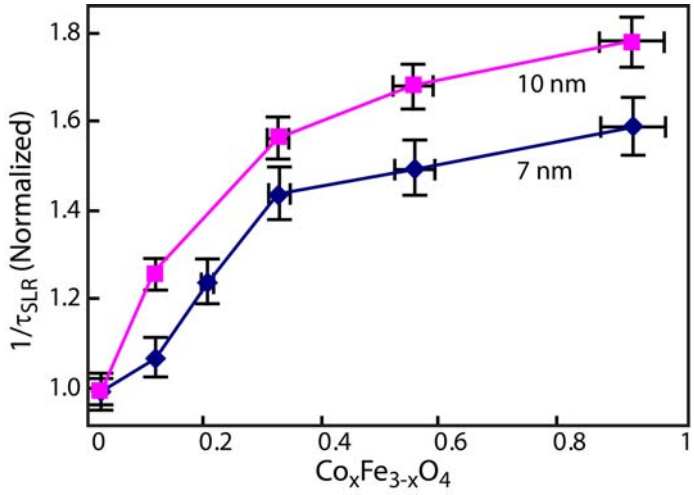

Figure 6.7. Comparison of the x-dependent relative spin-lattice relaxation rates of $Co_xFe_{3-x}O_4$ nanocrystals at two different particle diameters.

In Figure 6.8, the size dependence of spin-lattice relaxation rate is compared for the two different cobalt contents, x = 0 and 0.53. To facilitate the comparison, the relative values of $1/\tau_{SLR}$ normalized to that of 15 nm nanocrystal sample are plotted as a function of the diameter. The data indicate that $Co_xFe_{3-x}O_4$ nanocrystals with higher cobalt

content, i.e., with stronger bulk spin-orbit coupling, exhibit the weaker dependence of spin-lattice relaxation rate on the particle size.

These observations clearly indicate that varying cobalt content does not have the same effect on spin-lattice relaxation of $Co_xFe_{3-x}O_4$ nanocrystals of different sizes. An insight into the size-dependent chemical tuning of spin-lattice relaxation rate may be obtained by considering the role of surface in spin-lattice relaxation of nanocrystals.

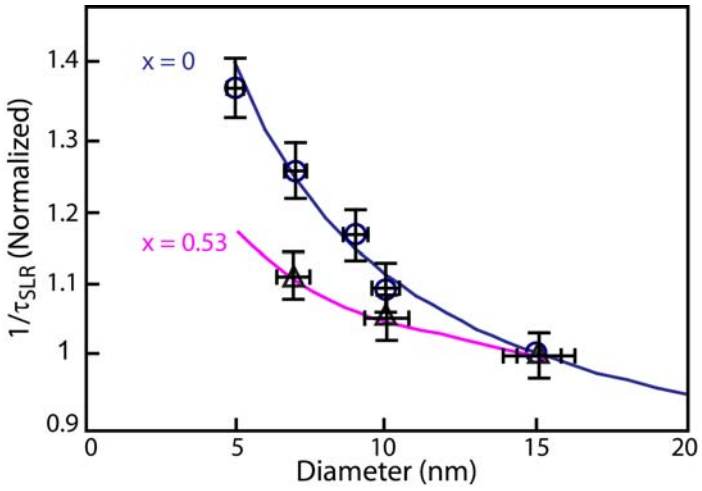

Figure 6.8. Comparison of the size-dependent relative spin-lattice relaxation rates of $Co_xFe_{3-x}O_4$ nanocrystals at two different cobalt contents.

According to Fermi's golden rule, spin-lattice relaxation rate ($1/\tau_{SLR}$) is proportional to the square of the coupling Hamiltonian term ($|\langle V \rangle|^2$) between the spinorbit perturbed ligand field states, where the Hamiltonian V is the fluctuating electric potential of the ligand. Here, we assume ($|\langle V \rangle|^2$) of nanocrystals has contributions from the interior

($|<V_i>|^2$) and the surface ($|<V_s>|^2$) proportionally to the fraction of the interior (*fi*) and surface (*fs*) spins. A similar model incorporating the surface contribution in the energy relaxation has been used to explain exciton relaxation dynamics in quantum dots.

$$1/\tau_{SLR} \propto |<V>|^2 = f_i \cdot |<V_i>|^2 + f_s \cdot |<V_s>|^2 \qquad 6.2$$

Using this model, we estimated the relative efficiency of the surface in spin-lattice relaxation with respect to the interior. The values of f_i and f_s depend on the thickness (t) of the surface region, which is somewhat arbitrary. In our analysis, we chose the values of t between 3 and 5 Å that contain the outermost atomic layer. From the analysis of $1/\tau_{SLR}$ vs. diameter of Fe_3O_4 nanocrystals, it was concluded that the surface is 3 times more efficient than the interior of the nanocrystals in spin-lattice relaxation, i.e., $|<V_s>|^2/|<V_i>|^2 = 3$.[99]

Stronger spin-orbit coupling at the surface can be justified as follows. In magnetic crystals, the effective spin-orbit energy (E_{so}), representing the strength of spin-orbit coupling, is on the order of $\xi^2/\Delta E$, where ξ is the atomic spin-orbit coupling parameter and ΔE is the ligand field splitting energy. In $Co_xFe_{3-x}O_4$ nanocrystals, metal ions have a smaller number of oxygen ligand on the surface than in the interior. The lacking oxygen ligand is replaced with weakly bound carboxylic group of oleic acid used as the surfactant. Therefore, the ligand field acting on the surface spins is smaller than that of the interior spins. Consequently, E_{so} of the surface spins can be larger than that of the

interior spins, resulting in a decreasing average E_{so} with increasing nanocrystal size.

When the same analysis is made on $Co_{0.53}Fe_{2.47}O_4$ nanocrystals, $|<V_s>|^2/|<V_i>|^2$ is 1.7. This suggests that the observed size dependence of the chemical tuning of spin-lattice relaxation can be explained if $|<V_s>|^2$ is less chemically sensitive than $|<V_i>|^2$. In such situation, the range of chemical tuning of spin-lattice relaxation will become smaller as the contribution of the surface to the overall spin-lattice relaxation increases. One would also expect the weaker size dependence of spin-lattice relaxation rate with increasing bulk spin-orbit coupling due to the decreasing contribution of the surface in determining the overall spin-lattice relaxation rate. Since the electronic relaxation rate of $Co_xFe_{3-x}O_4$ nanocrystals through vibronic coupling is not sensitive to cobalt content, the weaker chemical tunability of $|<V_s>|^2$ can be interpreted as the weaker tunability of spin-orbit coupling on the surface.

The relatively weak chemical tunability of spin-orbit coupling on the surface compared to the interior of the nanocrystals could arise from different causes. For instance, inhomogeneous distribution of cobalt ions with preferential occupation in the interior region of the nanocrystal may weaken the chemical sensitivity of surface spin-orbit coupling. We do not think this is a likely situation, since cobalt ions are considered to distribute homogeneously in the nanocrystals prepared at the high reaction temperatures of this study (290°C).[101] On the other hand, more complex ligand field on the surface could diminish the chemical sensitivity of the effective surface spin-orbit coupling, since the ligand field is another important factor affecting the effective spin-orbit coupling in crystalline materials. While further studies are needed for a more direct

evidence for the weaker chemical sensitivity of surface spin-orbit coupling and its cause, this study offers a simple framework to interpret the size and stoichiometry-dependent spin-lattice relaxation rates in superparamagnetic nanocrystals.

6.6. Summary

In summary, the surface spin and chemical tunability effect on spin-lattice relaxation rates in colloidal superparamagnetic $Co_xFe_{3-x}O_4$ nanocrystals was investigated. Spin-lattice relaxation rate increases with decrease of particle diameter is due to the fact that larger portion of the contribution to spin-orbit coupling is from surface spins. With increasing cobalt content (x), spin-lattice relaxation rate increases due to the increase in spin-orbit coupling strength regardless of the particle size. However, the range of chemical tunability of spin-lattice relaxation rate becomes narrower with the decreasing particle size. Furthermore, the size dependence of spin-lattice relaxation rate becomes weaker as cobalt content increases in $Co_xFe_{3-x}O_4$ nanocrystals. These observations suggest that spin-orbit coupling of the surface is less sensitive to stoichiometric variation than the interior of the nanocrystals.

CHAPTER VII

GENERAL CONCLUSIONS

7.1. Concluding Remarks

In conclusion, the electronic and magnetization dynamics of photoexcited $Co_xFe_{3-x}O_4$ nanocrystals have been studied through transient absorption and pump-probe Faraday rotation measurements. The results from this study provide information on how energy dissipates in and between electron, spin, and lattice degrees of freedoms in photoexcited magnetic nanocrystals as a function of particle size and chemical composition. Such a material structure-dynamic properties study in magnetic nanocrystals may be useful for spin-based electronics devices in nanometer length scale in the future.

$Co_xFe_{3-x}O_4$ nanocrystals were chosen as our model system to study the relationship between material structure and dynamic properties due to the fact that the synthesis procedure is well-established, the chemical composition can be easily controlled, and static physical properties are well studied in the bulk phase. Through all measurements in experiments in the dissertation, all nanocrystals were dissolved in organic solvent so that the effect of dipole-dipole interaction between each nanocrystal on electronic and magnetization can be ignored.

In magnetic materials, the energy can be stored in electron, spin, and lattice degrees of freedom. The focus of this dissertation is to understand specifically how the energies relax and dissipate in electron and spin to lattice degrees of freedom after photoexcitation of magnetic nanocrystals. Study of electronic/spin relaxation is accessed

by adapting transient absorption/pump-probe Faraday rotation measurements, where the data provided the information on energy relaxation in electron/spin and energy dissipation between electron-lattice/spin-lattice degrees of freedom. Lattice temperature dynamics of phtoexcited nanocrystals is also investigated in this dissertation to clarify the issue that the magnetization signal is not from the heating of lattice. Brief conclusion will be given in the following.

Electronic relaxation dynamics of excited intervalecne charge transfer states of Fe_3O_4 nanocrystals were studied through transient absorption measurements. The excited charge transfer state exhibited an ultrafast (100 fs) back energy transfer to the neighboring octahedral Fe^{2+} ions, and subsequently went through the vibrational and electronic relaxation in 1 and ~100 ps, respectively. Furthermore, the charge transfer excitation created coherent acoustic phonons, resulting in strong oscillations in the transient absorption data. The strong oscillation of the absorption has been explained in terms of the modulated oscillator strength of the charge transfer transitions. The present observation demonstrates that the charge transfer excitation can create coherent phonons in the transition metal oxide nanocrystals, which can dynamically modify their material properties. Size effect on electronic relaxation dynamics is not distinct due to the localized nature of interavlece charge transfer of transition metal oxide nanocrystals.

Information on lattice temperatures of photoexcited Fe_3O_4 nanocrystals were extracted from the oscillatory feature of transient absorption data. Excitation fluence and time-dependent elastic property and lattice temperature of the photoexcited colloidal magnetic nanocrystals were investigated. The period of the coherent acoustic phonon

was extracted by fitting the oscillatory feature of the transient absorption data to an exponentially decaying cosine function. Since the period of the coherent acoustic phonon is determined by the elastic constants, the lattice temperature was estimated from the temperature dependence of the elastic constants. Time-dependent lattice temperature was also estimated by employing two-pump/probe technique, where the first pump pulse acted as a heating pulse and the weaker second pump pulse created coherent phonon at various delay times. Information on the excitation fluence and time-dependent lattice temperature obtained in this study will be important in the investigation of optically induced dynamic magnetization and thermal transport in magnetic nanocrystals. The degree of demagnetization caused by the 100 K lattice temperature rise is less than 5%.

Magnetization dynamics of photoexcited $Co_xFe_{3-x}O_4$ nanocrystals have been studied via pump-probe Faraday rotation measurements. The general features of magnetization dynamics data included sub-ps demagnetization and then recovery in magnetization with tens and hundreds of ps time scales. The recovery of magnetization in hundreds ps is assigned as spin-lattice relaxation process and the effects of size and chemical composition are addressed. With smaller nanocrystal size and higher Co substitution, faster spin-lattice relaxation rate was observed due to the stronger effective spin-orbit coupling strength. Effective spin-orbit coupling strength is determined by the intrinsic spin-orbit coupling strength (ζ) and the ligand field splitting energy (ΔE) and is proportional to $\left(\frac{\zeta}{\Delta E}\right)$. In nanocrystals, unlike the Fe ions in the interior with order crystal structures, the Fe ions on the surface typically have a smaller number of ligands

which results in a smaller ligand field splitting energy and thus stronger effective spin-orbit coupling strength. In that sense, smaller nanocrystals have larger portion of surface spins and thus have a faster spin-lattice relaxation rate. On the other hand, higher Co substitution nanocrystals showed faster spin-lattice relaxation can be explained via increasing intrinsic spin-orbit coupling strength (ζ). However, the range of chemical tunability of the spin-lattice relaxation rate is narrower in smaller nanocrystals. Furthermore, the size dependence of the spin-lattice relaxation rate becomes weaker as cobalt content increase in $Co_xFe_{3-x}O_4$ nanocrystals. These observations suggest that spin-orbit coupling of the surface is less sensitive to stoichiometric variation than the interior of the nanocrystals.

7.2. Future Directions

To further support the interior and surface spin model, a few experiments can be performed in the future. Based on the results from this dissertation, surface spins are more efficient reservoirs for spin-lattice relaxation due to smaller ligand field energy splitting. One way to further tune the ligand field splitting energy is by changing the functional group on the surface of the nanocrystals or changing the surroundings of the materials. Systematically changing the surfactants of Fe_3O_4 nanocrystals from strong to weak ligands should result in faster spin-lattice relaxation. Different functional groups binding on the surface of nanocrystal (e.g. –COOH, -SH, -NH_2, -CN) can provide varying degree of ligand field and spin-orbit coupling for the Fe ions of the surfaces of the nanocrystals. Therefore, overall spin relaxation of the nanocrystal can be affected by

the variation of spin-orbit coupling on the surface. In addition, the rate of spin-lattice relaxation is also dependent on the matching of the excitation spectrum in spin and vibrational degrees of freedom, since the energy in spin degrees of freedom eventually dissipates into vibrational degrees of freedom. Variations of vibrational spectrum of molecules at the interface may also have a potentially influence on the spin-lattice relaxation of the nanocrystal.

Another way to confirm the surface/ interior spin model is to compare the pump-probe Faraday rotation data of Fe_3O_4 nanocrystals with core/shell Fe_3O_4 nanocrystals where the sizes of Fe_3O_4 nanocrystals were kept the same, but in the core/shell Fe_3O_4 sample, a diamagnetic shell with inverse spinel crystal structure is added. In the core/shell sample, the surface of Fe_3O_4 will now have the same crystal structure as the interior. Therefore, the core/shell sample should show slower spin-lattice relaxation than the core only Fe_3O_4 nanocrystals.

Besides the study of spin-lattice relaxation in magnetic nanocrystals, it will be very helpful to revisit the ultrafast demagnetization part of the magnetization dynamics data to get a better picture of how magnetization evolves as a function of time. From our previous study of magnetization dynamics of Fe_2O_3 nanocrystals (completely oxidized Fe_3O_4), instead of the sub-ps demagnetization, slow demagnetization (~100 ps) is actually observed. This is quite intriguing since Fe_2O_3 and Fe_3O_4 shows very similar crystal structure and magnetization. Recent studies of ultrafast demagnetization dynamics of ferromagnetic materials indicate that the ultrafast demagnetization is actually based on a electron-phonon-mediated spin-flip scattering process.[102-103] From

the transient absorption data of Fe_3O_4 nanocrystals we saw that the strong coupling nature of electron-phonon coupling manifested itself as the coherent acoustic phonon. Therefore, it may not be surprising that we observed the ultrafast demagnetization after the nanocrystals were photoexcited. On the other hand, the transient absorption data of Fe_2O_3 nanocrystal shows no feature of oscillatory modulation of absorption which implies the weak coupling between electron and lattice and thus shows slower demagnetization. It will be interesting to see how the demagnetization time scale varies as a function of oxidation level of Fe_3O_4 nanocrystals which can provide quantitative correlation between demagnetization rate and electron-phonon coupling strength.

REFERENCES

(1) Blundell, S. *Magnetism in Condensed Matter, 1st ed.*; Oxford University Press: New York, 2001.

(2) Cullity, B. D. *Introduction to Magnetic Materials*; Addison-Wesley Pub. Co.: Reading, MA, 1972.

(3) Spaldin, N. A. *Magnetic Material: Fundamentals and Device Application*; Cambridge University Press: Cambridge, NY, 2003.

(4) Stöhr, J.; Siegmann, H. C. *Magnetism: From Fundamentals to Nanoscale Dynamics*; Springer: Berlin, 2006.

(5) Beaurepaire, E.; Merle, J. C.; Daunois, A.; Bigot, J. Y. *Phys. Rev. Lett.* **1996**, *76*, 4250.

(6) Hohlfeld, J.; Matthias, E.; Knorren, R.; Bennemann, K. H. *Phys. Rev. Lett.* **1997**, *78*, 4861.

(7) Scholl, A.; Baumgarten, L.; Jacquemin, R.; Eberhardt, W. *Phys. Rev. Lett.* **1997**, *79*, 5146.

(8) Vaterlaus, A.; Beutler, T.; Meier, F. *Phys. Rev. Lett.* **1991**, *67*, 3314.

(9) Sun, S.; Zeng, H.; Robinson, D. B.; Raoux, S.; Rice, P. M.; Wang, S. X.; Li, G. *J. Am. Chem. Soc.* **2003**, *126*, 273.

(10) Sun, S.; Zeng, H. *J. Am. Chem. Soc.* **2002**, *124*, 8204.

(11) Bao, N.; Shen, L.; Wang, Y.; Padhan, P.; Gupta, A. *J. Am. Chem. Soc.* **2007**, *129*, 12374.

(12) AK Zvezdin, V. K. *Modern Magnetooptics and Magnetooptical Materials (Condensed Matter Physics)*; 1st ed.; Taylor & Francis: New York, 1997.

(13) Lee, J. H.; Huh, Y. M.; Jun, Y.; Seo, J.; Jang, J.; Song, H. T.; Kim, S.; Cho, E. J.; Yoon, H. G.; Suh, J. S.; Cheon, J. *Nature Medicine* **2007**, *13*, 95.

(14) Liu, H. Y.; Gao, L. *J. Am. Ceram. Soc.* **2006**, *89*, 370.

(15) Jiang, Y.; Decker, S.; Mohs, C.; Klabunde, K. J. *J. Catal.* **1998**, *180*, 24.

(16) Oregan, B.; Gratzel, M. *Nature* **1991**, *353*, 737.

(17) Gomez-Abal, R.; Ney, O.; Satitkovitchai, K.; Hubner, W. *Phys. Rev. Lett.* **2004**, *92*.

(18) Takano, M.; Nasu, S.; Abe, T.; Yamamoto, K.; Endo, S.; Takeda, Y.; Goodenough, J. B. *Phys. Rev. Lett.* **1991**, *67*, 3267.

(19) Walz, F. *J. Phys.: Condens. Matter* **2002**, *14*, R285.

(20) Kimel, A. V.; Kirilyuk, A.; Usachev, P. A.; Pisarev, R. V.; Balbashov, A. M.; Rasing, T. *Nature* **2005**, *435*, 655.

(21) Cavalleri, A.; Dekorsy, T.; Chong, H. H. W.; Kieffer, J. C.; Schoenlein, R. W. *Phys. Rev. B* **2004**, *70*.

(22) Lindenberg, A. M.; Kang, I.; Johnson, S. L.; Missalla, T.; Heimann, P. A.; Chang, Z.; Larsson, J.; Bucksbaum, P. H.; Kapteyn, H. C.; Padmore, H. A.; Lee, R. W.; Wark, J. S.; Falcone, R. W. *Phys. Rev. Lett.* **2000**, *84*, 111.

(23) Bargheer, M.; Zhavoronkov, N.; Gritsai, Y.; Woo, J. C.; Kim, D. S.; Woerner, M.; Elsaesser, T. *Science* **2004**, *306*, 1771.

(24) Krauss, T. D.; Wise, F. W. *Phys. Rev. Lett.* **1997**, *79*, 5102.

(25) Goldstein, A. N.; Echer, C. M.; Alivisatos, A. P. *Science* **1992**, *256*, 1425.

(26) Son, D. H.; Hughes, S. M.; Yin, Y. D.; Alivisatos, A. P. *Science* **2004**, *306*, 1009.

(27) Cerullo, G.; De Silvestri, S.; Banin, U. *Phys. Rev. B* **1999**, *60*, 1928.

(28) Hartland, G. V. *Annu. Rev. Phys. Chem.* **2006**, *57*, 403.

(29) Son, D. H.; Wittenberg, J. S.; Banin, U.; Alivisatos, A. P. *J. Phys. Chem. B* **2006**, *110*, 19884.

(30) Cherepy, N. J.; Liston, D. B.; Lovejoy, J. A.; Deng, H.; Zhang, J. Z. *J. Phys. Chem. B* **1998**, *102*, 770.

(31) Fu, L.; Wu, Z.; Ai, X.; Zhang, J.; Nie, Y.; Xie, S.; Yang, G.; Zou, B. *J. Chem. Phys.* **2004**, *120*, 3406.

(32) Hu, M.; Petrova, H.; Hartland, G. V. *Chem. Phys. Lett.* **2004**, *391*, 220.

(33) Maillard, M.; Pileni, M.-P.; Link, S.; El-Sayed, M. A. *J. Phys. Chem. B* **2004**, *108*, 5230.

(34) Juban, E. A.; McCusker, J. K. *J. Am. Chem. Soc.* **2005**, *127*, 6857.

(35) Zeiger, H. J.; Vidal, J.; Cheng, T. K.; Ippen, E. P.; Dresselhaus, G.; Dresselhaus, M. S. *Phys. Rev. B* **1992**, *45*, 768.

(36) Pollard, W. T.; Dexheimer, S. L.; Wang, Q.; Peteanu, L. A.; Shank, C. V.; Mathies, R. A. *J. Phys. Chem.* **1992**, *96*, 6147.

(37) Gawelda, W.; Pham, V.-T.; Benfatto, M.; Zaushitsyn, Y.; Kaiser, M.; Grolimund, D.; Johnson, S. L.; Abela, R.; Hauser, A.; Bressler, C.; Chergui, M. *Phys. Rev. Lett.* **2007**, *98*, 057401/1.

(38) Lamb, H. *Proc. Math. Soc. London* **1882**, *13*, 187.

(39) Ahrens, T. J. *Mineral Physics and Crystallography: A Handbook of Physical Constants*; American Geophysical Union: Washington, DC, 1995.

(40) Clark, S. M.; Prilliman, S. G.; Erdonmez, C. K.; Alivisatos, A. P. *Nanotechnology* **2005**, *16*, 2813.

(41) The modulation depth was calculated using the amplitude (A) of the exponentialy decaying cosine function $A\cos(2\pi t/\tau+\phi)$, which describes the oscillatory part of the transient absorption data.

(42) Pillet, S.; Souhassou, M.; Lecomte, C. *Acta Crystallogr., Sect. A* **2004**, *60*, 455.

(43) Vanloef, J. J. *Physica* **1966**, *32*, 2102.

(44) Prinz, G. A. *Science* **1998**, *282*, 1660.

(45) Wolf, S. A.; Awschalom, D. D.; Buhrman, R. A.; Daughton, J. M.; von Molnar, S.; Roukes, M. L.; Chtchelkanova, A. Y.; Treger, D. M. *Science* **2001**, *294*, 1488.

(46) Zhang, G. P.; Hübner, W. *Phys. Rev. Lett.* **2000**, *85*, 3025.

(47) Park, J.; An, K. J.; Hwang, Y. S.; Park, J. G.; Noh, H. J.; Kim, J. Y.; Park, J. H.; Hwang, N. M.; Hyeon, T. *Nat. Mater.* **2004**, *3*, 891.

(48) Song, Q.; Zhang, Z. J. *J. Phys. Chem. B* **2006**, *110*, 11205.

(49) Redl, F. X.; Black, C. T.; Papaefthymiou, G. C.; Sandstrom, R. L.; Yin, M.; Zeng, H.; Murray, C. B.; O'Brien, S. P. *J. Am. Chem. Soc.* **2004**, *126*, 14583.

(50) Buchanan, K. S.; Zhu, X. B.; Meldrum, A.; Freeman, M. R. *Nano Lett.* **2005**, *5*, 383.

(51) Andrade, L. H. F.; Laraoui, A.; Vomir, M.; Muller, D.; Stoquert, J. P.; Estournes, C.; Beaurepaire, E.; Bigot, J. Y. *Phys. Rev. Lett.* **2006**, *97*, 127401.

(52) Ju, G. P.; Hohlfeld, J.; Bergman, B.; van de Veerdonk, R. J. M.; Mryasov, O. N.; Kim, J. Y.; Wu, X. W.; Weller, D.; Koopmans, B. *Phys. Rev. Lett.* **2004**, *93*, 197403.

(53) Rhie, H. S.; Durr, H. A.; Eberhardt, W. *Phys. Rev. Lett.* **2003**, *90*, 247201.

(54) Stamm, C.; Kachel, T.; Pontius, N.; Mitzner, R.; Quast, T.; Holldack, K.; Khan, S.; Lupulescu, C.; Aziz, E. F.; Wietstruk, M.; Durr, H. A.; Eberhardt, W. *Nat. Mater.* **2007**, *6*, 740.

(55) Melnikov, A.; Radu, I.; Bovensiepen, U.; Krupin, O.; Starke, K.; Matthias, E.; Wolf, M. *Phys. Rev. Lett.* **2003**, *91*, 227403.

(56) Hsia, C. H.; Chen, T. Y.; Son, D. H. *Nano Lett.* **2008**, *8*, 571.

(57) Krauss, T. D.; Wise, F. W. *Phys. Rev. Lett.* **1997**, *79*, 5102.

(58) Hu, M.; Hartland, G. V. *J. Phys. Chem. B* **2002**, *106*, 7029.

(59) Hu, M.; Petrova, H.; Hartland, G. V. *Chem. Phys. Lett.* **2004**, *391*, 220.

(60) Hunsche, S.; Wienecke, K.; Dekorsy, T.; Kurz, H. *Phys. Rev. Lett.* **1995**, *75*, 1815.

(61) Levy, M. *Handbook of Elastic Properties of Solids, Liquids, and Gases*; Academic Press: San Diego, CA, 2001.

(62) This value was obtained from the total number of nanocrystals (4.26×10^{9} particles) and the absorbed photon energy (4.39×10^{-7} J) within the probe beam volume (2.83×10^{-7} cm^3) and bulk heat capacity of Fe_3O_4 (0.643 J/mol K) by assuming fast heating and slow cooling of the lattice.

(63) Cooper, F. *Int. J. Heat Mass Transfer* **1977**, *20*, 991.

(64) Wilson, O. M.; Hu, X.; Cahill, D. G.; Braun, P. V. *Phys. Rev. B* **2002**, *66*, 224301.

(65) Bialkowski, S. E. *Photothermal Spectroscopy Methods for Chemical Analysis*; John Wiley & Sons, Inc.: Logan, UT, 1996.

(66) Razzaq, M. Y.; Anhalt, M.; Frormann, L.; Weidenfeller, B. *Mater. Sci. Eng.: A* **2007**, *444*, 227.

(67) According to the prediction from Langevin function using bulk saturation magnetization of 84 emu/g of Fe_3O_4 and magnetic field of 0.35 T, ΔT of 50K should reduce the magnetization of the nanocrystals by less than 2.5 % for the nanocrystals of all the sizes in Reference 57.

(68) Müller, G. M.; Walowski, J.; Djordjevic, M.; Miao, G.-X.; Gupta, A.; Ramos, A. V.; Gehrke, K.; Moshnyaga, V.; Samwer, K.; Schmalhorst, J.; Thomas, A.; Hütten, A.; Reiss, G.; Moodera, J. S.; Münzenberg, M. *Nat. Mater.* **2009**, *8*, 56.

(69) Krivorotov, I. N.; Emley, N. C.; Sankey, J. C.; Kiselev, S. I.; Ralph, D. C.; Buhrman, R. A. *Science* **2005**, *307*, 228.

(70) Chappert, C.; Fert, A.; van Dau, F. N. *Nat. Mater.* **2007**, *6*, 813.

(71) Wolf, S. A.; Awschalom, D. D.; Buhrman, R. A.; Daughton, J. M.; von Molnár, S.; Roukes, M. L.; Chtchelkanova, A. Y.; Treger, D. M. *Science* **2001**, *294*, 1488.

(72) Hübner, W.; Bennemann, K. H. *Phys. Rev. B* **1996**, *53*, 3422.

(73) Penoyer, R. F.; Bickford, L. R. *Phys. Rev.* **1957**, *108*, 271.

(74) Tachiki, M. *Prog. Theor. Phys.* **1960**, *23*, 1055.

(75) Beaurepaire, E.; Merle, J. C.; Daunois, A.; Bigot, J.-Y. *Phys. Rev. Lett.* **1996**, *76*, 4250.

(76) Djordjevic, M.; Lüttich, M.; Moschkau, P.; Guderian, P.; Kampfrath, T.; Ulbrich, R. G.; Münzenberg, M.; Felsch, W.; Moodera, J. S. *Phys. Status Solidi C* **2006**, *3*, 1347.

(77) Zhang, Q.; Nurmikko, A. V.; Miao, G. X.; Xiao, G.; Gupta, A. *Phys. Rev. B* **2006**, *74*, 064414.

(78) Bigot, J.-Y.; Guidoni, L.; Beaurepaire, E.; Saeta, P. N. *Phys. Rev. Lett.* **2004**, *93*, 077401.

(79) Awschalom, D. D.; DiVincenzo, D. P.; Smyth, J. F. *Science* **1992**, *258*, 414.

(80) Klimov, V. I.; McBranch, D. W. *Phys. Rev. Lett.* **1998**, *80*, 4028.

(81) Burda, C.; Chen, X.; Narayanan, R.; El-Sayed, M. A. *Chem. Rev.* **2005**, *105*, 1025.

(82) Cooney, R. R.; Sewall, S. L.; Dias, E. A.; Sagar, D. M.; Anderson, K. E. H.; Kambhampati, P. *Phys. Rev. B* **2007**, *75*, 245311.

(83) Wohlfarth, E. P. *Ferromagnetic Materials: A Handbook on the Properties of Magnetically Ordered Substances*; North-Holland: New York, 1986.

(84) Ziemniak, S. E.; Anovitz, L. M.; Castelli, R. A.; Porter, W. D. *J. Phys. Chem. Solids* **2007**, *68*, 10.

(85) Goya, G. F.; Berquó, T. S.; Fonseca, F. C.; Morales, M. P. *J. Appl. Phys.* **2003**, *94*, 3520.

(86) Adam, J. R.; Anna, C. S. S.; Zhang, Z. J. *Appl. Phys. Lett.* **2000**, *76*, 3624.

(87) Vestal, C. R.; Song, Q.; Zhang, Z. J. *J. Phys. Chem. B* **2004**, *108*, 18222.

(88) Stamm, C.; Kachel, T.; Pontius, N.; Mitzner, R.; Quast, T.; Holldack, K.; Khan, S.; Lupulescu, C.; Aziz, E. F.; Wietstruk, M.; Dürr, H. A.; Eberhardt, W. *Nat. Mater.* **2007**, *6*, 740.

(89) Koopmans, B.; Ruigrok, J. J. M.; Longa, F. D.; de Jonge, W. J. M. *Phys. Rev. Lett.* **2005**, *95*, 267207.

(90) Kise, T.; Ogasawara, T.; Ashida, M.; Tomioka, Y.; Tokura, Y.; Kuwata-Gonokami, M. *Phys. Rev. Lett.* **2000**, *85*, 1986.

(91) Koopmans, B.; van Kampen, M.; Kohlhepp, J. T.; de Jonge, W. J. M. *Phys. Rev. Lett.* **2000**, *85*, 844.

(92) Djordjevic, M.; Münzenberg, M. *Phys. Rev. B* **2007**, *75*, 012404.

(93) Chen, T.-Y.; Hsia, C.-H.; Son, D. H. *J. Phys. Chem. C* **2008**, *112*, 10125.

(94) Lessard, A.; Moos, T. H.; Hübner, W. *Phys. Rev. B* **1997**, *56*, 2594.

(95) Skomski, R.; Coey, J. M. D. *Permanent Magnetism*; Taylor & Francis Group: Bristol, UK, 1999.

(96) Morales, M. A.; Skomski, R.; Fritz, S.; Shelburne, G.; Shield, J. E.; Yin, M.; O'Brien, S.; Leslie-Pelecky, D. L. *Phys. Rev. B* **2007**, *75*, 134423.

(97) Ogasawara, T.; Ohgushi, K.; Tomioka, Y.; Takahashi, K. S.; Okamoto, H.; Kawasaki, M.; Tokura, Y. *Phys. Rev. Lett.* **2005**, *94*, 087202.

(98) Hübner, W.; Bennemann, K. H. *Phys. Rev. B* **1996**, *53*, 3422.

(99) Hsia, C.-H.; Chen, T.-Y.; Son, D. H. *J. Am. Chem. Soc.* **2009**, *131*, 9146.

(100) Sparks, M. *Ferromagnetic-Relaxation Theory*; McGraw-Hill: New York, 1964.

(101) Liu, C.; Zou, B.; Rondinone, A. J.; Zhang, Z. J. *J. Am. Chem. Soc.* **2000**, *122*, 6263.

(102) Koopmans, B.; Malinowski, G.; Dalla Longa, F.; Steiauf, D.; Fahnle, M.; Roth, T.; Cinchetti, M.; Aeschlimann, M. *Nat. Mater.* **2010**, *9*, 259.

(103) Münzenberg, M. G. *Nat. Mater.* **2010**, *9*, 184.

VITA

Name: Tai-Yen Chen

Address: Department of Chemistry
Texas A&M University
PO Box 30012
College Station, TX 77843-3012
c/o Dong Hee Son

Email Address: tytamu@gmail.com

Education:

2010	Ph.D., Chemistry Texas A&M University, College Station, TX
2004	M.S., Chemistry National Tsing Hua University, Hsinchu, Taiwan
2002	B.S., Chemistry National Tsing Hua University, Hsinchu, Taiwan

Previously Published Materials:

- Chen, T.-Y.; Hsia, C.-H.; Chen, H.-Y.; Son, D. H. “Size Effect on Chemical Tuning of Spin-Lattice Relaxation Dynamics in Superparamagnetic Nanocrystals” *J. Phys. Chem. C*, **2010**, *114*, 9713.

- Chen, H.-Y.; Chen, T.-Y.; Son, D. H. "Measurement of Energy Transfer Time in Colloidal Mn-Doped Semiconductor Nanocrystals" *J. Phys. Chem. C*, **2010**, *114,* 4418.

- Hsia, C.-H.; Chen,T.-Y.; Son, D. H. "Time-Resolved Study on Surface Spin Effect on Spin-lattice Relaxation in Fe_3O_4 nanocrystals" *J. Am. Chem. Soc.*, **2009**, *131*, 9146.

- Chen, T.-Y.; Hsia, C.-H.; Son, D. H. “Time-Dependent Elastic Properties and Lattice Temperature of the Photoexcited Iron Oxide Nanocrystals” *J. Phys. Chem. C*, **2008**, *112*, 10125.

- Hsia, C.-H.; Chen, T.-Y.; Son, D. H. "Size-Dependent Ultrafast Magnetization Dynamic in Iron Oxide Nanocrystals" *Nano Lett.*, **2008**, *8*, 2, 571.

- Chen, T.-Y.; Hsia, C.-H.; Son, H. S.; Son, D. H. "Ultrafast Energy Transfer and Strong Dynamic non-Condon Effect on Ligand Field Transitions by Coherent Phonon in γ-Fe_2O_3 Nanocrystals" *J. Am. Chem. Soc.*, **2007**, *129*, 10829.